Molecular dynamics simulations of nanoclusters in neuromorphic systems

Prifysgol Abertawe
Swansea University

Wenkai Wu

Nanomaterials Lab

Faculty of Science and Engineering

Swansea University

This dissertation is submitted for the degree of
Doctor of Philosophy

December 2022

To my loving parents

Declarations

This work has not previously been accepted in substance for any degree and is not being concurrently submitted in candidature for any degree.

Signed: ███████████

Dated: 24-May-2023

This thesis is the result of my own investigations, except where otherwise stated. Other sources are acknowledged by footnotes giving explicit references. A bibliography is appended.

Signed: ███████████

Dated: 24-May-2023

I hereby give consent for my thesis, if accepted, to be available for photocopying and for inter- library loan, and for the title and summary to be made available to outside organisations.

Signed: ███████████

Dated: 24-May-2023

The University's ethical procedures have been followed and, where appropriate, that ethical approval has been granted.

Signed: ███████████

Dated: 24-May-2023

Acknowledgements

Abstract

Neuromorphic computing is a new computing paradigm that deals with computing tasks using inter-connected artificial neurons inspired by the natural neurons in the human brain. This computational architecture is more efficient in performing many complex tasks such a pattern recognition and has promise at overcoming some of the limitations of conventional computers. Among the emerging types of artificial neurons, a cluster-based neuromorphic device is a promising system with good cost efficiency because of a simple fabrication process. This device functions using the formation and breakage of the connections ("synapses") between clusters, driven by the bias voltage applied to the clusters. The mechanisms of the formation and breakage of these connections are thus of the utmost interest.

In this thesis, the molecular dynamics simulation method is used to explore the mechanisms of the formation and breakage of the connections ("filaments") between the clusters in a model of neuromorphic device. First, the Joule heating mechanism of filament breakage is explored using a model consisting of Au nanowire that connects two Au_{1415} clusters. Upon heating, the atoms of the nanofilament gradually aggregate towards the clusters, causing the middle of the wire to gradually thin and then suddenly break. Most of the system remains crystalline during this process, but the centre becomes molten. The terminal clusters increase the melting point of the nanowires by fixing them and act as recrystallisation regions. A strong dependence of the breaking temperature is found not only on the width of the nanowires but also their length and atomic structure. Secondly, the bridge formation and thermal breaking processes between Au_{1415} clusters on a graphite substrate are also simulated. The bridging process , which can heal a broken filament, is driven by diffusion of gold along the graphite substrate. The characteristic times of bridge formation are explored at elevated simulation temperatures to estimate the longer characteristic times of formation at room-temperature conditions. The width of the bridge formed has a power-law dependence on the simulation time, and the mechanism is a combination of diffusion and viscous flow. Simulations of bridge-breaking are also conducted and reveal the existence of a voltage threshold that must be reached to activate the breakage. The role of the substrate in the bridge

formation and breakage processes is revealed as a medium of diffusion. Lastly, to explore future potential cluster materials, the thermal behaviour of Pb-Al core-shell clusters is studied. The core and shell are found to melt separately. In fact, the core atoms of nanoclusters tend to escape their shells and partially cover them, leading to a preference for a segregated state. The melting point of the core can either be depressed or elevated, depending on the thickness of the shell due to different mechanisms.

Contents

e

List of Figures

1

5

7

List of Tables

Chapter 1 Perspective and Outline

1.1 Context

With the rapidly advancing demand for computational power over the latter half of the 20th and early 21st centuries, the bottleneck of the traditional von Neumann paradigm, characterized by the sequential transfer of data and instructions between memory and the CPU through a shared data bus with limited bandwidth, is limiting the performance of modern computers [1–3]. Neuromorphic computing provides a new computing paradigm that works by mimicking the functions of human brains [4]. The new computing framework functions by assembling the interconnected artificial neurons [5] and shows promising performance in certain areas where conventional computing methods are challenged [6]. The main elemental building block that acts as a single neuron in neuromorphic computing is a memristor, which is a non-linear device that changes its resistance depending on the history of bias applied to it [7, 8]. This switching property of the memristor is mainly obtained by the formation and breakage of nanoscale conductive paths inside the device [9]. Metal cluster films fabricated with the gas-phase deposition technique have been reported to show a similar non-ohmic switching behaviour [10, 11]. Therefore, this fabrication method is a promising approach for the fabrication of neuromorphic devices due to its simplicity and affordability compared with other techniques like lithography, which usually requires multiple delicate processes to create robust inter-device connections in a deterministic way [12, 13].

Many efforts have been made to ellucidate the behaviour of cluster-based neuromorphic devices. Several mechanisms have been proposed for the explanation of the formation and breakage of the connections between clusters. According to experimental observations, such as conductance measurements, the main mechanisms of the formation of atomic-scale connections between clusters are the electric field-induced surface diffusion and evaporation, as well as the van der Waals interaction between metal atoms [14–16]. The breakage of the connections is typically explained by electromigration caused by the electric current running through them [17, 18]. Joule heating, induced by the current running through

the connections, is also a possible mechanism for breakage [19]. Experiments have shown that significant amounts of local heat can be generated in an nanowire (NW) network due to the flow of current [20], but there is a shortage of studies on the effect of Joule heating on the breaking process of connections between particles in percolating systems. Meanwhile, the precise role of the various substrates in these processes is still not well understood, and there have been no comprehensive studies considering the entire process of nanofilament formation and subsequent breakage. Additionally, studies so far have primarily focused on elemental metal clusters, but alloy clusters may offer new possibilities for neuromorphic devices.

Benefited from the rapid advance in computational power during the past decades, the use of molecular dynamics (MD) simulations has become more prevalent in both basic and applied research [21]. Molecular dynamics simulations allow researchers to model the interactions between individual atoms and track the evolution of their assemblies over time. By analyzing the coordinates, velocities, and potentials of the atoms in a system, researchers can extract and study the dynamic processes and properties of these systems in detail. Due to the method's ability to accurately simulate systems at the atomic level and provide comprehensive reproducible results with a relatively moderate computational cost, MD is an ideal tool for studying the mechanisms and exploring new possibilities in cluster-based neuromorphic systems.

The aim of this thesis is to gain a deeper understanding of the mechanisms governing the formation and brekage of filaments in cluster-based neuromorphic devices using MD simulations. To achieve this, multiple models were constructed to investigate topics such as the effect of Joule heating and the effect of the substrate. Simulation results reveal ways for the formation and breakage of connections between clusters. the formation and breaking conditions are explored through analysis of the structural variation process. Additionally, the melting mechanism of potential new building materials for neuromorphic devices, such as core-shell clusters, are studied as a reference for fabrication and research in the future.

1.2 Thesis outline

This thesis is organised into the following chapters:

- In Chapter 2, a literature review is conducted to introduce the basic concepts of neuromorphic computing and neuromorphic computing devices. The chapter begins by discussing the basic properties and main categories of neuromorphic computing devices. It then focuses on cluster-based neuromorphic devices, discussing their fabrication and experimental observations. Previous studies and the missing pieces of the mechanisms governing cluster-based neuromorphic devices are also introduced.

- In Chapter 3, an overview of the principles of MD is provided to contextualize the methodology of this thesis. The chapter includes a discussion of the basic algorithms of MD, such as the integrator, the potential, and the boundary conditions. It also introduces and reviews relevant tools and software for building models, carrying out simulations, and performing analysis.

- In Chapter 4, the thermal breakage of a Au nanofilament located between two gold nanoparticles (NPs) was simulated to study the mechanisms of cluster-based neuromorphic devices. Simulations of Au nanowires (NWs) of different lengths, widths, and shapes connecting two Au_{1415} NPs were performed, and the evolution of the system was monitored through a detailed structural identification analysis. The results showed that atoms of the nanofilament gradually aggregate towards the clusters, causing the middle of the wire to gradually thin and then break. Most of the system remains crystalline during this process, but the center is molten. The terminal nanoparticles increase the melting point of the nanowires by fixing the middle wire and acting as recrystallisation areas. A strong dependence was found on the widths of the nanowires and also on their lengths and structures. These results may serve as guidelines for the development of cluster-based neuromorphic computing systems.

- In Chapter 5, the results of simulations of the formation and thermal-breaking of bridges between Au_{1415} clusters deposited on a carbon substrate are presented. The

11

formation process is driven by diffusion, and the characteristic times are evaluated at high temperatures and used to estimate the formation times at room temperature. The width of the bridges has a power-law dependence on the simulation time. The Joule heat generated by an electric current through the bridge is estimated using a quantum conductance model, and simulations of the breaking process reveal the existence of a threshold and the role of the substrate. These results provide an atomistic-level understanding of the fundamental processes involving conductive connections between individual clusters in cluster-based nanofilms, which is essential for the practical development of cluster-based neuromorphic systems.

- The melting behavior of core-shell clusters is a critical property that impacts their fabrication and research as a potential materials for cluster-based neuromorphic devices. In Chapter 6, the melting behavior of Pb-Al core-shell clusters is investigated using MD simulations. The clusters have a fixed Pb_{147} core and varying shell thicknesses. The results show that the core and shell melt separately, with the core atoms breaking out of the shell and the nanoclusters preferring a segregated state. The melting point of the core can be either depressed or elevated depending on the thickness of the shell due to different mechanisms. As the shell becomes thicker, the condition of the break-out event changes from the melting of the core to the melting of the shell due to the increased melting temperature and robustness. These results can be used as a reference for the future fabrication and experimental observations of these clusters.

- In Chapter 7, the achievements of the previous chapters are discussed in order to summarise the findings and give an outlook on future work.

References

[1] M. M. Waldrop, "The chips are down for Moore's law," *Nature*, vol. 530, pp. 144–147, Feb 2016.

[2] UN, "A new circular vision for electronics time for a global reboot." World Economic Forum, 2019, URL: https://www.weforum.org/reports/a-new-circular-vision-for-electronics-time-for-a-global-reboot.

[3] R. A. Nawrocki, R. M. Voyles, and S. E. Shaheen, "A mini review of neuromorphic architectures and implementations," *IEEE Transactions on Electron Devices*, vol. 63, pp. 3819–3829, Oct 2016.

[4] H. Jaeger, "Towards a generalized theory comprising digital, neuromorphic and unconventional computing," *Neuromorphic Computing and Engineering*, vol. 1, no. 1, p. 012002, 2021.

[5] C. Mead, "Neuromorphic electronic systems," *Proceedings of the IEEE*, vol. 78, no. 10, pp. 1629–1636, 1990.

[6] Z. Wang, H. Wu, G. W. Burr, C. S. Hwang, K. L. Wang, Q. Xia, and J. J. Yang, "Resistive switching materials for information processing," *Nature Reviews Materials*, vol. 5, pp. 173–195, Mar 2020.

[7] D. B. Strukov, G. S. Snider, D. R. Stewart, and R. S. Williams, "The missing memristor found," *Nature*, vol. 453, no. 7191, pp. 80–83, 2008.

[8] L. O. Chua, "Memristor—The missing circuit element," *IEEE Transactions on Circuit Theory*, vol. 18, no. 5, pp. 507–519, 1971.

[9] T. Prodromakis, C. Toumazou, and L. Chua, "Two centuries of memristors," *Nature Materials*, vol. 11, pp. 478–481, jun 2012.

[10] M. Mirigliano, D. Decastri, A. Pullia, D. Dellasega, A. Casu, A. Falqui, and P. Milani, "Complex electrical spiking activity in resistive switching nanostructured Au two-terminal devices," *Nanotechnology*, vol. 31, no. 23, p. 234001, 2020.

[11] M. Mirigliano, F. Borghi, A. Podestà, A. Antidormi, L. Colombo, and P. Milani, "Non-ohmic behavior and resistive switching of Au cluster-assembled films beyond the percolation threshold," *Nanoscale Advances*, vol. 1, no. 8, pp. 3119–3130, 2019.

[12] J. Joshua Yang, F. Miao, M. D. Pickett, D. A. Ohlberg, D. R. Stewart, C. N. Lau, and R. S. Williams, "The mechanism of electroforming of metal oxide memristive switches," *Nanotechnology*, vol. 20, no. 21, p. 215201, 2009.

[13] S. K. Bose, S. Shirai, J. B. Mallinson, and S. A. Brown, "Synaptic dynamics in complex self-assembled nanoparticle networks," *Faraday Discussions*, vol. 213, pp. 471–485, 2019.

[14] M. Olsen, M. Hummelgård, and H. Olin, "Surface modifications by field induced diffusion," *PLoS ONE*, vol. 7, no. 1, p. 30106, 2012.

[15] T. T. Tsong, "Effects of an electric field in atomic manipulations," *Physical Review B*, vol. 44, pp. 13703–13710, Dec 1991.

[16] T. M. Mayer, J. E. Houston, G. E. Franklin, A. A. Erchak, and T. A. Michalske, "Electric field induced surface modification of Au," *Journal of Applied Physics*, vol. 85, pp. 8170–8177, Jun 1999.

[17] T. B. Song, Y. Chen, C. H. Chung, Y. Yang, B. Bob, H. S. Duan, G. Li, K. N. Tu, and Y. Huang, "Nanoscale Joule heating and electromigration enhanced ripening of silver nanowire contacts," *ACS Nano*, vol. 8, no. 3, pp. 2804–2811, 2014.

[18] R. Hoffmann-Vogel, "Electromigration and the structure of metallic nanocontacts," *Applied Physics Reviews*, vol. 4, no. 3, p. 031302, 2017.

[19] A. Halbritter, S. Csonka, O. Y. Kolesnychenko, G. Mihály, O. I. Shklyarevskii, O. I. Shklyarevskii, and H. van Kempen, "Connective neck evolution and conductance steps in hot point contacts," *Physical Review B*, vol. 65, pp. 454131–454138, Jan 2002.

[20] S. Koo, J. Park, S. Koo, and K. Kim, "Local heat dissipation of Ag nanowire networks examined with scanning thermal microscopy," *Journal of Physical Chemistry C*, vol. 125, no. 11, pp. 6306–6312, 2021.

[21] D. C. Rapaport, *The Art of Molecular Dynamics Simulation.* Cambridge University Press, Apr 2004.

Chapter 2   An Introduction to Neuromorphic Computing Devices

This chapter reviews the literature on neuromorphic computing that underpins the work in the thesis. The first section, 2.1, is an introduction to neuromorphic computing devices and the main categories of such devices. The next section, 2.2, is focused on cluster-based neuromorphic computing devices and review relevant research concerning the fabrication and measurements of these devices. Section 2.3 then considers the mechanism operating in such systems, which emphasises the making and breaking of connections, or filaments, between clusters.

2.1   Neuromorphic computing and devices

In 1936, Alan Turing published a paper entitled 'On computable numbers, with an application to the Entscheidungsproblem', which presented proof that a certain kind of machine, now known as a 'Turing machine', can process any algorithm for mathematical computation [1]. Later, in 1945, John von Neumann presented a framework for a computing machine known as the von Neumann architecture, which then became the basis for most modern computers [2]. Computers based on this framework have achieved remarkable success and have become indispensable in numerous areas, including critical domains like scientific research [3], medicine [4], engineering [5], and finance [6], among others. However, the performance of these computers is limited by an inherent limitation in the architecture called von Neumann bottleneck [7]. The von Neumann bottleneck arises from the fact that data and instructions are stored in the same memory and must be fetched sequentially. This causes a delay, as the processing unit must wait for the data or instructions to be fetched before it can perform any computation. As a result, the speed of the processor may not be fully utilized, leading to performance inefficiencies.

On the other hand, in 1948, Turing predicted a computing machine that operated like neural systems in a meeting report [8]. The idea was then explicitly clarified by Mead [9]. In this machine, artificial neurons are all connected in an arbitrary pattern

with modifiers between them. Due to the properties of analog and parallel connections, the system can solve many problems that are hard to solve using von Neumann systems. Many of these problems, like pattern recognition, adaptive behaviour, fuzzy logic, etc., are more and more critical in the current era of big data and artificial intelligence. As a result, machine frameworks inspired by biological systems have attracted intense research interest, with the goal of building a machine based on neurophysiological models like the human brain [10, 11].

To achieve the features of neural systems in brains, devices with a neuromorphic architecture should have the ability to adjust the 'synaptic signal strength' or create new connections when processing information as the brain does. This property is called neuroplasticity. Many models have been proposed to explain the mechanism of synaptic plasticity in brains. Donald Hebb proposed a basic mechanism of the synaptic plasticity known as the Hebbian learning rule in 1949 [12]. In this model, the connections between two neurons might be strengthened if the neurons fire simultaneously. The model works well as long as all the input patterns are orthogonal or uncorrelated, but this requirement seriously limits the range of its applications [13–17]. Other models, such as the Bienenstock–Cooper–Munro (BCM) learning rule [18] and Hebbian-covariance rule [19], are extensions based on the Hebbian rule. They can also explain some mechanisms, but a single model that can explain all the observed properties of synaptic plasticity does not exist at this time.

There are two synaptic plasticity mechanisms that are critical for neuromorphic devices. They are the short-term plasticity (STP) and long-term plasticity mechanisms (LTP). STP refers to changes in the synaptic strength that happen within a short period, usually from 10 ms to 1 s. It is a quick adjustment of the synaptic strength control that helps determine how important that connection is to the ongoing process [20–22]. In the absence of presynaptic activity, the synaptic strength quickly returns to its initial level. An increased probability of an increase in synaptic strength in response to presynaptic action potentials is called short-term synaptic enhancement [23]. A decreased synaptic strength caused by the depletion of the vesicles, certain postsynaptic processes, or the feedback of presynaptic receptors is called short-term synaptic depression [24]. LTP refers to the

17

long-lasting activity-dependent changes in the synaptic strength. It lasts from minutes to hours or even longer, and it is widely considered the dominant model of how brains learn and remember information [25]. The synaptic activity patterns that produce a long-lasting increase in the synaptic strength are known as long-term potentiation, while other patterns that produce a long-lasting decrease are called long-term depression [26,27]. The relation between STP and LTP is researched by Hebb, who hypothesized that continuous and repeated stimulation from presynaptic neurons to postsynaptic neurons could cause an increase in the efficiency of synaptic transmission [12]. The concept of spike-timing-dependent plasticity (STDP) further improves Hebb's theory, revealing that the time relationship between presynaptic and postsynaptic spikes can adjust the synaptic weight [28]. STDP enables learning without any external control on the synaptic strengths or any previous knowledge of the information to be processed. This property makes STDP the basis for autonomous, unsupervised learning [29]. Frequency-dependent-synaptic plasticity (SRDP) is another learning mechanism for LTP in the brain, which indicates that synaptic weight can be adjusted by controlling the frequency of presynaptic spikes [30].

The typical device that is generally used as a single neuron in a neuromorphic computing system is called a memristor [31–33]. A memristor is a passive electronic circuit device for which pinched hysteresis loops in I-V curves are observed [34]. This current-voltage feature indicates that the conductance state of the device can be switched by the bias being applied to it. The first memristor was proposed in 1971 by Leon Chua, who combined the common circuit elements (resistor, capacitor and inductor) [35]. In Chua's model, many valuable properties of memristors are demonstrated, and meanwhile, in oxide-based resistance switches, pinched hysteresis loops in I-V curves have been observed [36]. However, it was not until 2008 that the link between the theory and an experimental demonstration was established by a team in a HP lab [37,38]. Memristors then attracted a large amount of attention and were used in a wide range of applications, such as neuromorphic computing, non-volatile random access memory (NVRAM), etc [39].

The artificial synapse devices used to construct a neuromorphic network can be categorised into several branches based on the materials used to construct them (e.g. electro-

chemical metallisation materials, phase-changing materials, ferroelectric materials, ionic/-electronic hybrid materials) [40]. To mimic bio-synaptic functions, these synaptic devices have a variety of materials, fabrication process and functions. Here, we introduce the main categories of neuromorphic devices.

Electrochemical metallisation materials Electrochemical metallisation (ECM) memory is an important resistive switching memory composed of a sandwiched structure that consists of the top electrode, active layer and bottom electrode. The resistive switching mechanism is based on the formation and breakage of the metallic filament, which utilises the oxidation of active electrodes like Ag and Cu. Metal cations are transported through the active layer, and reduction reactions occur at the noble metal electrode. The filament dissipation may be due to spontaneous diffusion, Joule heating, or ionisation. Diverse electrochemical metallisation materials have been used to fabricate ECM memory, including chalcogenide [41–43], nitride [44], amorphous silicon [45] and polymer [46, 47].

Figure 2-1 below (from [48]) illustrates the operation of an ECM memory cell during an $I-V$ switching cycle using a quasi-static triangular voltage stimulation signal. The cell consists of an electrochemically active electrode (AE) made of a metal such as Ag, Cu, or Ni, an electrochemically inert counter electrode (CE) made of a metal such as Pt, Ir, or W, and a thin film of a solid electrolyte (i.e., an ion conductor of the metal in AE) sandwiched between the two electrodes. In the initial high-resistance state (OFF-state), there is no electrodeposit of the metal on the inert electrode (Figure 2-1 (a)). When a sufficiently positive bias voltage is applied to the active electrode AE, a SET process occurs. This process involves the anodic dissolution of the AE metal, the drift of cations across the solid electrolyte thin film, and the reduction and electro-crystallization of the AE metal on the surface of the inert electrode CE. The electro-crystallization process, which is enhanced by the electric field, results in the growth of a metal filament preferentially in the direction of the active electrode (Figure 2-1 (c)). When the metal filament grows far enough to make an electronic connection with the opposite AE electrode, the cell switches to the ON-state (Figure 2-1 (d)). The cell remains in the ON-state unless a sufficient voltage of opposite polarity is applied, which RESETs the cell (Figure 2-1 (e))
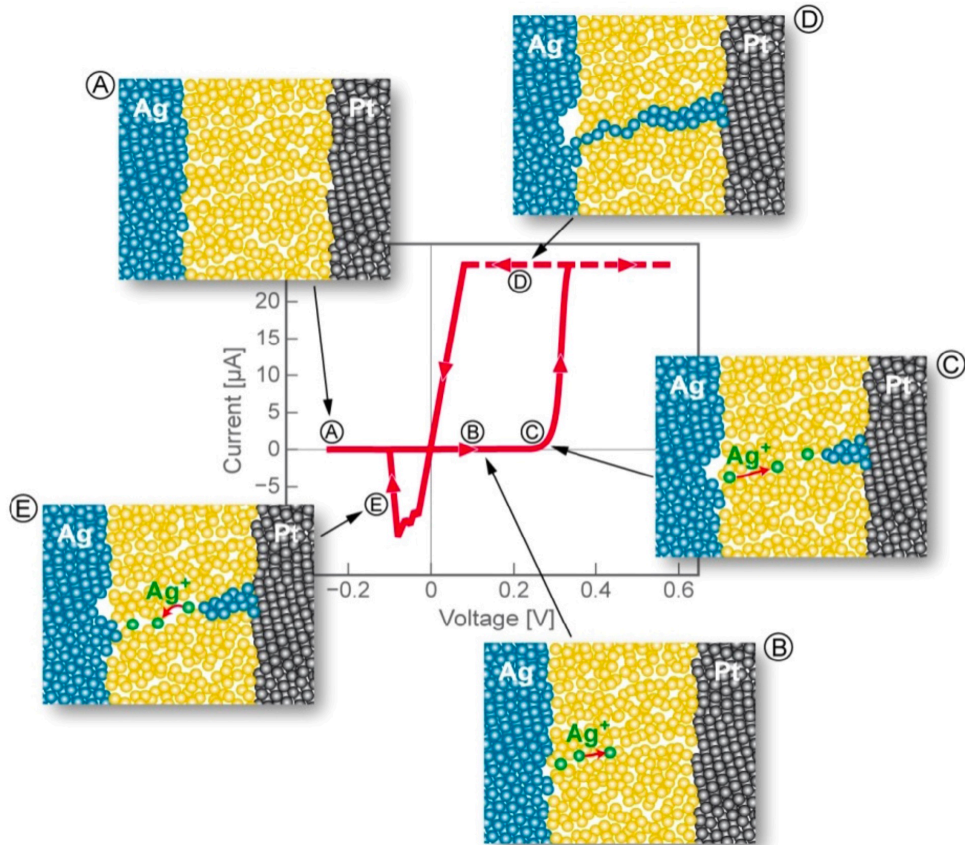
Figure 2-1 A figure from [48]. Sketch of the steps of the SET ((a)–(d)) and RESET (e) operations of an electrochemical metallization memory (ECM) cell.

to its initial OFF-state (Figure 2-1 (a)). During the initial phase of RESET, there is both an electronic current through the metallic filament and an electrochemical current that dissolves the metal filament. The SET switching speed of ECM cells is mainly determined by the kinetics of the process steps involved in the SET process.

Phase-change materials Phase-change materials have been extensively explored in memory applications (PCM: phase-change memory) because of their fast read/write speed and extensible and controllable multilevel resistance states [49–56]. The switching is realised by the transition from the amorphous phase (high-resistance state) to the crystalline phase (low-resistance state) due to Joule heating [57]. For the 'set' operation, applying an appropriate voltage to the PCM causes Joule heating, subsequently raising the material

20

temperature to above the crystal transition temperature but below the melting temperature. As for the 'reset' operation, the material temperature is raised above the melting temperature and then quickly quenched to room temperature, causing the material transfer to enter an amorphous phase. By precisely controlling the transition process between these two states, multiple levels of intermediate states can be achieved to emulate biological synapses [58–60]. Many kinds of chalcogenide glass can be used to create phase-change memory, including GeTe [51] and $Ge_2Sb_2Te_5$ (GST) [54].

The example in reference [61] describes a PCM device that utilizes GST as the dielectric material. GST has low resistivity in its polycrystalline state and high resistivity in its amorphous phase, which can be reversibly transitioned between to update the conductance of the PCM device. The device structure consists of GST sandwiched between a top electrode and a narrow bottom electrode (shown in Figure 2-2 (a)). The as-fabricated dielectric is initially in the crystalline phase. Through the application of heat, an amorphous region can be created around the narrow bottom electrode, resulting in a low conductance device state. This process, called RESET, can be achieved through the use of a short current pulse that causes melting and subsequent quenching of the material. The conductance can then be gradually increased through the application of a sequence of SET pulses, which raise the device temperature to its crystallization regime and reduce the volume of the amorphous region through crystal growth. This process, called SET, can be gradual and accumulative when using suitable current amplitudes. However, the RESET process that creates the amorphous region is observed to be non-accumulative and abrupt. Figure 2-2 (b) shows the conductance evolution statistics from 10,000 devices that were initialized to around 0.1 μS and subjected to 20 SET pulses of 90 μA amplitude and 50 ns width. The mean of the conductance change per subsequent programming pulse decreases and its standard deviation increases, leading to non-linear update behavior. An experiment was performed in which devices were applied with SET pulse sequences with different time delays, simulating the situation in neural network training where different sets of synaptic memory devices may be programmed at different times and drift at different rates. The results of this experiment are shown in Figure 2-2 (c).
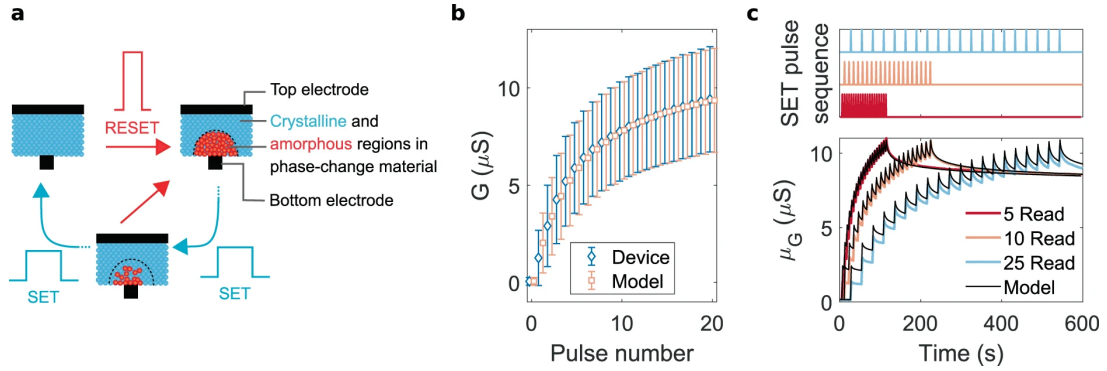
Figure 2-2 A Phase-change memory example based on GST [61]. (a) Phase-change memory devices have a phase change material sandwiched between a top electrode and a narrow bottom electrode. In a mushroom-like device structure, such as the one shown in the figure, the application of a RESET pulse creates an amorphous dome around the narrow bottom electrode. The crystalline state of the material can then be reversed through the application of SET pulses, which induce crystal growth and gradually increase the conductance of the device. (b) Non-linear conductance evolution characteristics of PCM in response to a sequence of SET pulses with 90 μA amplitude and 50 ns width. (c) Conductance evolution of PCM when programmed with 20 SET pulses of different delays. SET programming pulses are delayed by inserting different numbers of read pulses in between.

Ferroelectric materials Ferroelectric materials have a high dielectric constant and spontaneous polarisation [62–64]. The polarisation states of the ferroelectric materials can be tuned by applying voltages, so these materials can be used as the active layer in synaptic devices. Meanwhile, the fine polarisation states of the ferroelectric material can be achieved by applying a certain pulse sequence, so multiple conductance states can be obtained in this kind of synaptic device. The multilevel changes of the conductance are able to imitate various synapse behaviours. Ferroelectric materials could help synaptic devices to improve their ON/OFF ratio and the linearity of weight updates [65].

In [63], a ferroelectric artificial synapse was created using an inorganic based on ferroelectric tunnel junctions to realize STDP, through which the synaptic strengths evolve depending on the timing and causality of electrical signals from neighbouring neurons as shown in Figure 2-3 (a). The $BiFeO_3$ (BFO) active layer was placed between Pt/Co and $YAlO_3$ (YAO) top, and $(Ca,Ce)MnO_3$ (CCMO) bottom electrodes as shown in Figure 2-3 (b). The device demonstrated well-defined voltage thresholds in its hysteresis loop as shown in Figure 2-3 (c) due to the inherent inhomogeneous polarization switching in the BFO, enabling the implementation of STDP. When both pre- and post-neuron spikes reach the memristor with a delay Δt, their combination produces the waveforms $(V_{pre} - V_{post})$ displayed in the inset of Figure 2-3 (d). The combined waveform temporary exceeds the threshold voltage, leading to an increase ($\Delta G > 0$, synapse strengthening) or a decrease ($\Delta G < 0$, synapse weakening) of the conductance (G), depending on the sign of Δt. As seen from the experimental STDP curve in Figure 2-3 (d), only closely timed spikes produce a conductance change whereas long delays leave the device unchanged.

Ionic/electronic hybrid materials Ionic/electronic hybrid materials are employed in field-effect transistors (FETs). The architecture comprises gate electrolytes and channel materials. Gate electrolytes can be made using diverse materials, such as ion gel [66, 67], ion liquid [68, 69], inorganic oxides [70, 71] and polyelectrolytes [72, 73]. Channel materials can be made using both inorganic and organic materials, such as carbon nanotubes (CNTs) [74, 75]; graphene [76, 77], MoS_2 [78, 79], IZO [71], IGZO [80] and MoO3 [68]; and PEDOT:PSS [81–83].
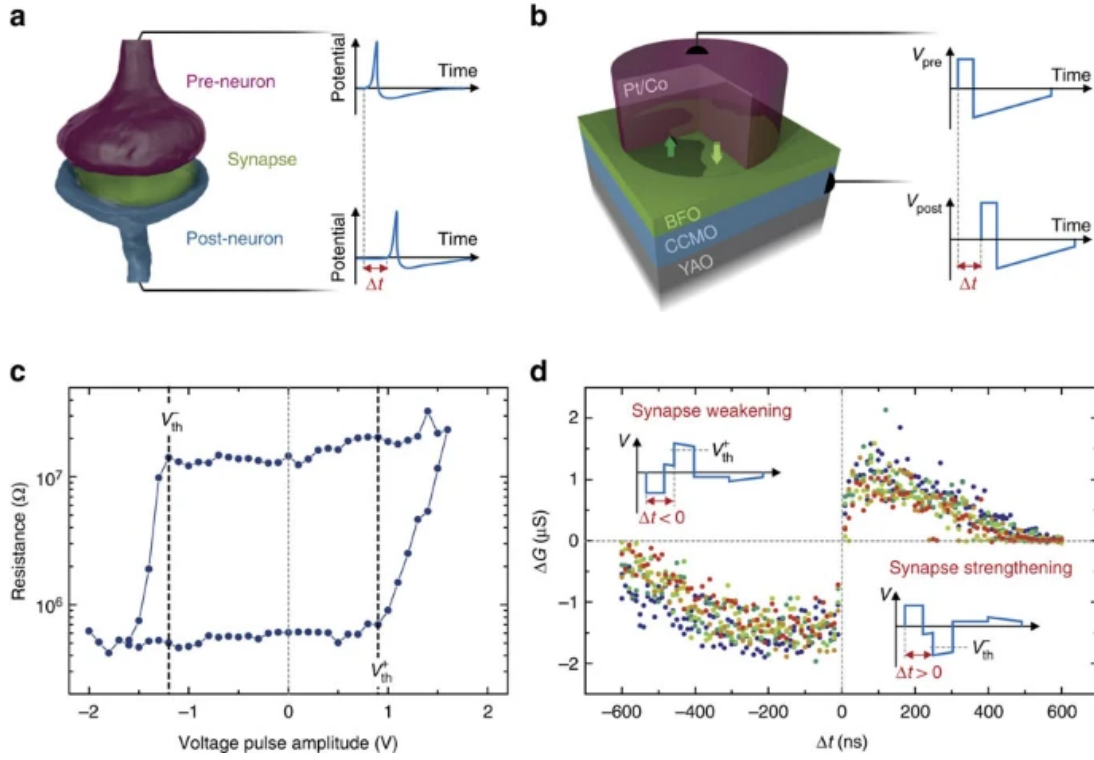
Figure 2-3 Sketches and measurements of a ferroelectric memristor in [63]. (a) Sketch of pre-neurons (in purple) and post-neurons (in blue) connected by a synapse (in green), with the synaptic transmission modulated by the causality (Δt) of neuron spikes. (b) Sketch of a ferroelectric memristor, with a ferroelectric tunnel barrier of $BiFeO_3$ (BFO) sandwiched between a bottom electrode of $(Ca,Ce)MnO_3$ (CCMO) and a top submicron pillar of Pt/Co, and $YAlO_3$ (YAO). (c) Single-pulse hysteresis loop of the ferroelectric memristor, showing clear voltage thresholds (V_{th}^{+} and V_{th}^{-}). (d) Measurements of STDP in the ferroelectric memristor, showing the modulation of the device conductance (ΔG) as a function of the delay (Δt) between pre- and post-synaptic spikes. Seven data sets were collected on the same device, demonstrating the reproducibility of the effect. The total length of each pre- and post-synaptic spike is 600 ns.

24
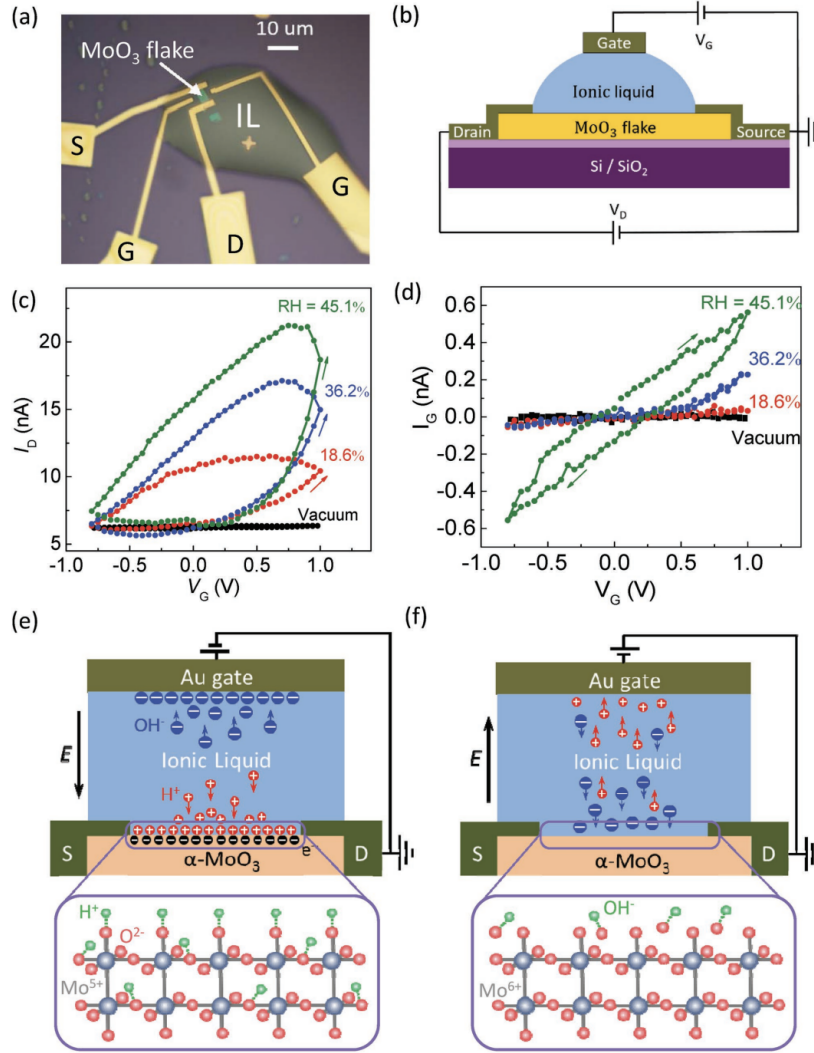
Figure 2-4 Quasi-2D α-MoO$_3$-based three-terminal synaptic device [68]. (a) Optical image of the device. (b) Schematic illustration of device structure and measurement setup. (c,d) I_D and I_G dependence on gate voltage under different relative humidity conditions. (e) Schematic of transistor structure under positive gate voltage application. The applied electric field drives protons and hydroxyls, which dissociate from H$_2$O adsorbed in the ionic liquid, in the opposite direction. (f) Schematic of transistor structure under negative gate voltage application.

Figure 2-4 shows a quasi-2D α-MoO$_3$-based three-terminal synaptic device [68]. The optical image and schematic illustration of the device structure and measurement setup are shown in (a) and (b), respectively. In the measurement setup, a small dc voltage ($V_D = 50$ mV) is applied between the source and drain electrodes and the corresponding drain current (I_D) is measured. The gate voltage (V_G) is directly applied on the gate electrode and the corresponding gate current (I_G) is also monitored. (c,d) show the dependence of I_D and I_G on the gate voltage under different relative humidity conditions (vacuum, 18.6%, 36.2%, 45.1%). (e) and (f) show schematics of the transistor structure under positive and negative gate voltage application, respectively. In the positive gate voltage application, the applied electric field drives protons and hydroxyls to dissociate from H$_2$O adsorbed in the ionic liquid and move in opposite directions. The protons are adsorbed at the α-MoO$_3$ channel surface and injected into the α-MoO$_3$ lattice, resulting in an increase in the channel conductance. In the negative gate voltage application, the protons are extracted and desorbed from the α-MoO$_3$ channel surface with the accumulation of hydroxyls, resulting in a decrease in the channel conductance back to the initial state.

The main categories of artificial synaptic devices mentioned above usually have complicated fabrication processes. Building such a device requires multiple layers of materials to be accurately stacked using different masking procedures or lithography techniques. In recent years, a more straightforward method was developed to fabricate such synaptic devices, which involves depositing nanoclusters between two metal electrodes on insulating substrates. When a large enough amount of surface coverage, called the percolation threshold, is reached during the deposition, the nanoparticles in the device are able to form and break atomic-scale wires between the gaps and show switching events similar to the potentiation in biological neural systems [84]. The following two sections will introduce the fabrication, experimental properties and general research of the behaviour of these cluster-based neuromorphic systems.

2.2 Cluster-based neuromorphic systems: fabrication and experimental measurements

The random assembly of nanoscale building blocks is becoming one of the most promising approaches to forming a neuromorphic network [85], and atomic clusters and small nanoparticles can function as its building blocks. Metal cluster films fabricated using the gas-phase deposition technique have been reported to show non-ohmic synaptic-like switching behaviour [86–91]. Such films are fabricated by depositing clusters onto an insulating substrate with prefabricated electrodes on it. The conductance of the device needs to be measured during the deposition to monitor the formation of a connective path. Therefore, the deposited cluster should be neutral to prevent interference with the measurements. The deposition should be immediately stopped when a sudden change in the conductance is detected. This conductance jump means that a long-range connectivity between two electrodes was established by the clusters. There is a term in percolation theory called the percolation threshold that represents the critical point where this connectivity occurs [92]. In this situation, the conductance can switch to different states because of the establishment of and damage to the long-range connection, which are controlled by the bias voltage applied. Figure 2-5 shows the scanning electron microscope (SEM) image and an illustration of the cluster film near the percolation threshold. The cluster deposition can be described in detail by the 2D inhomogeneous fully penetrable discs model [87], and the surface coverage p by the clusters at the percolation threshold is $p_c \approx 0.68$ [93]. The substrate of the device can be made of a variety of insulating materials, such as silicon nitride [89, 90], silica [88], glass [85] and even paper [91]. Benefitting from the development of cluster deposition technologies [94–96], the approach is more straightforward and possibly cheaper than other techniques such as the lithography method [97–99], which needs to create robust intra- and inter-device connections in a deterministic way.

The nanoscale coalescence in a percolating nanocluster film is a focus of interest because the connection between the clusters formed or broken during the measurement will directly determine the properties of the device. The neck radius r between two coalescing

27
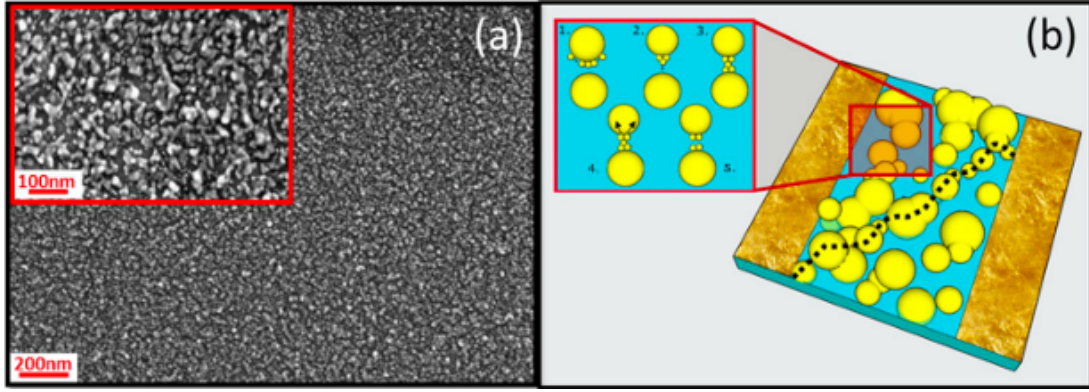
Figure 2-5 From [85]. (a) SEM images of the Au nanocluster film on a glass substrate near the percolation threshold. (b) Schematic illustration of a percolating cluster system. The substrate is marked light blue and the gold clusters and electrodes are marked yellow. A tunneling path is marked with a black dashed line. The insert shows typical situations that occur when the bridge is formed or broken between clusters.

clusters follows a power law $r \propto t^\alpha$, where t is time and α is specific to the physical process and lies between 1/6 (surface diffusion) and 1/2 (viscous flow) [100,101]. The conductance of two coalescent clusters depends on the neck radius according to the following relation: $G \propto r^\omega$ [102], where ω is equal to 1 or 2 depending on whether r is larger or smaller than the electron mean free path. The combination of the two relations above suggests that the conductance is expected to follow the following power law in time: $G \propto t^\beta$, where $\beta = \alpha \cdot \omega$ has a value between 1/6 and 1. A comparison between the conductance measurements on bismuth cluster films and kinetic Monte Carlo (kMC) simulations has verified the prevalence of the power law predicted by theory [103]. The power is $\alpha \approx 0.3$ when $r/R < 0.5$, where R is the radius of the particle. This relation has also been observed in situ on gold nanoparticles using transmission electron microscopy (TEM) [104].

The transfer properties of the cluster devices differ according to the size of the network. The quantisation of the conductance has been observed in samples with small areas $(10 \times 20 \ \mu m)$ made by tin clusters that were ~ 7 nm in diameter [87]. When the width of the connection is comparable to the Fermi wavelength λ_F of the carriers, the quantised conductance of the connection is an integral number multiple of the conductance
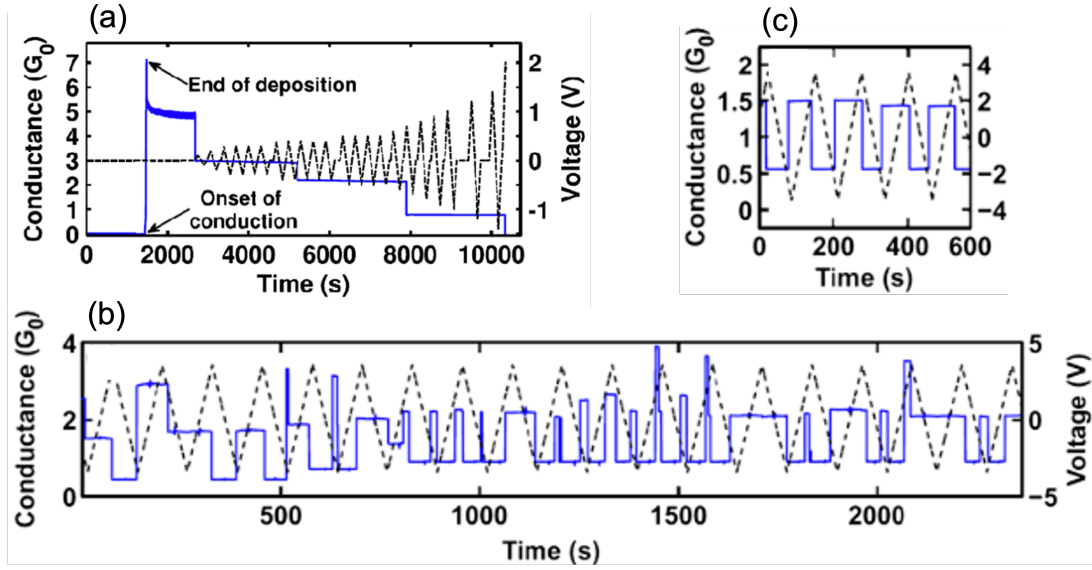
Figure 2-6 The conductance of cluster films with different sizes [87]. (a) Conductance of a 10×20 μm sample (solid line) showing downward steps under an applied ramping voltage (dashed line). (b) Typical multilevel switching behaviour of an 100×200 μm sample under an applied voltage ramp. (c) Example of repeatable switching between two conductance levels in a sample that is the same size as the sample in (b).

quantum (the quantized unit of electrical conductance) $G_0 = 2e^2/h$ [105]. Figure 2-6 (a) shows decreasing quantised steps when the applied ramping bias is increasing during the measurement. On the other hand, larger samples (100×200 μm) show more complicated conductance steps, as shown in Figure 2-6 (b). Repeated steps can be observed between similar conductance levels, but in many other cases, the conductance switches between multiple levels. The behaviour occurs because there is a much more complicated network in a large sample, with a much larger number of possible percolating pathways. The size of the step (rather than the conductance) is also quantised in some cases, as shown in Figure 2-6 (c), which indicates the repeated formation and breakage of a connecting path controlled by the bias.

Despite the complexity in the switching behaviour, some typical events can be identified when the maximum of the ramping bias is higher than a threshold beyond which

29
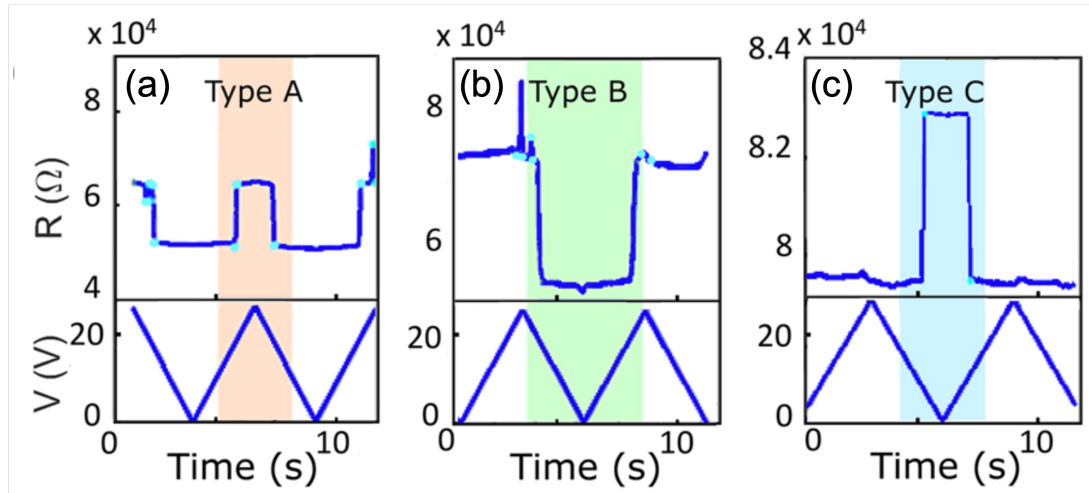
Figure 2-7 Examples of characteristic switching events [85]. The three simplest types of events are reported: (a) resistance increase (conductance decrease) at high voltage (pink region); (b) resistance decrease (conductance increase) at low voltage (green region); and (c) resistance increase (conductance decrease) at low voltage (blue region). These archetypes are referred to as Type A, B and C, respectively.

a complex cascade of switching events occurs [85], as shown in Figure 2-7. These typical events are classified into three types: Type A – a step-wise decrease in the conductance is observed when the voltage is increasing (marked in pink); Type B – a step-wise increase in the conductance is observed when the voltage is decreasing; and Type C – a step-wise decrease in the conductance is observed when the voltage is decreasing. For all three event types, the transitions occur at almost exactly the same voltage, which means that the connection and breakage of **the same** conductive path is controlled by the voltage in these events. Meanwhile, the distinguished nature of Type C events indicates a different physical origin compared to Type A and B events, and is due to the breakage of connections as the voltage is decreased. Therefore, multiple mechanisms are responsible for the formation and breakage of the connections; these mechanisms will be discussed in the next section.

30

2.3 Mechanisms of the formation and breakage of conductive filaments

The mechanisms of the formation and breakage of the conductive connections between clusters are fundamental and have been widely discussed in the literature.

According to experimental observations, such as conductance measurements [87, 106], electric field-induced surface diffusion (EFISD) and evaporation (EFIE) and the van der Waals interaction between metal atoms are considered the main mechanisms of the formation of atomic-scale connections between the clusters [107–109]. Van der Waals forces are weak attractive forces that arise from the particle's electric polarisation, which is induced by the presence of other particles. The non-retarded van der Waals interaction energy between two atoms at a distance r from each other is given by $W(r) = -C/r^6$, where C is determined by the atoms [110]. Using this relation, the potential or forces between objects in certain geometric configurations have been calculated [111]. By considering a tip and STM (Scanning tunneling microscope)-like model, it can be proved that an ad-atom on a surface will be attracted by the approaching tip to the centre of the gap between the tip and the surface [107]. In the cluster film devices, ad-atoms are accumulatively attracted toward the centre of the gap between the clusters, and they form a connection. The formation mechanism is completely irrelevant to the bias, but the connection can be damaged due to the higher bias voltage applied. Afterwards, when the bias voltage is released, ad-atoms will accumulate again, and the connection will have a chance to be rebuilt. In this mechanism, connections are formed automatically but bias is needed to break them. Therefore, the high conductance state will be at a low bias and the low conductance state will be at a high bias. The Type A and Type B events shown in Figure 2-7 are both consistent with this van der Waals-based mechanism. A further piece of evidence is the random switch events observed with a constant higher bias voltage, as shown in Figure 2-8 [85]. The connection randomly formed by the van der Waals forces is immediately broken due to the voltage [85].

Another mechanism for the formation of connections involves electric field-induced surface diffusion (EFISD) and electric field-induced evaporation (EFIE). EFISD and EFIE

31
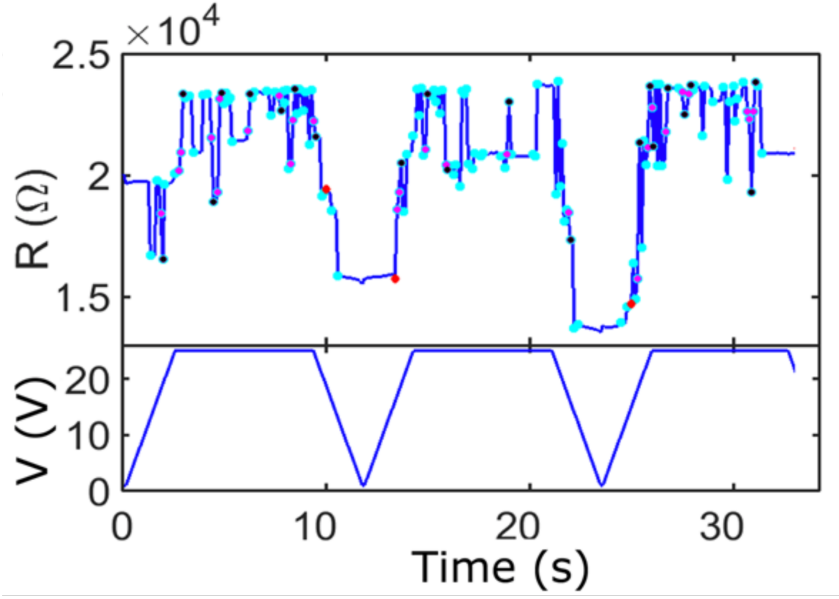
Figure 2-8 Switching events recorded at high voltage [85].

describe how a polarised ad-atom will diffuse along the surface or even be evaporated due to the strong applied electric field by the approaching tip [107–109]. The electric fields required for EFISD and EFIE are ~ 1 V$\cdot$nm^{-1} [107] and ~ 20 V$\cdot$nm^{-1} [112, 113], respectively. Under this mechanism, the connection between clusters is formed by the aggregated polarised ad-atoms under a strong electric field induced by the bias. When the electric field is not strong enough to form such a link, the existing link will be broken due to the current flow. This phenomenon can explain the Type C events shown in Figure 2-7. Another piece of experimental evidence is that after all the connections are broken by the repeated cycling of the voltage ($2 \sim 4$ V), a higher voltage (~ 10 V) can restart the switching behaviour, as shown in Figure 2-9 [87].

On the other hand, the breakage of the connections is explained by the electromigration caused by the electric current running through the connections. Numerous studies have emphasised the contribution of electromigration to the breakage or resistive switching of metal nanowires (NWs) [114–117]. In a conductor with current flow, the ionised atoms are affected by two forces: the direct electrostatic force F_e and the force from the exchange of momentum with other charge carriers F_p. In metallic conductors, F_p is called the wind force F_w. Suppose that the momentum lost by the current flow is mv_d per τ_i, where v_d

32
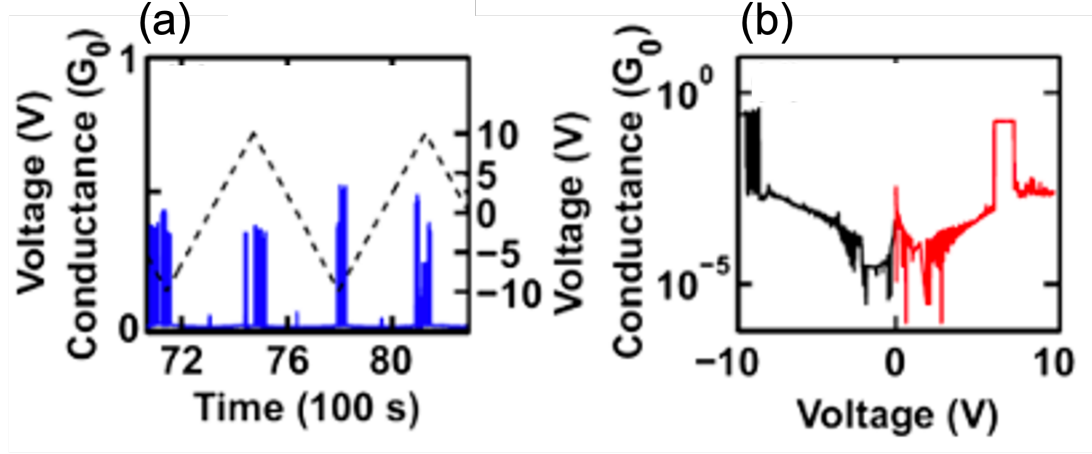
Figure 2-9 Switching events recorded at high voltage ($\sim$ 10 V) after all the connections are broken by the repeated cycling of the voltage (2 $\sim$ 4 V). (a) Signal measured under a ramping bias of $V_{max} = 10$ V [87]. (b) I-V curve of (a). The exponential increase is the evidence for tunneling; it indicates that no connection is formed if the voltage is not strong enough.

is the drift velocity and τ_i is the collision time for electron scattering at an impurity or a defect ion. By multiplying by the electron density n and dividing by the density of defect or impurity ions N_i, one can express the wind force in terms of the charge current j as follows:

$$\mathbf{F}_w = -\frac{\mathbf{j}/m}{e\tau_i N_i} = -e\frac{n\rho_i}{N_i\rho}\mathbf{E}, \tag{2-1}$$

where $\rho = E/j$ is the total resistivity and $\rho_i = m/(ne^2\tau_i)$ is the resistivity due to collisions with the impurities [117].

An alternative mechanism for the breakage is the Joule heating induced by the current running through the connections [86]. High temperatures of up to thousands of kelvins can be induced by small voltage drops on the order of $\sim$100 mV when the size of a point contact in a complex nanoscale junction is smaller than the mean free path of electrons [118]. The thermally induced breaking of nanowires (NW) has been frequently reported [119–121], and relevant computer simulations have been carried out [122–124]. Strong local heating can be observed in an NW network when the current exists [125]. The breaking process of the NW caused by heat generation can be observed in situ using

33

TEM [126].

While the mechanism mentioned above provides some insights, it does not paint the full picture. The effect of Joule heating on the breaking process of connections between particles in percolating systems is non-negligible, but there is a shortage of studies on this effect. In parallel, although there are plenty of experimental studies and computer simulations of cluster dynamics on various substrates [127–129], the role of the substrate in the formation and breakage of conductive filaments remains unclear. Furthermore, previous cluster-based neuromorphic devices have primarily used elemental metals, highlighting the need to explore new potential materials. The following chapters of this thesis will address these issues respectively, delving into the impact of Joule heating and substrate properties on the formation and breakage of conductive filaments, as well as exploring alternative materials for the development of cluster-based neuromorphic devices. This comprehensive approach aims to advance our understanding of the underlying mechanisms and contribute to the improvement of neuromorphic technology.

References

[1] A. M. Turing, "On computable numbers, with an application to the entscheidungsproblem," *Proceedings of the London Mathematical Society*, vol. s2-42, no. 1, pp. 230–265, 1937.

[2] J. Von Neumann, *First draft of a report on the EDVAC*. Moore School of Electrical Engineering, University of Pennsylvania, 1945.

[3] T. Hey, S. Tansley, K. Tolle, and J. Gray, *The Fourth Paradigm: Data-Intensive Scientific Discovery*. Microsoft Research, October 2009.

[4] H. G. Xu, Z. G. Zhang, Y. Feng, J. Yuan, Y. Zhao, and W. Zheng, "Vanadium-doped small silicon clusters: Photoelectron spectroscopy and density-functional calculations," *Chemical Physics Letters*, vol. 487, no. 4-6, pp. 204–208, 2010.

[5] G. Aouad, S. Wu, A. Lee, and T. Onyenobi, *Computer aided design guide for architecture, engineering and construction*. Routledge, 2013.

[6] J. J. Murphy, *Technical analysis of the financial markets: a comprehensive guide to trading methods and applications.* New York Institute of Finance, 1999.

[7] J. Backus, "Can Programming Be Liberated from the von Neumann Style? A Functional Style and Its Algebra of Programs," *Communications of the ACM*, vol. 21, pp. 613–641, aug 1978.

[8] A. M. Turing, "Intelligent machinery, a heretical theory," *Philosophia Mathematica*, vol. 4, no. 3, pp. 256–260, 1996.

[9] C. Mead, "Neuromorphic electronic systems," *Proceedings of the IEEE*, vol. 78, no. 10, pp. 1629–1636, 1990.

[10] H. C. Anderson, "Neural network machines," *IEEE Potentials*, vol. 8, pp. 13–16, Feb 1989.

[11] L. Chua, G. C. Sirakoulis, and A. Adamatzky, *Handbook of Memristor Networks.* Cham: Springer International Publishing, 2019.

[12] D. Hebb, *The Organization of Behavior.* Psychology Press, Apr 2005.

[13] H. Markram, "A history of spike-timing-dependent plasticity," *Frontiers in Synaptic Neuroscience*, vol. 3, no. 8, pp. 1–24, 2011.

[14] H. Markram, J. Lübke, M. Frotscher, and B. Sakmann, "Regulation of synaptic efficacy by coincidence of postsynaptic APs and EPSPs," *Science*, vol. 275, no. 5297, pp. 213–215, 1997.

[15] W. B. Levy and O. Steward, "Temporal contiguity requirements for long-term associative potentiation/depression in the hippocampus," *Neuroscience*, vol. 8, no. 4, pp. 791–797, 1983.

[16] L. N. Cooper and M. F. Bear, "The BCM theory of synapse modification at 30: interaction of theory with experiment," *Nature Reviews Neuroscience*, vol. 13, pp. 798–810, nov 2012.

[17] G. Q. Bi and M. M. Poo, "Synaptic modifications in cultured hippocampal neurons: Dependence on spike timing, synaptic strength, and postsynaptic cell type," *Journal of Neuroscience*, vol. 18, no. 24, pp. 10464–10472, 1998.

[18] E. L. Bienenstock, L. N. Cooper, and P. W. Munro, "Theory for the development of neuron selectivity: Orientation specificity and binocular interaction in visual cortex," *Journal of Neuroscience*, vol. 2, no. 1, pp. 32–48, 1982.

[19] T. Sejnowski, S. Chattarji, and P. Sfanton, "Induction of synaptic plasticity by Hebbian covariance in the hippocampus," *The Computing Neuron*, pp. 105–124, 1989.

[20] C. F. Stevens and Y. Wang, "Facilitation and depression at single central synapses," *Neuron*, vol. 14, no. 4, pp. 795–802, 1995.

[21] H. Markram and M. Tsodyks, "Redistribution of synaptic efficacy between neocortical pyramidal neurons," *Nature*, vol. 382, no. 6594, pp. 807–810, 1996.

[22] L. F. Abbott and W. G. Regehr, "Synaptic computation," *Nature*, vol. 431, pp. 796–803, oct 2004.

[23] C. F. Stevens and J. F. Wesseling, "Augmentation is a potentiation of the exocytotic process," *Neuron*, vol. 22, no. 1, pp. 139–146, 1999.

[24] R. S. Zucker and W. G. Regehr, "Short-term synaptic plasticity," *Annual Review of Physiology*, vol. 64, pp. 355–405, 2002.

[25] M. A. Lynch, "Long-term potentiation and memory," *Physiological Reviews*, vol. 84, no. 1, pp. 87–136, 2004.

[26] E. R. Kandel, "The molecular biology of memory storage: A dialogue between genes and synapses," *Science*, vol. 294, no. 5544, pp. 1030–1038, 2001.

[27] S. Fusi, P. J. Drew, and L. F. Abbott, "Cascade models of synaptically stored memories," *Neuron*, vol. 45, no. 4, pp. 599–611, 2005.

[28] N. Caporale and Y. Dan, "Spike Timing–Dependent Plasticity: A Hebbian Learning Rule," *Annual Review of Neuroscience*, vol. 31, pp. 25–46, jul 2008.

[29] T. Masquelier, R. Guyonneau, and S. J. Thorpe, "Competitive STDP-Based Spike Pattern Learning," *Neural Computation*, vol. 21, pp. 1259–1276, may 2009.

[30] C. C. Law and L. N. Cooper, "Formation of receptive fields in realistic visual environments according to the Bienenstock, Cooper, and Munro (BCM) theory.," *Proceedings of the National Academy of Sciences*, vol. 91, pp. 7797–7801, aug 1994.

[31] M. J. Lee, C. B. Lee, D. Lee, S. R. Lee, M. Chang, J. H. Hur, Y. B. Kim, C. J. Kim, D. H. Seo, S. Seo, U. I. Chung, I. K. Yoo, and K. Kim, "A fast, high-endurance and scalable non-volatile memory device made from asymmetric Ta2O5-xx/TaO2-xbilayer structures," *Nature Materials*, vol. 10, no. 8, pp. 625–630, 2011.

[32] Z. Yang, X. Yang, and Z. Xu, "Molecular dynamics simulation of the melting behavior of Pt-Au nanoparticles with core-shell structure," *Journal of Physical Chemistry C*, vol. 112, no. 13, pp. 4937–4947, 2008.

[33] M. Wuttig and N. Yamada, "Phase-change materials for rewriteable data storage," *Nature Materials*, vol. 6, no. 11, pp. 824–832, 2007.

[34] L. O. Chua and S. M. Kang, "Memristive devices and systems," *Proceedings of the IEEE*, vol. 64, no. 2, pp. 209–223, 1976.

[35] L. O. Chua, "Memristor—The missing circuit element," *IEEE Transactions on Circuit Theory*, vol. 18, no. 5, pp. 507–519, 1971.

[36] W. R. Hiatt and T. W. Hickmott, "Bistable switching in niobium oxide diodes," *Applied Physics Letters*, vol. 6, no. 6, pp. 106–108, 1965.

[37] D. B. Strukov, G. S. Snider, D. R. Stewart, and R. S. Williams, "The missing memristor found," *Nature*, vol. 453, no. 7191, pp. 80–83, 2008.

[38] R. S. Williams, "How we found the missing memristor," *IEEE Spectrum*, vol. 45, no. 12, pp. 28–35, 2008.

[39] S. S. Sarwar, S. A. N. Saqueb, F. Quaiyum, and A. B. M. H.-U. Rashid, "Memristor-Based Nonvolatile Random Access Memory: Hybrid Architecture for Low Power Compact Memory Design," *IEEE Access*, vol. 1, pp. 29–34, 2013.

[40] M. Zeng, Y. He, C. Zhang, and Q. Wan, "Neuromorphic devices for bionic sensing and perception," *Frontiers in Neuroscience*, vol. 15, Jun 2021.

[41] T. Hasegawa, T. Ohno, K. Terabe, T. Tsuruoka, T. Nakayama, J. K. Cimzewski, and M. Aono, "Learning abilities achieved by a single solid-state atomic switch," *Advanced Materials*, vol. 22, pp. 1831–1834, Apr 2010.

[42] T. Ohno, T. Hasegawa, T. Tsuruoka, K. Terabe, J. K. Gimzewski, and M. Aono, "Short-term plasticity and long-term potentiation mimicked in single inorganic synapses," *Nature Materials*, vol. 10, pp. 591–595, Aug 2011.

[43] J. J. Zhang, H. J. Sun, Y. Li, Q. Wang, X. H. Xu, and X. S. Miao, "AgInSbTe memristor with gradual resistance tuning," *Applied Physics Letters*, vol. 102, p. 183513, May 2013.

[44] Y. Yang, P. Gao, S. Gaba, T. Chang, X. Pan, and W. Lu, "Observation of conducting filament growth in nanoscale resistive memories," *Nature Communications*, vol. 3, p. 732, Jan 2012.

[45] X. Zhang, S. Liu, X. Zhao, F. Wu, Q. Wu, W. Wang, R. Cao, Y. Fang, H. Lv, S. Long, Q. Liu, and M. Liu, "Emulating short-term and long-term plasticity of bio-synapse based on Cu/a-Si/Pt memristor," *IEEE Electron Device Letters*, vol. 38, pp. 1208–1211, Sept 2017.

[46] S. Li, F. Zeng, C. Chen, H. Liu, G. Tang, S. Gao, C. Song, Y. Lin, F. Pan, and D. Guo, "Synaptic plasticity and learning behaviours mimicked through Ag interface movement in an Ag/conducting polymer/Ta memristive system," *Journal of Materials Chemistry C*, vol. 1, no. 34, pp. 5292–5298, 2013.

[47] M. K. Kim and J. S. Lee, "Short-term plasticity and long-term potentiation in artificial biosynapses with diffusive dynamics," *ACS Nano*, vol. 12, pp. 1680–1687, Feb 2018.

[48] I. Valov, R. Waser, J. R. Jameson, and M. N. Kozicki, "Electrochemical metallization memories—fundamentals, applications, prospects," *Nanotechnology*, vol. 22, p. 289502, jul 2011.

[49] S. R. Ovshinsky, "Reversible electrical switching phenomena in disordered structures," *Physical Review Letters*, vol. 21, pp. 1450–1453, Nov 1968.

[50] M. H. Lankhorst, B. W. Ketelaars, and R. A. Wolters, "Low-cost and nanoscale non-volatile memory concept for future silicon chips," *Nature Materials*, vol. 4, pp. 347–352, Apr 2005.

[51] O. Bichler, M. Suri, D. Querlioz, D. Vuillaume, B. DeSalvo, and C. Gamrat, "Visual pattern extraction using energy-efficient "2-PCM synapse" neuromorphic architecture," *IEEE Transactions on Electron Devices*, vol. 59, pp. 2206–2214, Aug 2012.

[52] T. V. Bliss and T. Lømo, "Long-lasting potentiation of synaptic transmission in the dentate area of the anaesthetized rabbit following stimulation of the perforant path," *The Journal of Physiology*, vol. 232, pp. 331–356, Jul 1973.

[53] M. Suri, O. Bichler, D. Querlioz, B. Traoré, O. Cueto, L. Perniola, V. Sousa, D. Vuillaume, C. Gamrat, and B. Desalvo, "Physical aspects of low power synapses based on phase change memory devices," *Journal of Applied Physics*, vol. 112, p. 054904, Sept 2012.

[54] S. Ambrogio, N. Ciocchini, M. Laudato, V. Milo, A. Pirovano, P. Fantini, and D. Ielmini, "Unsupervised learning by spike timing dependent plasticity in phase change memory (PCM) synapses," *Frontiers in Neuroscience*, vol. 10, Mar 2016.

[55] S. Ambrogio, P. Narayanan, H. Tsai, R. M. Shelby, I. Boybat, C. Di Nolfo, S. Sidler, M. Giordano, M. Bodini, N. C. Farinha, B. Killeen, C. Cheng, Y. Jaoudi,

and G. W. Burr, "Equivalent-accuracy accelerated neural-network training using analogue memory," *Nature*, vol. 558, pp. 60–67, Jun 2018.

[56] I. Boybat, M. Le Gallo, S. R. Nandakumar, T. Moraitis, T. Parnell, T. Tuma, B. Rajendran, Y. Leblebici, A. Sebastian, and E. Eleftheriou, "Neuromorphic computing with multi-memristive synapses," *Nature Communications*, vol. 9, p. 2514, Dec 2018.

[57] G. W. Burr, M. J. BrightSky, A. Sebastian, H. Y. Cheng, J. Y. Wu, S. Kim, N. E. Sosa, N. Papandreou, H. L. Lung, H. Pozidis, E. Eleftheriou, and C. H. Lam, "Recent progress in phase-change memory technology," *IEEE Journal on Emerging and Selected Topics in Circuits and Systems*, vol. 6, pp. 146–162, Jun 2016.

[58] K. Nakayama, M. Takata, T. Kasai, A. Kitagawa, and J. Akita, "Pulse number control of electrical resistance for multi-level storage based on phase change," *Journal of Physics D: Applied Physics*, vol. 40, pp. 5061–5065, Sept 2007.

[59] D. Ielmini, A. L. Lacaita, A. Pirovano, F. Pellizzer, and R. Bez, "Analysis of phase distribution in phase-change nonvolatile memories," *IEEE Electron Device Letters*, vol. 25, pp. 507–509, Jul 2004.

[60] T. Nirschl, J. B. Philipp, T. D. Happ, G. W. Burr, B. Rajendran, M. H. Lee, A. Schrott, M. Yang, M. Breitwisch, C. F. Chen, E. Joseph, M. Lamorey, R. Cheek, S. H. Chen, S. Zaidi, S. Raoux, Y. C. Chen, Y. Zhu, R. Bergmann, H. L. Lung, and C. Lam, "Write strategies for 2 and 4-bit multi-level phase-change memory," *Technical Digest - International Electron Devices Meeting (IEDM)*, pp. 461–464, 2007.

[61] S. R. Nandakumar, I. Boybat, M. Le Gallo, E. Eleftheriou, A. Sebastian, and B. Rajendran, "Experimental Demonstration of Supervised Learning in Spiking Neural Networks with Phase-Change Memory Synapses," *Scientific Reports*, vol. 10, p. 8080, may 2020.

[62] A. Chanthbouala, V. Garcia, R. O. Cherifi, K. Bouzehouane, S. Fusil, X. Moya, S. Xavier, H. Yamada, C. Deranlot, N. D. Mathur, M. Bibes, A. Barthélémy, and J. Grollier, "A ferroelectric memristor," *Nature Materials*, vol. 11, pp. 860–864, Oct 2012.

[63] S. Boyn, J. Grollier, G. Lecerf, B. Xu, N. Locatelli, S. Fusil, S. Girod, C. Carrétéro, K. Garcia, S. Xavier, J. Tomas, L. Bellaiche, M. Bibes, A. Barthélémy, S. Saïghi, and V. Garcia, "Learning through ferroelectric domain dynamics in solid-state synapses," *Nature Communications*, vol. 8, p. 14736, Apr 2017.

[64] L. Tu, S. Yuan, J. Xu, K. Yang, P. Wang, X. Cui, X. Zhang, J. Wang, Y. Q. Zhan, and L. R. Zheng, "A wide-range operating synaptic device based on organic ferroelectricity with low energy consumption," *RSC Advances*, vol. 8, no. 47, pp. 26549–26553, 2018.

[65] M. K. Kim and J. S. Lee, "Ferroelectric analog synaptic transistors," *Nano Letters*, vol. 19, pp. 2044–2050, Mar 2019.

[66] C. Qian, J. Sun, L. A. Kong, G. Gou, J. Yang, J. He, Y. Gao, and Q. Wan, "Artificial synapses based on in-plane gate organic electrochemical transistors," *ACS Applied Materials and Interfaces*, vol. 8, pp. 26169–26175, Oct 2016.

[67] W. Xu, S. Y. Min, H. Hwang, and T. W. Lee, "Organic core-sheath nanowire artificial synapses with femtojoule energy consumption," *Science Advances*, vol. 2, Jun 2016.

[68] C. S. Yang, D. S. Shang, N. Liu, G. Shi, X. Shen, R. C. Yu, Y. Q. Li, and Y. Sun, "A synaptic transistor based on quasi-2D molybdenum oxide," *Advanced Materials*, vol. 29, p. 1700906, Jul 2017.

[69] A. Melianas, T. J. Quill, G. LeCroy, Y. Tuchman, H. V. Loo, S. T. Keene, A. Giovannitti, H. R. Lee, I. P. Maria, I. McCulloch, and A. Salleo, "Temperature-resilient solid-state organic artificial synapses for neuromorphic computing," *Science Advances*, vol. 6, Jul 2020.

41

[70] C. J. Wan, L. Q. Zhu, J. M. Zhou, Y. Shi, and Q. Wan, "Memory and learning behaviors mimicked in nanogranular SiO 2-based proton conductor gated oxide-based synaptic transistors," *Nanoscale*, vol. 5, no. 21, pp. 10194–10199, 2013.

[71] C. J. Wan, Y. H. Liu, P. Feng, W. Wang, L. Q. Zhu, Z. P. Liu, Y. Shi, and Q. Wan, "Flexible metal oxide/graphene oxide hybrid neuromorphic transistors on flexible conducting graphene substrates," *Advanced Materials*, vol. 28, pp. 5878–5885, Jul 2016.

[72] F. Yu, L. Q. Zhu, H. Xiao, W. T. Gao, and Y. B. Guo, "Restickable oxide neuromorphic transistors with spike-timing-dependent plasticity and Pavlovian associative learning activities," *Advanced Functional Materials*, vol. 28, p. 1804025, Oct 2018.

[73] Y. He, S. Nie, R. Liu, S. Jiang, Y. Shi, and Q. Wan, "Spatiotemporal information processing emulated by multiterminal neuro-transistor networks," *Advanced Materials*, vol. 31, p. 1900903, May 2019.

[74] K. Kim, C. L. Chen, Q. Truong, A. M. Shen, and Y. Chen, "A carbon nanotube synapse with dynamic logic and learning," *Advanced Materials*, vol. 25, pp. 1693–1698, Mar 2013.

[75] P. Feng, W. Xu, Y. Yang, X. Wan, Y. Shi, Q. Wan, J. Zhao, and Z. Cui, "Printed neuromorphic devices based on printed carbon nanotube thin-film transistors," *Advanced Functional Materials*, vol. 27, p. 1604447, Feb 2017.

[76] H. Tian, W. Mi, X. F. Wang, H. Zhao, Q. Y. Xie, C. Li, Y. X. Li, Y. Yang, and T. L. Ren, "Graphene dynamic synapse with modulatable plasticity," *Nano Letters*, vol. 15, pp. 8013–8019, Dec 2015.

[77] M. T. Sharbati, Y. Du, J. Torres, N. D. Ardolino, M. Yun, and F. Xiong, "Low-power, electrochemically tunable graphene synapses for neuromorphic computing," *Advanced Materials*, vol. 30, p. 1802353, Sept 2018.

[78] J. Jiang, J. Guo, X. Wan, Y. Yang, H. Xie, D. Niu, J. Yang, J. He, Y. Gao, and Q. Wan, "2D MoS2 neuromorphic devices for brain-like computational systems," *Small*, vol. 13, p. 1700933, Aug 2017.

[79] R. A. John, F. Liu, N. A. Chien, M. R. Kulkarni, C. Zhu, Q. Fu, A. Basu, Z. Liu, and N. Mathews, "Synergistic gating of electro-iono-photoactive 2D chalcogenide neuristors: Coexistence of Hebbian and homeostatic synaptic metaplasticity," *Advanced Materials*, vol. 30, p. 1800220, Jun 2018.

[80] J. Zhou, N. Liu, L. Zhu, Y. Shi, and Q. Wan, "Energy-efficient artificial synapses based on flexible IGZO electric-double-layer transistors," *IEEE Electron Device Letters*, vol. 36, pp. 198–200, Feb 2015.

[81] P. Gkoupidenis, N. Schaefer, B. Garlan, and G. G. Malliaras, "Neuromorphic functions in PEDOT:PSS organic electrochemical transistors," *Advanced Materials*, vol. 27, pp. 7176–7180, Nov 2015.

[82] P. Gkoupidenis, D. A. Koutsouras, and G. G. Malliaras, "Neuromorphic device architectures with global connectivity through electrolyte gating," *Nature Communications*, vol. 8, p. 15448, Aug 2017.

[83] Y. Van De Burgt, E. Lubberman, E. J. Fuller, S. T. Keene, G. C. Faria, S. Agarwal, M. J. Marinella, A. Alec Talin, and A. Salleo, "A non-volatile organic electrochemical device as a low-voltage artificial synapse for neuromorphic computing," *Nature Materials*, vol. 16, pp. 414–418, Apr 2017.

[84] S. Fostner and S. A. Brown, "Neuromorphic behavior in percolating nanoparticle films," *Physical Review E - Statistical, Nonlinear, and Soft Matter Physics*, vol. 92, no. 5, pp. 1–11, 2015.

[85] C. Minnai, A. Bellacicca, S. A. Brown, and P. Milani, "Facile fabrication of complex networks of memristive devices," *Scientific Reports*, vol. 7, no. 1, p. 7955, 2017.

[86] M. Mirigliano, D. Decastri, A. Pullia, D. Dellasega, A. Casu, A. Falqui, and P. Milani, "Complex electrical spiking activity in resistive switching nanostructured Au two-terminal devices," *Nanotechnology*, vol. 31, no. 23, p. 234001, 2020.

[87] A. Sattar, S. Fostner, and S. A. Brown, "Quantized conductance and switching in percolating nanoparticle films," *Physical Review Letters*, vol. 111, no. 13, p. 136808, 2013.

[88] M. Mirigliano, F. Borghi, A. Podestà, A. Antidormi, L. Colombo, and P. Milani, "Non-ohmic behavior and resistive switching of Au cluster-assembled films beyond the percolation threshold," *Nanoscale Advances*, vol. 1, no. 8, pp. 3119–3130, 2019.

[89] S. K. Bose, J. B. Mallinson, R. M. Gazoni, and S. A. Brown, "Stable self-assembled atomic-switch networks for neuromorphic applications," *IEEE Transactions on Electron Devices*, vol. 64, no. 12, pp. 5194–5201, 2017.

[90] J. B. Mallinson, S. Shirai, S. K. Acharya, S. K. Bose, E. Galli, and S. A. Brown, "Avalanches and criticality in self-organized nanoscale networks," *Science Advances*, vol. 5, no. 11, p. eaaw8483, 2019.

[91] C. Minnai, M. Mirigliano, S. A. Brown, and P. Milani, "The nanocoherer: An electrically and mechanically resettable resistive switching device based on gold clusters assembled on paper," *Nano Futures*, vol. 2, no. 1, p. 1002, 2018.

[92] D. Stauffer and A. Aharony, *Introduction to Percolation Theory*. Taylor & Francis, 2nd revised ed., 1992.

[93] J. Quintanilla, S. Torquato, and R. M. Ziff, "Efficient measurement of the percolation threshold for fully penetrable discs," *Journal of Physics A: Mathematical and General*, vol. 33, pp. L399–L407, Oct 2000.

[94] K. Wegner, P. Piseri, H. V. Tafreshi, and P. Milani, "Cluster beam deposition: A tool for nanoscale science and technology," *Journal of Physics D: Applied Physics*, vol. 39, no. 22, pp. 439–460, 2006.

[95] C. Zhang, H. Tsunoyama, H. Akatsuka, H. Sekiya, T. Nagase, and A. Nakajima, "Advanced nanocluster ion source based on high-power impulse magnetron sputtering and time-resolved measurements of nanocluster formation," *Journal of Physical Chemistry A*, vol. 117, no. 40, pp. 10211–10217, 2013.

[96] R. E. Palmer, L. Cao, and F. Yin, "Note: Proof of principle of a new type of cluster beam source with potential for scale-up," *Review of Scientific Instruments*, vol. 87, no. 4, pp. 10–13, 2016.

[97] J. Joshua Yang, F. Miao, M. D. Pickett, D. A. Ohlberg, D. R. Stewart, C. N. Lau, and R. S. Williams, "The mechanism of electroforming of metal oxide memristive switches," *Nanotechnology*, vol. 20, no. 21, p. 215201, 2009.

[98] C. Du, F. Cai, M. A. Zidan, W. Ma, S. H. Lee, and W. D. Lu, "Reservoir computing using dynamic memristors for temporal information processing," *Nature Communications*, vol. 8, p. 2204, 2017.

[99] S. K. Bose, S. Shirai, J. B. Mallinson, and S. A. Brown, "Synaptic dynamics in complex self-assembled nanoparticle networks," *Faraday Discussions*, vol. 213, pp. 471–485, 2019.

[100] G. C. Kuczynski, "Study of the sintering of glass," *Journal of Applied Physics*, vol. 20, pp. 1160–1163, Dec 1949.

[101] F. A. Nichols and W. W. Mullins, "Morphological changes of a surface of revolution due to capillarity-induced surface diffusion," *Journal of Applied Physics*, vol. 36, no. 6, pp. 1826–1835, 1965.

[102] A. Mikrajuddin, F. G. Shi, H. K. Kim, and K. Okuyama, "Size-dependent electrical constriction resistance for contacts of arbitrary size: From Sharvin to Holm limits," *Materials Science in Semiconductor Processing*, vol. 2, pp. 321–327, Dec 1999.

[103] P. Y. Convers, D. N. McCarthy, A. Sattar, F. Natali, S. C. Hendy, and S. A. Brown, "Electrical signature of nanoscale coalescence in a percolating Bi nanocluster film," *Physical Review B*, vol. 82, no. 11, pp. 1–5, 2010.

[104] T. H. Lim, D. McCarthy, S. C. Hendy, K. J. Stevens, S. A. Brown, and R. D. Tilley, "Real-time TEM and kinetic Monte Carlo studies of the coalescence of decahedral gold nanoparticles," *ACS Nano*, vol. 3, no. 11, pp. 3809–3813, 2009.

[105] R. Landauer, "Spatial variation of currents fields due to localized scatterers in metallic conduction," *IBM Journal of Research and Development*, vol. 1, pp. 223–231, Jul 2010.

[106] M. D. Pike, S. K. Bose, J. B. Mallinson, S. K. Acharya, S. Shirai, E. Galli, S. J. Weddell, P. J. Bones, M. D. Arnold, and S. A. Brown, "Atomic scale dynamics drive brain-like avalanches in percolating nanostructured networks," *Nano Letters*, vol. 20, no. 5, pp. 3935–3942, 2020.

[107] M. Olsen, M. Hummelgård, and H. Olin, "Surface modifications by field induced diffusion," *PLoS ONE*, vol. 7, no. 1, p. 30106, 2012.

[108] T. T. Tsong, "Effects of an electric field in atomic manipulations," *Physical Review B*, vol. 44, pp. 13703–13710, Dec 1991.

[109] T. M. Mayer, J. E. Houston, G. E. Franklin, A. A. Erchak, and T. A. Michalske, "Electric field induced surface modification of Au," *Journal of Applied Physics*, vol. 85, pp. 8170–8177, Jun 1999.

[110] C. Kittel, *Introduction to Solid State Physics*. John Wiley & Sons, Inc., 2005.

[111] H. C. Hamaker, "The London-van der Waals attraction between spherical particles," *Physica*, vol. 4, pp. 1058–1072, Oct 1937.

[112] T. Ganetsos, A. W. Mair, G. L. Mair, L. Bischoff, C. Akhmadaliev, and C. J. Aidinis, "Can direct field-evaporation of doubly charged ions and post-ionisation from the singly charged state co-exist?," *Surface and Interface Analysis*, vol. 39, pp. 128–131, Feb 2007.

[113] T. T. Tsong, *Atom-Probe Field Ion Microscopy*. Cambridge University Press, Aug 1990.

[114] T. H. Kim, X. G. Zhang, D. M. Nicholson, B. M. Evans, N. S. Kulkarni, B. Rad-hakrishnan, E. A. Kenik, and A. P. Li, "Large discrete resistance jump at grain boundary in copper nanowire," *Nano Letters*, vol. 10, no. 8, pp. 3096–3100, 2010.

[115] S. L. Johnson, A. Sundararajan, D. P. Hunley, and D. R. Strachan, "Memristive switching of single-component metallic nanowires," *Nanotechnology*, vol. 21, no. 12, p. 125204, 2010.

[116] T. B. Song, Y. Chen, C. H. Chung, Y. Yang, B. Bob, H. S. Duan, G. Li, K. N. Tu, and Y. Huang, "Nanoscale Joule heating and electromigration enhanced ripening of silver nanowire contacts," *ACS Nano*, vol. 8, no. 3, pp. 2804–2811, 2014.

[117] R. Hoffmann-Vogel, "Electromigration and the structure of metallic nanocontacts," *Applied Physics Reviews*, vol. 4, no. 3, p. 031302, 2017.

[118] A. Halbritter, S. Csonka, O. Y. Kolesnychenko, G. Mihály, O. I. Shklyarevskii, O. I. Shklyarevskii, and H. van Kempen, "Connective neck evolution and conductance steps in hot point contacts," *Physical Review B*, vol. 65, pp. 454131–454138, Jan 2002.

[119] Y. H. Wen, Y. Zhang, J. C. Zheng, Z. Z. Zhu, and S. G. Sun, "Orientation-dependent structural transition and melting of Au nanowires," *Journal of Physical Chemistry C*, vol. 113, no. 48, pp. 20611–20617, 2009.

[120] A. Volk, D. Knez, P. Thaler, A. W. Hauser, W. Grogger, F. Hofer, and W. E. Ernst, "Thermal instabilities and Rayleigh breakup of ultrathin silver nanowires grown in helium nanodroplets," *Physical Chemistry Chemical Physics*, vol. 17, no. 38, pp. 24570–24575, 2015.

[121] M. Schnedlitz, M. Lasserus, D. Knez, A. W. Hauser, F. Hofer, and W. E. Ernst, "Thermally induced breakup of metallic nanowires: Experiment and theory," *Physical Chemistry Chemical Physics*, vol. 19, no. 14, pp. 9402–9408, 2017.

[122] Y. H. Wen, Z. Z. Zhu, R. Zhu, and G. F. Shao, "Size effects on the melting of nickel nanowires: A molecular dynamics study," *Physica E: Low-Dimensional Systems and Nanostructures*, vol. 25, no. 1, pp. 47–54, 2004.

[123] P. Moskovkin, M. Panshenskov, S. Lucas, and A. V. Solov'yov, "Simulation of nanowire fragmentation by means of kinetic Monte Carlo approach: 2D case," *Physica Status Solidi (B) Basic Research*, vol. 251, no. 7, pp. 1456–1462, 2014.

[124] W. Wu, T. Pavloudis, A. V. Verkhovtsev, A. V. Solov'yov, and R. E. Palmer, "Molecular dynamics simulation of nanofilament breakage in neuromorphic nanoparticle networks," *Nanotechnology*, vol. 33, p. 275602, Jul 2022.

[125] S. Koo, J. Park, S. Koo, and K. Kim, "Local heat dissipation of Ag nanowire networks examined with scanning thermal microscopy," *Journal of Physical Chemistry C*, vol. 125, no. 11, pp. 6306–6312, 2021.

[126] C. L. Kim, J. Y. Lee, D. G. Shin, J. S. Yeo, and D. E. Kim, "Mechanism of heat-induced fusion of silver nanowires," *Scientific Reports*, vol. 10, p. 9271, 2020.

[127] J. Y. Ruzicka, F. Abu Bakar, C. Hoeck, R. Adnan, C. Mcnicoll, T. Kemmitt, B. C. Cowie, G. F. Metha, G. G. Andersson, and V. B. Golovko, "Toward control of gold cluster aggregation on TiO2 via surface treatments," *Journal of Physical Chemistry C*, vol. 119, pp. 24465–24474, Oct 2015.

[128] A. V. Verkhovtsev, Y. Erofeev, and A. V. Solov'yov, "Soft landing of metal clusters on graphite: A molecular dynamics study," *The European Physical Journal D*, vol. 74, p. 205, Oct 2020.

[129] L. Bardotti, P. Jensen, A. Hoareau, M. Treilleux, B. Cabaud, A. Perez, and F. C. S. Aires, "Diffusion and aggregation of large antimony and gold clusters deposited on graphite," *Surface Science*, vol. 367, pp. 276–292, Dec 1996.

Chapter 3   Simulation Methods

In this chapter we introduce the simulation methods related to this thesis. The first section, 3.1, is about the molecular dynamics simulations, which is the main research method in this thesis. We introduce the basic principles and algorithms of molecular dynamics simulations. The next section, 3.2, introduces some useful tools and will review several tools which are related with this thesis

3.1   Molecular dynamics simulation method

Molecular dynamics (MD) simulations are a computer simulation method for analysing the dynamics of small particles like atoms, molecules or proteins [1]. The atoms and molecules are set in a simulation box and are allowed to interact for a period of time to obtain the evolution of the system. The trajectories of particles are calculated by continuously solving Newton's equations of motion numerically, where the forces between the particles are calculated using interatomic potentials or force fields. By recording and analysing the coordinates, velocities and potentials of the particles in the system, the dynamic processes and statistical properties can be tracked and studied in detail. The method is applied mostly in materials science [2,3], chemical physics [4,5], biophysics [6] and drug design [7]. The MD method is the main approach used in this thesis. Here, we introduce the main simulation algorithms for the MD method.

A series of algorithms control an MD simulation. These algorithms include integration, thermostats and barostats, boundary conditions, neighbour searching, force fields and potentials, etc. The integrator defines the numerical solving process of the equations of motion. The thermostat or barostat are introduced to keep the system under the desired temperature or pressure settings to mimic the experimental conditions. The boundary condition specifies the type of constraints imposed on the simulation box. The periodic boundary condition is frequently used to approximate an extensive system using a small, infinitely repeated unit cell. The neighbour searching algorithm is used to find the pairs of atoms within a predefined or adaptive cutoff radius to analyse the results. Force field or

inter-atomic potentials need to be set in advance to obtain the inter-atomic force during the simulations.

3.1.1 Equations of motion and integrator

In a system of N particles with coordinates $\mathbf{r}_i$, $i = 1$, ... , N, the equation of motion is Newton's second law:

$$m_i \frac{\mathrm{d}^2 \mathbf{r}_i}{\mathrm{d}t^2} = \mathbf{F}_i, \tag{3-1}$$

where m_i and $\mathbf{F}_i$ are the mass of the particle i and the force on it, respectively.

A numerical solution to Equation 3-1 is given by Verlet [8]:

$$\mathbf{r}_i(t + \Delta t) = 2\mathbf{r}_i(t) - \mathbf{r}_i(t - \Delta t) + \mathbf{a}_i(t)\Delta t^2, \tag{3-2}$$

with the associated velocity being calculated using the central difference:

$$\mathbf{v}_i(t) = \frac{\mathbf{r}_i(t + \Delta t) - \mathbf{r}_i(t - \Delta t)}{2\Delta t}, \tag{3-3}$$

where $\mathbf{a}_i = \mathbf{F}_i/m_i$ is the acceleration of the particle i. The Verlet algorithm approximates the Newton's equations of motion by using Taylor series expansions of the particle's position ($\mathbf{r}_i$) with respect to time (t). The Verlet-type integrator is the most commonly used algorithm in molecular dynamics [9]. It is time-reversible with a local error on the order of $\mathcal{O}(\Delta t^4)$ in the position and $\mathcal{O}(\Delta t^2)$ in the velocity [10].

Some modifications of the original Verlet integrator have been developed to improve the efficiency. The leapfrog method [11] and the velocity-Verlet method [12] are two successful integrator methods that perform integration over half of the time step.

The leapfrog integration approximates the Newton equation by updating positions and velocities in a staggered manner, ensuring energy conservation and time-reversibility in molecular dynamics simulations. The equations for updating the positions and velocities are

$$\begin{cases} \mathbf{r}_i(t + \Delta t) = \mathbf{r}_i(t) + \mathbf{v}_i\left(t + \frac{1}{2}\Delta t\right)\Delta t, \\ \mathbf{v}_i\left(t + \frac{1}{2}\Delta t\right) = \mathbf{v}_i\left(t - \frac{1}{2}\Delta t\right) + \mathbf{a}_i(t)\Delta t. \end{cases} \tag{3-4}$$

As shown in Equation 3-4, $\mathbf{r}_i$ at integer time steps and $\mathbf{v}_i$ at half-integer time steps jump over each other in the computing sequence, which is where the name 'leapfrog' comes from.

The velocity at the integer time step is obtained by averaging the neighbouring velocities of half-integer steps:

$$\mathbf{v}_i(t) = \frac{\mathbf{v}_i\left(t + \frac{1}{2}\Delta t\right) - \mathbf{v}_i\left(t - \frac{1}{2}\Delta t\right)}{2}. \tag{3-5}$$

The velocity-Verlet method, however, calculates the time and velocity at the same value of the time variable:

$$\begin{cases} \mathbf{r}_i(t + \Delta t) = \mathbf{r}_i(t) + \mathbf{v}_i(t)\Delta t + \frac{1}{2}\mathbf{a}_i(t)\Delta t^2, \\ \mathbf{v}_i(t + \Delta t) = \mathbf{v}_i(t) + \frac{\mathbf{a}_i(t) + \mathbf{a}_i(t+\Delta t)}{2}\Delta t. \end{cases} \tag{3-6}$$

It can be shown that the error of both the leapfrog and the velocity-Verlet methods is of the same order as the error of the basic Verlet method.

The leapfrog and velocity-Verlet methods are very efficient at producing the evolving positions and velocities with time, and they are easy to program. They have been employed by many open-source and commercial packages. The leapfrog method is the default integrator in open-source packages like GROMACS [13], while the velocity-Verlet method is implemented by open-source packages like LAMMPS [14] and commercial packages like MBN Explorer [15, 16]. Other integrators that are not Verlet-like integrators, like the Runge-Kutta method, are less frequently used because of their complexity and high computational resource demands [10].

3.1.2 Thermostat and barostat

If the equations of motion are solved exactly by the Verlet integrator, the energy of the system will be conserved. Thus, the ensemble of the system will be an micro-canonical (NVE) ensemble in which the number of particles (N), the volume of the simulation box (V) and the total energy (E) are all kept constant. However, in most experimental circumstances, the system is kept under certain temperature or pressure conditions. Therefore, the integrator needs to be modified to include external temperature and pressure by employing thermostats and barostats, respectively. A thermostat is an algorithm that controls or maintains a constant temperature within the simulated system, thereby mimicking the behavior of the system in a heat bath, while a barostat is an algorithm that maintains a desired pressure within the simulated system.

To control the temperature T to the target T_0, a direct scaling of the velocities of the particle is an obvious way. The instantaneous value of the temperature T is related to the kinetic energy E_k as follows:

$$E_k = \sum_i \frac{1}{2} m_i \mathbf{v}_i^2 = \frac{k_B T}{2} N_{df}. \tag{3-7}$$

where m_i and $\mathbf{v}_i$ are the masses and velocities of the particles, respectively. k_B is the Boltzmann constant and N_{df} is the total number of degrees of freedom. According to Equation 3-7, if the velocities are multiplied by a factor λ which equals to $\sqrt{T_0/T}$, the temperature T of the system will be scaled to the target T_0. However, this approach is not acceptable because this will set the temperature to a constant value T_0, eliminating the energy fluctuations present in the canonical ensembles, leading to an incorrect representation of the system's behavior. Berendsen [17] provides a more reasonable approach to correcting the temperature T to the target value T_0. In such an approach, the temperature of the system is corrected such that the deviation exponentially decays with a time constant τ_T:

$$\frac{\mathrm{d}T}{\mathrm{d}t} = \frac{T_0 - T}{\tau_T}. \tag{3-8}$$

According to this, the factor λ that is used to scale the velocities of the particles can be determined:

$$\lambda = \sqrt{1 + \frac{\Delta t}{\tau_T} \left(\frac{T_0}{T} - 1 \right)}. \tag{3-9}$$

We can see that, although the Berendsen thermostat is less aggressive than a direct scaling, the suppression of the energy fluctuation is still inevitable. Meanwhile, it does not generate an exact canonical ensemble [18], but for large systems on the order of thousands of atoms/molecules, the approximation yields approximately correct results for most calculated properties [18].

Berendsen also has his own barostat [17], which uses a similar approach to his thermostat. The pressure of the system is controlled as follows:

$$\frac{\mathrm{d}P}{\mathrm{d}t} = \frac{P_0 - P}{\tau_P}. \tag{3-10}$$

Berendsen coupling approaches are simple and effective. However, in many cases, especially for smaller systems where energy fluctuations are more significant, a more

accurate ensemble is needed. In such cases, the Nosé-Hoover thermostat [19, 20] and the Parrinello-Rahman barostat [21, 22] are better choices; they solve the problem by introducing a fictitious dynamical variable to mimic the external temperature or pressure.

The Nosé-Hoover thermostat introduces a friction ζ, which slows down or accelerates particles until the temperature is equal to the desired value. The equations of motion are modified as follows:

$$m_i \frac{\mathrm{d}^2 \mathbf{r}_i}{\mathrm{d}t^2} = \mathbf{F}_i - \zeta m_i \mathbf{v}_i, \tag{3-11}$$

with

$$\frac{\mathrm{d}\zeta(t)}{\mathrm{d}t} = \frac{1}{Q} \left[\sum_{i=1}^{N} \frac{1}{2} m_i \mathbf{v}_i^2 - \frac{3N+1}{2} k_B T_0 \right], \tag{3-12}$$

where Q determines the relaxation of the dynamics of the friction $\zeta(t)$, T_0 is the target temperature and N is the number of particles. In a steady state, where $\mathrm{d}\zeta/\mathrm{d}t = 0$, the kinetic energy is $(3N+1)k_B T_0/2$ because of equipartition (the factor is $3N+1$ instead of $3N$ because there is one more degree of freedom ζ). During the simulation, the temperature will tend toward the target value step by step, and the whole system maintains accurate canonical values.

The Parrinello-Rahman barostat works in a similar way to the Nosé-Hoover thermostat. It can be applied to crystals. The cell of the crystal can be completely described with three vectors $\mathbf{a}$, $\mathbf{b}$ and $\mathbf{c}$. By defining the box matrix $\mathbf{h} = [\mathbf{a}, \mathbf{b}, \mathbf{c}]$ and tensor $\mathbf{G} = \mathbf{h}^T \mathbf{h}$, the equation of motion under isotropic external pressure can be written as follows:

$$m_i \frac{\mathrm{d}^2 \mathbf{r}_i}{\mathrm{d}t^2} = \mathbf{F}_i - \mathbf{G}^{-1} \frac{\mathrm{d}\mathbf{G}}{\mathrm{d}t} m_i \mathbf{v}_i, \tag{3-13}$$

with

$$\mathbf{W} \frac{\mathrm{d}^2 \mathbf{h}}{\mathrm{d}t^2} = (P - P_0)\sigma, \tag{3-14}$$

where σ represents the conjugate vectors of $\mathbf{h}$ in reciprocal space ($\sigma = \mathbf{a} \cdot (\mathbf{b} \times \mathbf{c})(\mathbf{h}^T)^{-1}$) and $\mathbf{W}$ is the mass parameter matrix that describes the strength of the pressure coupling. The shape of the simulation box is allowed to change during the simulation.

Another widely used thermostat is the Langevin thermostat [23, 24]. In Langevin dynamics, atoms in the system are assumed to be embedded in a sea of fictional particles

of smaller size. The dynamics of the particles are described by the Langevin equation, which includes additional terms to account for the friction force and the noise terms:

$$m_i \frac{\mathrm{d}^2 \mathbf{r}_i}{\mathrm{d}t^2} = \mathbf{F}_i - \frac{1}{\tau_d} m_i \mathbf{v}_i + \sqrt{\frac{2 k_B T_0 m_i}{\tau_d}} \mathbf{R}_i(t), \qquad (3\text{-}15)$$

where T_0 is the target temperature, and τ_d is the characteristic viscous damping time, which describes the coupling strength of the temperature. $\mathbf{R}_i(t)$ is a delta-correlated stationary Gaussian process with zero mean that satisfies

$$\begin{cases} \langle \mathbf{R}_i(t) \rangle = 0, \\ \langle \mathbf{R}_i(t) \mathbf{R}_i(t') \rangle = \delta(t - t'), \end{cases} \qquad (3\text{-}16)$$

where δ is the Dirac delta. Langevin dynamics attempt to extend molecular dynamics to allow the friction caused by the jostling of solvent or air molecules and the perturbation of the system caused by occasional high velocity collisions. It is also an accurate canonical ensemble that is suitable for smaller systems.

3.1.3   Periodic boundary condition

A periodic boundary condition (PBC) is usually employed when we want to use the simulation of the unit cell to reasonably represent an infinite system by replicating it with its periodic images. This treatment works perfectly for highly ordered crystals but will introduce artifacts in other systems like liquid systems. Fortunately, such errors are usually very small in large systems with thousands or more atoms [1]. Under periodic boundary conditions, the linear momentum of the system is conserved, but angular momentum is not [25].

A PBC requires the unit cell to have a shape that will tile perfectly into a three-dimensional crystal. Obviously, a spherical or elliptical cell cannot be used. A cube or cuboid unit cell is the most intuitive and common choice. The PBC of a cuboid unit cell in three-dimensional space can be mathematically defined according to the smooth real

functions $\phi : \mathbb{R}^3 \to \mathbb{R}$ as follows:

$$
\begin{cases}
\frac{\partial^n}{\partial x^n} \phi(x_1, y, z) = \frac{\partial^n}{\partial x^n} \phi(x_2, y, z), \\[2mm]
\frac{\partial^n}{\partial y^n} \phi(x, y_1, z) = \frac{\partial^n}{\partial y^n} \phi(x, y_2, z), \\[2mm]
\frac{\partial^n}{\partial z^n} \phi(x, y, z_1) = \frac{\partial^n}{\partial y^n} \phi(x, y, z_2),
\end{cases}
\tag{3-17}
$$

for all $n = 1,\ 2,\ ...$, where x_1, x_2, y_1, y_2, z_1 and z_2 are the coordinates of the boundary along the x, y and z axes, respectively [26].

3.1.4 Cutoff and neighbouring list

In a system with N particles, the number of interacting pairs is on the order of $\mathcal{O}(N^2)$. Therefore, the computational cost will be quadrupled when the size of the system is doubled, which is not acceptable, especially for large systems. To speed up the simulation with a reasonable accuracy, the cutoff radius for short-range interactions is usually fixed at a constant value (usually 10–15 Å). With this approach, the computational cost will proportionally increase as the number of the particles N increases, which significantly improves the efficiency of the simulation.

Meanwhile, in a large system of hundreds or thousands of particles, only a few particles (~ 10) will be located within the cutoff radius. In this case, it will be very important to locate these interacting neighbours efficiently in order to reduce the computational costs [1]. One of the searching algorithms is called the Verlet list method, which uses a less frequently updated neighbour list with a radius slightly larger than the cutoff radius. Another approach is the cell-list method, which divides the simulation box into many smaller cells so that the neighbours can be found in adjacent cells. The cell-list method is more intuitive and efficient for large systems [27].

3.1.5 Force field and potentials

In molecular dynamics, the interaction forces between particles are often determined by a series of potential functions that need to be defined before the simulation. These potentials can be empirical (from experiments) or calculated by other ab-initio methods.

The empirical potentials used in chemistry are called force fields [28]. They consist of a series of bonded forces associated with chemical bonds, bond angles and bond dihedrals and non-bonded forces associated with van der Waals forces and electrostatic charge. The parameters in these potentials, like the atomic charge, van der Waals parameters, equilibrium bound length, angle, etc., are obtained by fitting detailed quantum chemical simulations or experimental properties like spectroscopic measurements.

The potential functions representing the non-bonded energy are formulated as a sum over interactions between the particles of the system. A simple approach is the pair potential: the total potential energy is the sum of the potential energy between pairs of atoms. An example of this is the Lennard-Jones potential, which is used for van der Waals interaction [29]:

$$E_{LJij} = 4\epsilon_{ij} \left[\left(\frac{\sigma_{ij}}{r_{ij}} \right)^{12} - \left(\frac{\sigma_{ij}}{r_{ij}} \right)^{6} \right]. \tag{3-18}$$

where r_{ij} is the distance between two interacting particles, and ϵ_{ij} (usually referred to as 'dispersion energy') and σ_{ij} (often referred to as 'size of the particle') are the depth of the potential well and the distance at which the potential energy between the atoms is zero.

Another example is the Coulomb potential:

$$E_{Cij} = \frac{q_i q_j}{4\pi\epsilon_0 r_{ij}}. \tag{3-19}$$

where r_{ij} is the distance between two interacting particles, q_i and q_j are the charges on particle i and j, ϵ_0 is the electric constant.

In addition to the pair potential, there is another form of potential called the many-body potential in which the potential energy includes the effects of three or more particles interacting with each other [30]. In many-body potentials, the potential energy is calculated explicitly as a combination of higher-order terms, so the total potential energy is not a sum over pairs of atoms. In these potentials, the angles between the atoms become an important factor.

One such many-body potential that has proven to be effective in describing the properties of metallic systems is the Gupta potential [31,32]. The Gupta potential is based on the concept of broken-bond counting, where the potential energy of a system is determined by

Table 3-1 Parameters for some fcc transition metals in Gupta potential [32].

	A (eV)	ξ (eV)	p	q
Ni	0.0376	1.070	16.999	1.189
Cu	0.0855	1.224	10.960	2.278
Rh	0.0629	1.660	18.450	1.867
Pd	0.1746	1.718	10.867	3.742
Ag	0.1028	1.178	10.928	3.139
Ir	0.1156	2.289	16.980	2.691
Pt	0.2975	2.695	10.612	4.004
Au	0.2061	1.790	10.229	4.036
Al	0.1221	1.316	8.612	2.516
Pb	0.0980	0.914	9.576	3.648

considering the attractive and repulsive contributions of the pairwise interactions between atoms. The attractive term originates from the metallic bonding, while the repulsive term arises due to the electron cloud overlap between the neighboring atoms. The general form of Gupta potential can be expressed by the following equation:

$$E_{Gupta} = A \sum_{i \neq j}^{N} v(r_{ij}) - \xi \sum_{i=1}^{N} \sqrt{\rho(r_i)}. \tag{3-20}$$

where $v(r_{ij})$ is the pairwise part of the potential defined as:

$$v(r_{ij}) = \exp\left[-p\left(\frac{r_{ij}}{r_0} - 1\right)\right]. \tag{3-21}$$

The second term in Equation 3-20 describes the nonlocal effects of the interatomic interaction. The function $\rho(r_i)$ is expressed by:

$$\rho(r_i) = \sum_{j=1, j \neq i}^{N} \exp\left[-2q\left(\frac{r_{ij}}{r_0} - 1\right)\right]. \tag{3-22}$$

where r_0 is the lattice constant of the atoms, A, p, ξ and q are all parameters that are determined by fitting the potential to experimental data or ab initio calculations. The parameters for some fcc transition metals are shown in the Table 3-1 [32].

The Brenner potential [33] is another many-body potential which was initially derived

to study the carbon-based materials. This potential has the following form:

$$E_{Brenner} = \frac{1}{2} \sum_{i \neq j} V_{ij}$$

$$(3\text{-}23)$$

$$V_{ij} = f_C(r_{ij}) \left[f_R(r_{ij}) + b_{ij} f_A(r_{ij}) \right]$$

Here, V_{ij} is the bond energy between particle i and j. The indices i and j run over the atoms of the system, and r_{ij} is the distance form atom i to atom j. the $1/2$ is included to account for double counting of pairwise interactions. The function f_R represents a repulsive pair potential and f_A represents an attractive pair potential associated with bonding. The function f_C is a smooth cutoff function to limit the range of the potential for efficiency in computational effort. The function b_{ij} represents a measure of the bond order. These functions have the following expressions:

$$f_C(r_{ij}) = \begin{cases} 1, & r_{ij} \leq R_1 \\ \frac{1}{2}\left[1 + \cos\left(\frac{r_{ij} - R_1}{R_2 - R_1}\pi\right)\right], & R_1 < r_{ij} \leq R_2 \\ 0, & r_{ij} > R_2 \end{cases}$$

$$(3\text{-}24)$$

This cutoff function has continuous value and derivative for all r, and goes from 1 to 0 as r_{ij} goes from R_1 to R_2.

For the repulsive and attractive term:

$$f_R(r_{ij}) = \frac{D_e}{S-1} \exp\left[-\sqrt{2S}\beta(r_{ij} - R_0)\right]$$

$$f_A(r_{ij}) = \frac{D_e S}{S-1} \exp\left[-\sqrt{\frac{2}{S}}\beta(r_{ij} - R_0)\right]$$

$$(3\text{-}25)$$

where the well depth D_e, equilibrium distance R_0 and β are equal to the Morse potential parameters [34] and is independent from the parameter S. For the bond order term b_{ij}:

$$b_{ij} = \left[1 + \zeta_{ij}{}^n\right]^\delta$$

$$\zeta_{ij} = \sum_{k \neq i,j} f_C(r_{ik}) G(\theta_{ijk})$$

$$(3\text{-}26)$$

where $G(\theta_{ijk})$ depends on the angle θ_{ijk} between bonds formed by the atom pairs (i, j) and (i, k). In Brenner potential it has the following form:

$$G(\theta_{ijk}) = a_0 \left[1 + \frac{c_0{}^2}{d_0{}^2} - \frac{c_0{}^2}{d_0{}^2 + (1 + \cos\theta_{ijk})^2}\right]$$

$$(3\text{-}27)$$

Table 3-2 Parameters and the values of carbon for Brenner potential [33].

D_e (eV)	S	β (Å^{-1})	R_0 (Å)	δ	a_0	c_0	d_0	R_1 (Å)	R_2 (Å)
6.325	1.29	1.5	1.315	0.80469	0.011304	19	2.5	1.7	2.0

where a_0, c_0 and d_0 are related to the geometry of the lattice. From Equation 3-24 to 3-27, The parameters of the Brenner potential and their values for carbon are summarized in Table 3-2.

Another important potential for metallic system is the Embedded Atom Method (EAM) potential, which is developed by M. S. Daw and M. I. Baskes in the early 1980s [35]. The central concept of the EAM potential is that the energy of an atom in a metallic system can be represented by two contributions: the embedding energy, which is the energy needed to embed an atom into the electron density of its neighboring atoms and accounts for many-body effects depending on the local electron density at the atom's site, and the pair potential, which denotes the pairwise interaction between atoms, taking into account the repulsive forces from overlapping electron clouds and the attractive forces due to metallic bonding. The general form of the EAM potential is:

$$E_{EAM} = F_\alpha \left(\sum_{j \neq i} \rho_\beta(r_{ij}) \right) + \frac{1}{2} \sum_{j \neq i} \phi_{\alpha\beta}(r_{ij}) \tag{3-28}$$

where F_α (embedding energy), ρ_β (charge density), and $\phi_{\alpha\beta}$ (pair potential) are the tabulated functions which parametrize the interactions of atoms of type α and β by fitting to experimental or ab initio data.

3.2   Molecular dynamics simulation software

Through decades of research and development, many powerful tools have been created to handle the molecular dynamics simulation. Table 3-3 shows some commonly used molecular dynamics packages. In this table, "Model builder" means the package has some inbuilt tools that allow the users to build and manipulate models, "optimisation" means the package is capable of energy minimization and "MC" means the package is capable of performing either stand-alone or hybrid Monte Carlo simulations. Proprietary means

Table 3-3 MD simulation suites and their main features

Name	Model builder	Optimisation	MC	Licence
AMBER [36]	Yes	Yes	Yes	Proprietary and open source versions
CHARMM [37]	Yes	Yes	Yes	Proprietary and commercial
GROMACS [38]	No	Yes	No	Open source
LAMMPS [14]	Yes	Yes	Yes	Open source
Material Studio [39]	Yes	Yes	Yes	Proprietary
MBN Explorer [40]	Yes	Yes	Yes	Proprietary

the software has restrictions on usage, modification, and redistribution and commercial means the software is intended for profit.

Here, we introduce the relevant packages that are used in this thesis:

3.2.1 For Model building, visualization and analysis

VESTA The Visualization for Electronic and Structural Analysis (VESTA) program is a 3D visualization suite that allows users to view structural models, volumetric data, and crystal morphologies [41]. It has a number of unique features, including the ability to handle multiple structural models, volumetric data, and crystal morphologies in the same window, support for multiple tabs and windows, and the ability to deal with a virtually unlimited number of objects such as atoms, bonds, polyhedra, and polygons on isosurfaces. Additionally, VESTA supports lattice transformation using a matrix, which can be used to create superlattices and sublattices, and it can visualize interatomic distances and bond angles. It also offers high quality smooth rendering of isosurfaces and sections, and can export high-resolution graphic images that exceed the limitations of most video cards. A screenshot of the interface of VESTA is shown in Figure 3-1.

OVITO The Open Visualization Tool (OVITO) is a scientific visualization and data analysis solution for atomistic and other particle-based models [42]. OVITO is a platform-independent software that uses hardware-accelerated rendering based on the OpenGL standard to display a large number of atoms in realtime, even on entry-level graphics

60
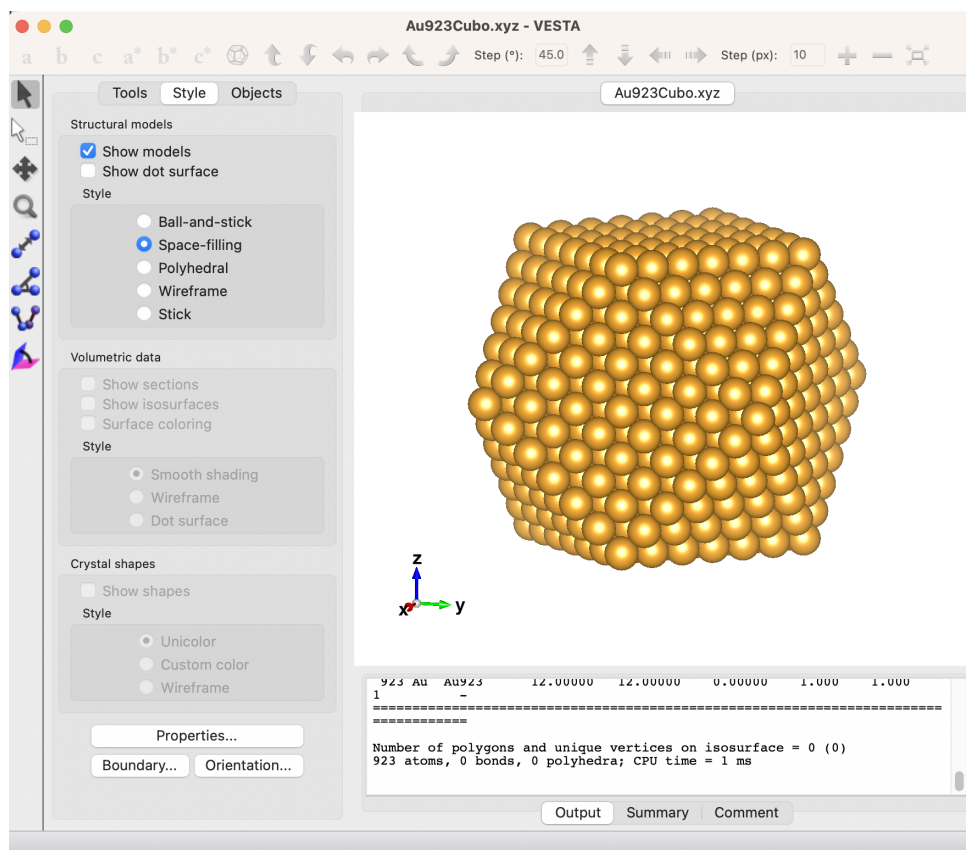
Figure 3-1 Au$_{923}$ cuboctahedral cluster displayed in space-filling mode in VESTA
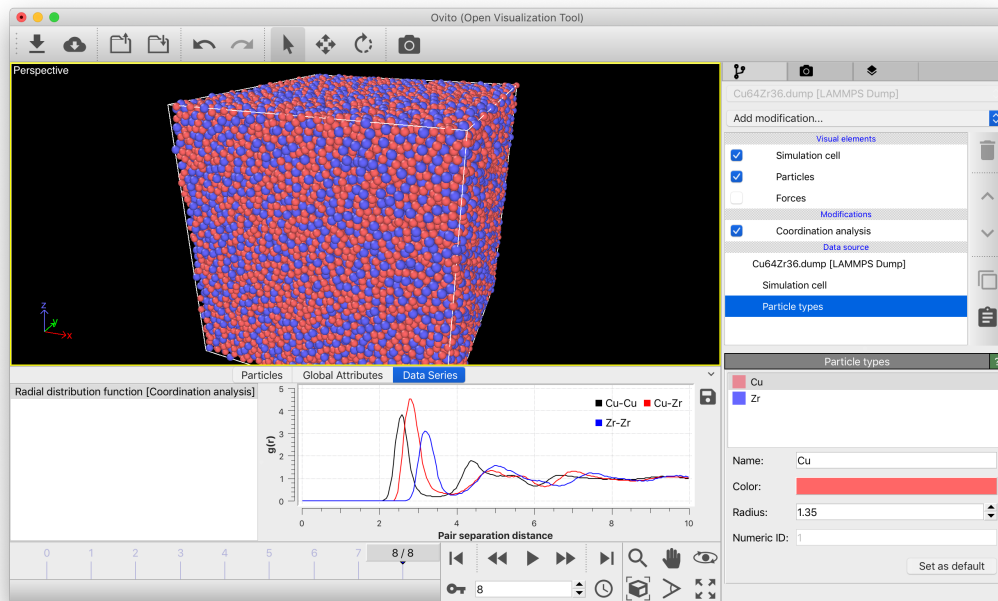
Figure 3-2 Cu-Zr alloy displayed in OVITO. A radial distribution function is shown for each component pair

cards. It can handle multi-timestep data files and allows users to visualize the evolution of a system over time, as well as create fly-through movie animations and display three-dimensional polygonal data and geometric shapes. OVITO has a plug-in based architecture that enables users to easily extend the software to meet their specific needs and add import and export capabilities for various file formats. It also features a rich graphical user interface and a scripting interface based on Python for batch processing and integration into custom tool chains. OVITO is available on all major operating systems, including Windows, macOS and Linux. A screenshot of the interface of OVITO is shown in Figure 3-2.

3.2.2 For Molecular dynamics simulations

LAMMPS The Large-scale Atomic/Molecular Massively Parallel Simulator (LAMMPS) [14] is a classical molecular dynamics (MD) tool that models ensembles of particles in a liquid, solid or gaseous state. It can model atomic, polymeric, biological, solid-state (metals, ceramics, oxides), granular, coarse-grained or macroscopic systems using a variety of

interatomic potentials (force fields) and boundary conditions [43]. It can model 2D or 3D systems with only a few particles and systems with millions or billions of particles.

LAMMPS is written in C++ and requires a compiler that is at least compatible with the C++-11 standard. It can be built and run on a laptop or desktop machine, but it is designed for parallel computers. It will run in serial and on any parallel machine that supports the MPI message-passing library.

LAMMPS provides a full working flow of molecular dynamics simulation, from building the model to analysing the results. It supports a large variety of potentials and has good force-field compatibility with other simulation tools like AMBER and GROMACS. It is coupled to many analysis tools and engines as well. For computing efficiency, LAMMPS uses neighbour lists (Verlet lists) to keep track of nearby particles [44]. The lists are optimised for systems with particles that repel at short distances, so that the local density of particles never grows too large.

The high customizability of LAMMPS makes it a versatile tool to apply novel methodologies in simulations. In the following example [45], an efficient, transferable, and interpretable machine learning force fields is developed for gold nanoparticles based on data gathered from Density Functional Theory calculations. This potential is applied on Au_{6266} nanoparticles to carry out molecular dynamics simulations with LAMMPS. The simulation results under different temperature conditions are shown in Figure 3-3 together with the temperature-dependent radial distribution of the fraction of LI (liquid inner) and of LS (liquid surface) local atomic environment. It can be observed that the melting transition initiates at the outer layer, and later spreads to the inner region.

MBN Explorer and MBN Studio MesoBioNano Explorer (MBN Explorer) is a software package for molecular dynamics simulations, structure optimisation and kinetic Monte Carlo simulations [15]. It is designed for the multiscale computational analysis of the structure and dynamics of atomic clusters and nanoparticles, biomolecules and nanosystems, nanostructured materials, different states of matter and various interfaces. MBN Studio is a special multi-task software toolkit with a graphical user interface that was developed to facilitate setting up and starting MBN Explorer calculations, monitor-
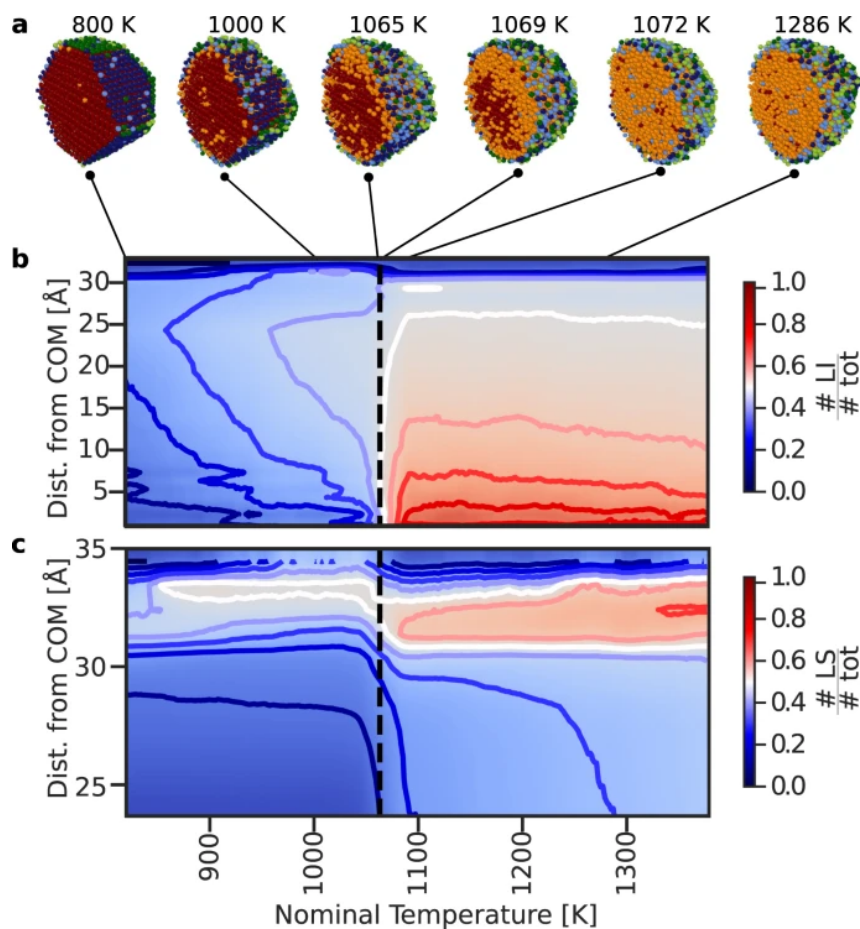
Figure 3-3 The simulation result of gold particles with a machine learning force field [45] (a) Snapshots of Au_{6266} simulated using the rPBE ML-FF at different nominal simulation temperatures, with atoms coloured according to the clustering algorithm. (b),(c) Average fraction of LI (b) and LS (c) local atomic environments as a function of the radial distance from the center of mass (y-coordinate), and of the nominal system temperature (x-coordinate). The bold coloured lines in (b, c) indicate the isosurfaces in the plot, from 0 to 1 every 0.1, while the black dashed line indicates the melting temperature of the nanoparticle (1065 K).
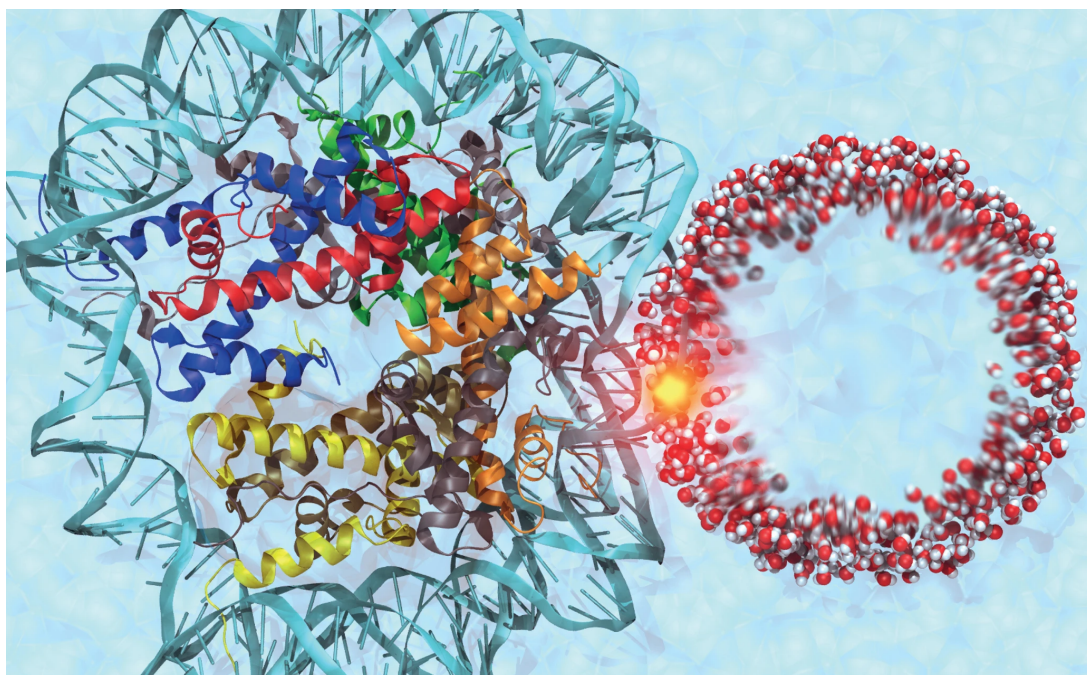
Figure 3-4 A figure from [46]. In this artistic depiction, a cylindrical shock wave front in water (on the right) interacts with a nucleosome (on the left) that has a segment of a DNA molecule on its surface. The ion's path is the axis of the cylinder, which is perpendicular to the plane of the figure. The yellow dot indicates where damage occurs. The medium is very dense in the region following the wave front and is rarefied in the wake.

ing their progress and examining the calculation results. These software packages were developed by the MBN Research Center.

MBN Explorer is suitable for classical molecular dynamics, irradiation-driven molecular dynamics, Monte Carlo, Euler and relativistic dynamics simulations of a large variety of molecular systems in a solid, liquid or gaseous state. It includes a large variety of interatomic potentials and allows one to model very different molecular systems, such as atomic clusters and nanoparticles, biomolecular systems, nanostructured materials, composite materials and material interfaces. The nice graphical interface from MBN Studio makes the model-building and analysis process very intuitive and extensively simplifies the workflow of the simulation.

This following work [46] demonstrates the capability of the MBN Explorer. In cells

that contain a nucleus, DNA is stored in structures called chromatin fibers. These fibers are made up of units called nucleosomes, which are octamers (eight units) of histone proteins wrapped in a double helix of DNA. MD simulations are carried out to study how a shock wave created by an ion traveling through a tissue-like medium interacts with a piece of DNA that is attached to the surface of a nucleosome. This is shown in Figure 3-4. The local heating of the medium near ion paths can lead to impressive effects. Through our MD simulations, we have seen that a shock wave created by an ion traveling through a tissue-like medium can produce stresses strong enough to break covalent bonds in DNA under certain circumstances.

References

[1] D. C. Rapaport, *The Art of Molecular Dynamics Simulation*. Cambridge University Press, Apr 2004.

[2] M. L. Klein and W. Shinoda, "Large-scale molecular dynamics simulations of self-assembling systems," *Science*, vol. 321, pp. 798–800, Aug 2008.

[3] F. Grasselli, L. Stixrude, and S. Baroni, "Heat and charge transport in H2O at ice-giant conditions from ab initio molecular dynamics simulations," *Nature Communications*, vol. 11, no. 1, 2020.

[4] P. C. T. Souza, R. Alessandri, J. Barnoud, S. Thallmair, I. Faustino, F. Grünewald, I. Patmanidis, H. Abdizadeh, B. M. H. Bruininks, T. A. Wassenaar, P. C. Kroon, J. Melcr, V. Nieto, V. Corradi, H. M. Khan, J. Domański, M. Javanainen, H. Martinez-Seara, N. Reuter, R. B. Best, I. Vattulainen, L. Monticelli, X. Periole, D. P. Tieleman, A. H. de Vries, and S. J. Marrink, "Martini 3: A general purpose force field for coarse-grained molecular dynamics," *Nature Methods*, vol. 18, pp. 382–388, Apr 2021.

[5] R. F. Ribeiro, L. A. Martínez-Martínez, M. Du, J. Campos-Gonzalez-Angulo, and J. Yuen-Zhou, "Polariton chemistry: Controlling molecular dynamics with optical cavities," *Chemical Science*, vol. 9, no. 30, pp. 6325–6339, 2018.

[6] B. Yang, K. Wei, C. Loebel, K. Zhang, Q. Feng, R. Li, S. H. D. Wong, X. Xu, C. Lau, X. Chen, P. Zhao, C. Yin, J. A. Burdick, Y. Wang, and L. Bian, "Enhanced mechanosensing of cells in synthetic 3D matrix with controlled biophysical dynamics," *Nature Communications*, vol. 12, p. 3514, Dec 2021.

[7] C. Choudhury, U. D. Priyakumar, and G. N. Sastry, "Dynamics based pharmacophore models for screening potential inhibitors of mycobacterial cyclopropane synthase," *Journal of Chemical Information and Modeling*, vol. 55, pp. 848–860, Apr 2015.

[8] L. Verlet, "Computer "experiments" on classical fluids. I. Thermodynamical properties of Lennard-Jones molecules," *Physical Review*, vol. 159, pp. 98–103, Jul 1967.

[9] N. Grønbech-Jensen and O. Farago, "A simple and effective Verlet-type algorithm for simulating Langevin dynamics," *Molecular Physics*, vol. 111, pp. 983–991, Apr 2013.

[10] William H. Press, S. A. Teukolsky, W. T. Vetterling, and B. P. Flannery, *Numerical Recipes 3rd Edition: The Art of Scientific Computing*. Cambridge University Press, 3rd ed., 2007.

[11] R. W. Hockney, "The potential calculation and some applications," *Methods in Computational Physics*, vol. 9, pp. 135–211, 1970.

[12] W. C. Swope, H. C. Andersen, P. H. Berens, and K. R. Wilson, "A computer simulation method for the calculation of equilibrium constants for the formation of physical clusters of molecules: Application to small water clusters," *The Journal of Chemical Physics*, vol. 76, pp. 637–649, Jan 1982.

[13] H. J. Berendsen, D. van der Spoel, and R. van Drunen, "GROMACS: A message-passing parallel molecular dynamics implementation," *Computer Physics Communications*, vol. 91, pp. 43–56, Sept 1995.

[14] A. P. Thompson, H. M. Aktulga, R. Berger, D. S. Bolintineanu, W. M. Brown, P. S. Crozier, P. J. in 't Veld, A. Kohlmeyer, S. G. Moore, T. D. Nguyen, R. Shan, M. J.

Stevens, J. Tranchida, C. Trott, and S. J. Plimpton, "LAMMPS - A flexible simulation tool for particle-based materials modeling at the atomic, meso, and continuum scales," *Computer Physics Communications*, vol. 271, p. 108171, 2022.

[15] I. A. Solov'yov, A. V. Yakubovich, P. V. Nikolaev, I. Volkovets, and A. V. Solov'yov, "MesoBioNano explorer-A universal program for multiscale computer simulations of complex molecular structure and dynamics," *Journal of Computational Chemistry*, vol. 33, no. 30, pp. 2412–2439, 2012.

[16] G. B. Sushko, I. A. Solov'yov, and A. V. Solov'yov, "Modeling MesoBioNano systems with MBN Studio made easy," *Journal of Molecular Graphics and Modelling*, vol. 88, pp. 247–260, 2019.

[17] H. J. C. Berendsen, J. P. M. Postma, W. F. van Gunsteren, A. DiNola, and J. R. Haak, "Molecular dynamics with coupling to an external bath," *The Journal of Chemical Physics*, vol. 81, pp. 3684–3690, Oct 1984.

[18] T. Morishita, "Fluctuation formulas in molecular-dynamics simulations with the weak coupling heat bath," *Journal of Chemical Physics*, vol. 113, pp. 2976–2982, Aug 2000.

[19] S. Nosé, "A molecular dynamics method for simulations in the canonical ensemble," *Molecular Physics*, vol. 52, pp. 255–268, Jun 1984.

[20] W. G. Hoover, "Canonical dynamics: Equilibrium phase-space distributions," *Physical Review A*, vol. 31, pp. 1695–1697, Mar 1985.

[21] M. Parrinello and A. Rahman, "Polymorphic transitions in single crystals: A new molecular dynamics method," *Journal of Applied Physics*, vol. 52, pp. 7182–7190, Dec 1981.

[22] M. Parrinello and A. Rahman, "Strain fluctuations and elastic constants," *The Journal of Chemical Physics*, vol. 76, pp. 2662–2666, Mar 1982.

[23] W. G. Hoover, A. J. C. Ladd, and B. Moran, "High-strain-rate plastic flow studied via nonequilibrium molecular dynamics," *Physical Review Letters*, vol. 48, pp. 1818–1820, Jun 1982.

[24] X. Shang and M. Kröger, "Time correlation functions of equilibrium and nonequilibrium Langevin dynamics: Derivations and numerics using random numbers," *SIAM Review*, vol. 62, pp. 901–935, Jan 2020.

[25] V. Kuzkin, "On angular momentum balance for particle systems with periodic boundary conditions," *ZAMM - Journal of Applied Mathematics and Mechanics / Zeitschrift für Angewandte Mathematik und Mechanik*, vol. 95, pp. 1290–1295, Nov 2015.

[26] D. Frenkel and B. Smit, *Understanding molecular simulation : from algorithms to applications*. Computational science (San Diego, Calif.), San Diego: Academic Press, 2nd ed ed., 2002.

[27] W. Mattson and B. M. Rice, "Near-neighbor calculations using a modified cell-linked list method," *Computer Physics Communications*, vol. 119, pp. 135–148, jun 1999.

[28] D. Frenkel, B. Smit, and M. A. Ratner, "Understanding molecular simulation: From algorithms to applications," *Physics Today*, vol. 50, pp. 66–66, Jul 1997.

[29] J. E. Lennard-Jones, "Cohesion," *Proceedings of the Physical Society*, vol. 43, pp. 461–482, sep 1931.

[30] J. F. Justo, M. Z. Bazant, E. Kaxiras, V. V. Bulatov, and S. Yip, "Interatomic potential for silicon defects and disordered phases," *Physical Review B*, vol. 58, pp. 2539–2550, Aug 1998.

[31] R. P. Gupta, "Lattice relaxation at a metal surface," *Physical Review B*, vol. 23, no. 12, pp. 6265–6270, 1981.

[32] F. Cleri and V. Rosato, "Tight-binding potentials for transition metals and alloys," *Physical Review B*, vol. 48, pp. 22–33, Jul 1993.

[33] D. W. Brenner, "Empirical potential for hydrocarbons for use in simulating the chemical vapor deposition of diamond films," *Physical Review B*, vol. 42, pp. 9458–9471, Nov 1990.

[34] P. M. Morse, "Diatomic molecules according to the wave mechanics. II. Vibrational levels," *Physical Review*, vol. 34, pp. 57–64, jul 1929.

[35] M. S. Daw, S. M. Foiles, and M. I. Baskes, "The embedded-atom method: A review of theory and applications," *Materials Science Reports*, vol. 9, pp. 251–310, Mar 1993.

[36] R. Salomon-Ferrer, D. A. Case, and R. C. Walker, "An overview of the Amber biomolecular simulation package," *Wiley Interdisciplinary Reviews: Computational Molecular Science*, vol. 3, pp. 198–210, mar 2013.

[37] B. R. Brooks, R. E. Bruccoleri, B. D. Olafson, D. J. States, S. Swaminathan, and M. Karplus, "CHARMM: A program for macromolecular energy, minimization, and dynamics calculations," *Journal of Computational Chemistry*, vol. 4, no. 2, pp. 187–217, 1983.

[38] D. Van Der Spoel, E. Lindahl, B. Hess, G. Groenhof, A. E. Mark, and H. J. Berendsen, "GROMACS: Fast, flexible, and free," *Journal of Computational Chemistry*, vol. 26, pp. 1701–1718, dec 2005.

[39] S. Sharma, P. Kumar, and R. Chandra, "Applications of BIOVIA materials studio, LAMMPS, and GROMACS in various fields of science and engineering," in *Molecular Dynamics Simulation of Nanocomposites using BIOVIA Materials Studio, Lammps and Gromacs*, pp. 329–341, Elsevier, 2019.

[40] I. A. Solov'yov, A. V. Korol, and A. V. Solov'yov, *Multiscale Modeling of Complex Molecular Structure and Dynamics with MBN Explorer*. Cham: Springer International Publishing, 2017.

[41] K. MOMMA, "Introduction to vesta." `https://jp-minerals.org/vesta/en/`, 2002. (Accessed on 12/20/2022).

[42] A. Stukowski, "Visualization and analysis of atomistic simulation data with OVITO-the Open Visualization Tool," *Modelling and Simulation in Materials Science and Engineering*, vol. 18, no. 1, p. 015012, 2010.

[43] Sandia National Laboratories, "Overview of LAMMPS," 2013.

[44] S. Plimpton, "Fast parallel algorithms for short-range molecular dynamics," Tech. Rep. 1, Sandia National Laboratories (SNL), Albuquerque, NM, and Livermore, CA (United States), May 1995.

[45] C. Zeni, K. Rossi, T. Pavloudis, J. Kioseoglou, S. de Gironcoli, R. E. Palmer, and F. Baletto, "Data-driven simulation and characterisation of gold nanoparticle melting," *Nature Communications*, vol. 12, p. 6056, oct 2021.

[46] E. Surdutovich, A. V. Yakubovich, and A. V. Solov'yov, "Biodamage via shock waves initiated by irradiation with ions," *Scientific Reports*, vol. 3, p. 1289, dec 2013.

Chapter 4 Nanofilament Fission Simulation in Neuromorphic Nanoparticle Networks

This chapter presents a systematic simulation of the breakage of a nanowire joining two nanoclusters, to represent a model of a synapse in a cluster-associated neuromorphic array. The focus of the simulation is to explore the effect of heat, which will be generated in the device through Joule heating.

4.1 Introduction

The assembling of interconnected, synapse-like switching devices represents one of the most promising neuromorphic computer architectures [1–4]; it is a new computing framework that is a promising solution to the problems of the contemporary computing method [5–13]. The memristor is the main elemental building block that acts as a neuron in such an architecture [14, 15]. A memristor is a nonlinear two-terminal electrical component that changes its resistance depending on the history of bias applied to it [16]. One of the main ways that this attractive feature can be obtained is through the formation and dissolution of nanoscale conductive filaments [17]. Depending on the specific application, the formed conductive filaments have a lifetime (or retention time) from a few microseconds [18, 19] to several months or even years [20, 21], allowing them to mimic both short-term and long-term plasticity in a neural network. Research shows that this process is strongly affected by surface atomic self-diffusion [22].

Lithographic methods are commonly used in fabricating memristors [23–25], but they are complicated and costly due to the need to deterministically create robust intra- and inter-device connections [26]. A simpler and possibly cheaper alternative is the random assembly of nanoscale building blocks to form the neuromorphic network from the bottom up [26]. In such an approach, nanoparticles (NPs) can be used as building blocks for memristors [27–31]. NP films produced by gas-phase cluster deposition technology have been reported to show non-ohmic electrical behaviour and reproducible resistive switching [30–33]. Such films have been deposited on a multitude of insulating materials, such

as silicon nitride [31, 32], silica [30], glass [26] or even paper [33]. Networks fabricated using this method show good robustness because their overall structure is fixed on the substrates [34], in contrast to some other approaches, like annealing a thin film to form clusters [35].

The mechanisms of the formation and breakage of the conducting connections between NPs are of the utmost importance, and intensive experimental research and simulations have been done on filamentary processes. In general, atomic-scale connections between the gaps in the NP film are created by electric field-induced surface diffusion and evaporation [34] and also by van der Waals forces between metal atoms. After its creation, this connection introduces electromigration, which eventually causes its breakage. There are numerous studies on the contribution of electromigration to the breakage or resistive switching of the nanowires (NWs) [36–39]. One alternative mechanism for the formation and dissolution of the conductive paths between particles is the Joule heating and temperature alternation caused by the variation of the current flow [28]. When a point contact in a complex nanoscale junction is smaller than the mean free path of electrons, high temperatures of up to thousands of kelvins can be induced by small voltage drops on the order of 100 mV [40].

The thermally induced breaking mechanism of NWs has been investigated in many reports [41–45]. Experiments show that large amounts of local heat can be generated in an NW network by the current [46], and the breaking process due to heat generation has been observed in-situ with TEM [47]. The effect of Joule heating on the breaking process of connections between particles in percolating systems is non-negligible, but there is a shortage of studies on this effect.

In this chapter, molecular dynamic (MD) simulations are performed on the breakage of nanofilaments to verify the contribution of Joule heating to the breaking mechanism. Gold NWs with different lengths, widths and structures were located between two nanometre-sized gold clusters in order to mimic a transit nanofilament. The bottom atoms of the gold clusters were fixed to imitate the interaction with the substrate. The temperature was gradually increased to find the breaking condition of each simulated system. Structural changes in the system were analysed. Our results show that the connection between NPs

73

can be broken by Joule heating, validating the mechanism in cluster-based neuromorphic devices.

4.2   Methodology

The MD simulations were performed with the MesoBioNano Explorer (MBN Explorer) software package [48]. The creation of the systems and the analysis of the results were performed with its accompanying multi-task toolkit, MBN Studio [49].

The simulated systems utilise a gold NW as the nanofilament connecting two Au_{1415} cuboctahedral clusters [50]. In cluster-based neuromorphic devices fabricated by cluster deposition technology, various structures and sizes coexist [28, 51]. The Au_{1415} cuboctahedral clusters have been chosen for their simplicity, as our primary focus is on the bridge portion of the system. The atoms on the bottom facet of the clusters were fixed to simulate the bonding with the substrate. The NWs have a face-centred-cubic (fcc) structure to represent relevant TEM observations [52]. The joints of the NW and the clusters are chosen at the central axis of the system on the (100) facet for simplicity in representation. Figure 4-1 (a) shows the structure of one of the simulated systems. Three kinds of NWs were simulated: a 4-Å-wide cubic NW (3 layers of atoms), an 8-Å-wide cubic NW (5 layers of atoms) and an 8-Å-wide truncated cubic NW in which the atoms on the four long edges of the NW have been removed. These shapes were chosen to reproduce experimental observations of Au NWs with a truncated cubic shape [52–54]. The cross sections of the three NWs are shown in Figure 4-1 (b)–(d).

We used the Gupta many-body potential [55] for our MD simulations. The parameters for Au–Au interaction were adopted from [56] with a cutoff radius of 7 Å to balance computational efficiency with accurate representation of Au-Au interactions. A brief introduction of the Gupta potential can be found in Chapter 3. The Langevin thermostat with a 1 ps damping time was used to control the temperature, ensuring efficient temperature regulation without excessive damping. An introduction of the Langevin thermostat can be found in Chapter 3. The timestep for the MD was set to 2 fs to maintain numerical stability, capture high-frequency vibrations, and balance accuracy with computational efficiency.
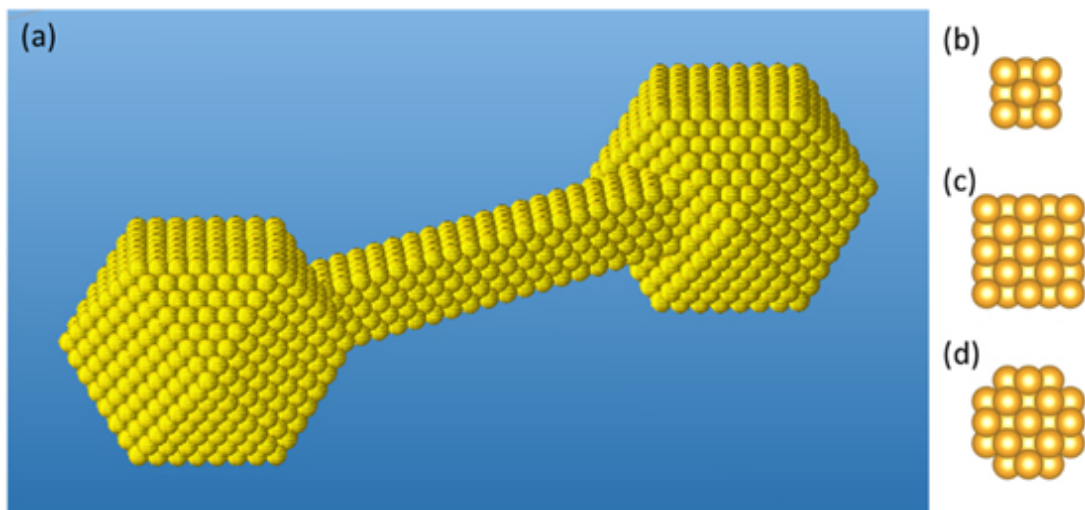
Figure 4-1 (a) The structure of one of the simulated systems. An 8-Å-wide, 60-Å-long cubic NW is connected to two cuboctahedral Au_{1415} clusters at each end. The atoms on the bottom surface of the clusters are fixed to represent the interaction between the cluster and the substrate. The cross sections of the following NWs are shown: (b) the 4-Å-wide cubic NW; (c) the 8-Å-wide cubic NW; (d) the 8-Å-wide truncated cubic NW.

At first, all the models underwent energy minimization using the conjugate gradient algorithm to obtain the lowest energy configuration at 0 K. Then, the MD simulations were initialised at room temperature (300 K) with random initial velocities. The initial velocities for each particle were generated using the following rule: the direction of the velocity vector was determined randomly, while the magnitude was calculated based on the equipartition theorem. [57]The models were heated at a rate of 20 K/ns for 30 ns. This heating rate balances computational efficiency and adequate sampling while providing the system with sufficient time to equilibrate at each temperature step. Each model was simulated seven times with random initial microstates [58] to reflect the statistical nature of the NW breakage process while balancing the limited computational resources available. The trajectory, the temperature and the potential energy changes for each simulation were recorded. To extract the crystallinity of the NWs and NPs during the heating process, an adaptive common neighbour analysis (a-CNA) [59] was performed using the OVITO visualisation and analysis software [60].

4.3 Results and discussion

4.3.1 Breakage process of the nanofilament

The breaking process of an 8-Å-wide, 60-Å-long cubic NW between two Au_{1415} clusters is illustrated in Figure 4-2. The temperatures stated under Figure 4-2 are nominal temperatures that correspond to the timestep of each frame, assuming linear scaling between the starting and ending temperatures. The typical evolution of the NW in the simulated systems can be summarised by the following stages: At low temperatures, the shape of the NW is changed minimally due to the thermal vibrations of the system. The NW loses its crystallinity and its outermost atoms begin to diffuse towards the clusters in a slow and gradual manner (Figure 4-2 (b)–(d)). As the temperature rises, the atomic movement towards the clusters becomes more pronounced, leaving the middle part of the NW thinner and more unstable (Figure 4-2 (e), (f)). Eventually, the NW breaks, and all the atoms left in the middle are pulled towards the clusters quickly and assimilated into them. Figure 4-2 (f) and (g) show the two trajectory frames before and after the breaking
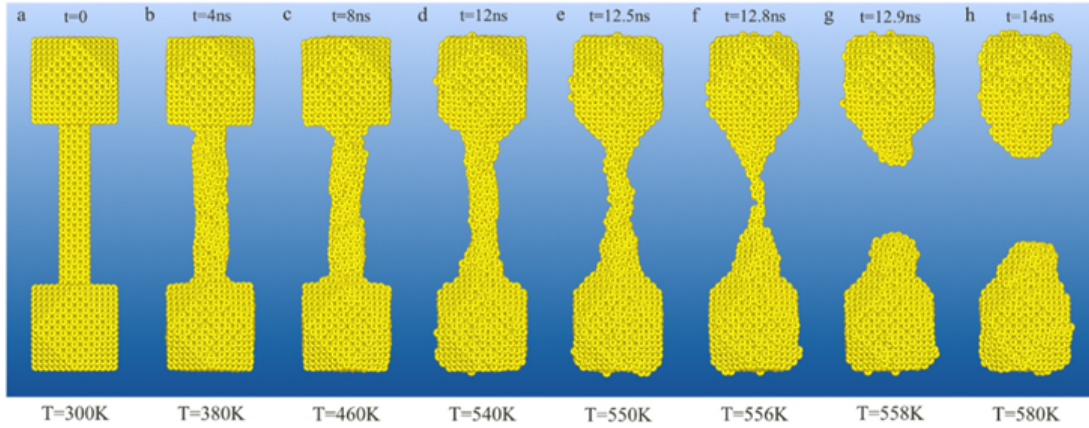
Figure 4-2 The breaking process of an 8-Å-wide, 60-Å-long cubic NW between two Au_{1415} clusters. The initial temperature is 300 K in panel (a). Panels (b)–(d) illustrate the perturbation region: some atoms of the NW are gradually pulled towards the clusters, and the NW's diameter is gradually reduced. In panels (e) and (f), the atoms of the NW move towards the clusters on two sides more quickly (within only $\sim$ 0.3 ns). The NW becomes even thinner in the middle. The fragmentation of the NW is shown in panel (f). After the breaking, the atoms of the NW coalesce into the NPs in panels (g)–(h).

event in our simulation. After the breaking, the aggregation continues but in a much slower manner (Figure 4-2 (h)) until the whole system melts and becomes amorphous.

The investigation of the effect of time on the breaking at constant temperatures would be an interesting study that would require a new set of simulations of these nanostructures at a series of temperatures close to the critical points mentioned in this work. This is a major undertaking that is beyond the scope of this work. However, we do believe that, even in a long simulation, this NW would not break at 550 K since it is clear from the figure 4-2 that, although it is largely non-crystalline, the NW is still thick enough to hold.

In this study, we consider the fragmentation of a nanowire on the atomistic level using the MD approach. This imposes limitations on the sizes of the studied systems, which are much smaller than the systems simulated in [44,45] using the kinetic Monte Carlo method. These two cited studies, [44] in 2D and [45] in 3D, demonstrated that micrometre-sized, metal NWs can break thermally into smaller islands, a phenomenon analogous to the

Rayleigh instability for a liquid cylinder. In our simulations, the NWs always break in the middle, and they do not disperse into multiple islands. This is caused by the strong surface diffusion current towards the clusters, which reduces the thickness of the NW in a gradual way. Additionally, by fixing the bottom of the cluster, we assume a much stronger interaction between the cluster and the substrate than that between the cluster and the bridge. This leads to a strong rigidity at the cluster base, which also contributes to the observed breaking pattern.

4.3.2   Structural analysis

A structural analysis can reveal further details of the mechanism of the breaking of the NW. Figure 4-3 shows the results of this analysis for some critical frames of the breaking process for NWs with different shapes and widths. The atoms of the inner shells of the Au_{1415} clusters and the connecting NWs are identified as being in the fcc structure initially. The atoms of the outer shells, on the other hand, cannot be assigned by the CNA algorithm to any of the crystalline structures due to their reduced coordination number [59]The CNA algorithm works by analyzing the local bonding environment of atoms based on their neighboring atoms, focusing on their common neighbors, to classify them into specific crystal structures. However, because the outer shell atoms have fewer neighboring atoms, the CNA algorithm struggles to properly identify their local crystal structures. As a result, the algorithm classifies these atoms as 'amorphous', despite the fact that they are visibly arranged in a crystalline formation.

In the thinner 4-Å-wide cubic NW (see Figure 4-3 (a1)–(a3)), the surface atoms constitute a large proportion of the whole NW; therefore, only a single row of atoms in the centre appear to be crystalline from the beginning. The algorithm can hardly show the structure change of the NW in this case. However, as more atoms aggregate towards the clusters, atoms marked as fcc or bcc will appear on both ends of the NW.

For the 8-Å-wide cubic NW (Figure 4-3 (c1)–(c3)) and 8-Å-wide truncated cubic NW (Figure 4-3 (b1)–(b3)), the structural changes during the breaking process are similar. During the perturbation stage, phase transitions from the fcc structure to the hcp structure appear diagonally at 2 and 3 places, respectively, dividing the NWs into equally sized
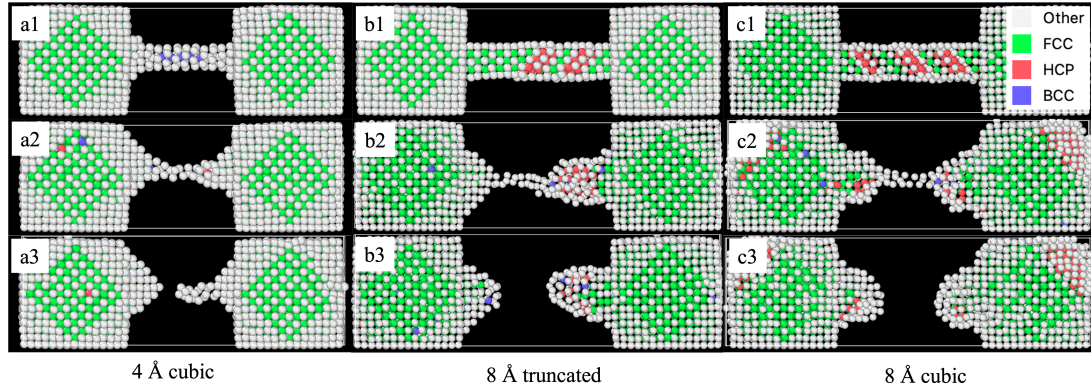
Figure 4-3 A comparison of the melting process between the systems with different NWs. Columns: (a) The 4 Å-wide 40 Å-long cubic NW. (b) The 8 Å-wide 40 Å-long truncated cubic NW. (c) The 8 Å-wide 40 Å-long cubic NW. Rows: (1) The frame during the perturbation period at t = 1 ns. (2) The frame before the NW breaks. (3) The frame after the NW breaks. The averaged breaking temperature for each structure is shown in Table 4-1.

parts. As the temperature rises and more atoms aggregate towards the NPs, the structural transitions between the fcc and hcp structures become more frequent and irregular due to the reduced dimensionality and increased surface-to-volume ratio. The middle part of the NW becomes too thin for the algorithm to recognise the structure, but inner atoms at the ends of the NW remain crystalline. These phase transitions are caused by the shearing strength generated by the perturbation. Marszalek et al. [61] confirmed experimentally that the sliding of crystal planes within the gold NWs will change the local structure from an fcc structure to an hcp structure. This phenomenon is known as plastic deformation in fcc metals.

In the studied systems, parts of the NW, specifically their two ends, remain crystalline throughout the whole process, a finding that differs from previous studies of the melting of fcc NWs [41, 42]. This is due to the presence of the clusters at the ends, which act as a recrystallisation area. The amorphisation of the NW and re-crystallisation at the two ends are also visible in the radial distribution function. Figure 4-4 shows snapshots of an 8-Å-wide and 40-Å-long cubic NW between two clusters and the corresponding radial distribution function. As all the lengths exhibit similar behavior, the 40-Å-long

79
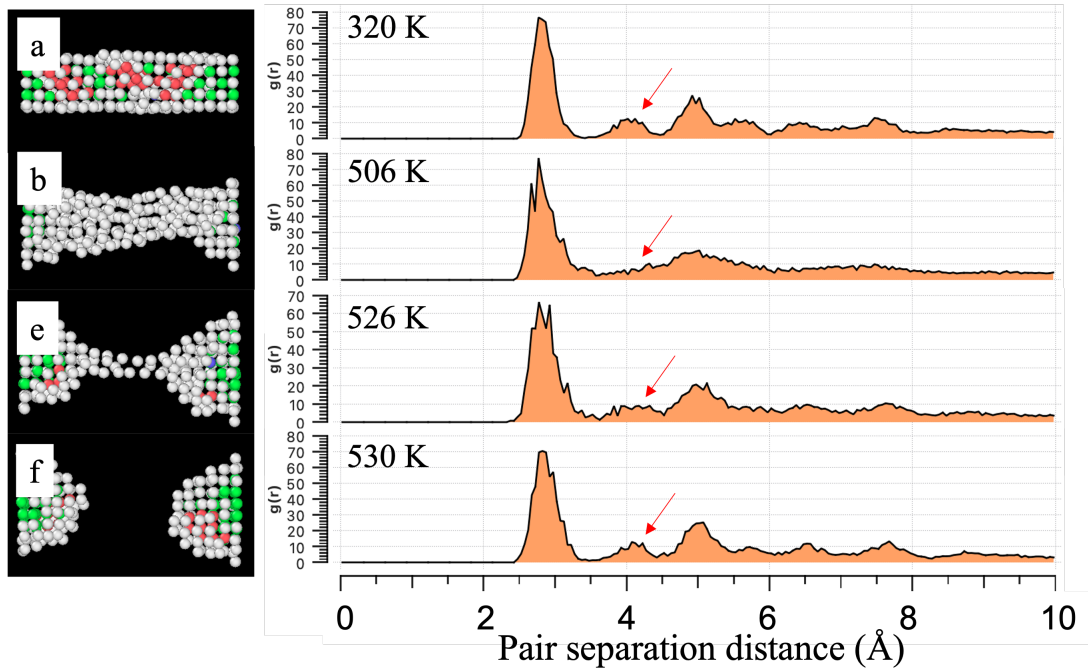
Figure 4-4 (a)–(d): The NW part of the 8-Å-wide, 40-Å-long cubic NW model and the corresponding radial distribution functions. (a) The NW at the perturbation region. (b) The $\sqrt{2}\sigma$ peak is reduced and (c) reaches its minimum. (d) The $\sqrt{2}\sigma$ peak reappears due to recrystallisation at the two NPs.

NWs is chosen for better representation in the figure. The nearest neighbour distance ($\sigma \approx 2.8$ Å) can be read from the first peak. Figure 4-4 (a) shows a crystalline state. In the perturbation region of the NW, the $\sqrt{2}\sigma$ peak of the function begins to decrease (Figure 4-4 (b)). The $\sqrt{2}\sigma$ peak reaches its minimum (Figure 4-4 (c)) and the form of the functions tends to resemble a liquid state. In Figure 4-4 (d), the NW is broken and the $\sqrt{2}\sigma$ peak gradually appears again. In general, the disappearance of the $\sqrt{2}\sigma$ peaks happens $10 \sim 30$ K below the breaking temperatures.

4.3.3 The breaking temperature

The average breaking temperatures of the simulated systems for NWs of different lengths and widths are shown in Table 4-1 and illustrated in Figure 4-5. The breaking temperatures in most cases vary from 400 to 650 K and show a dependence on the width,
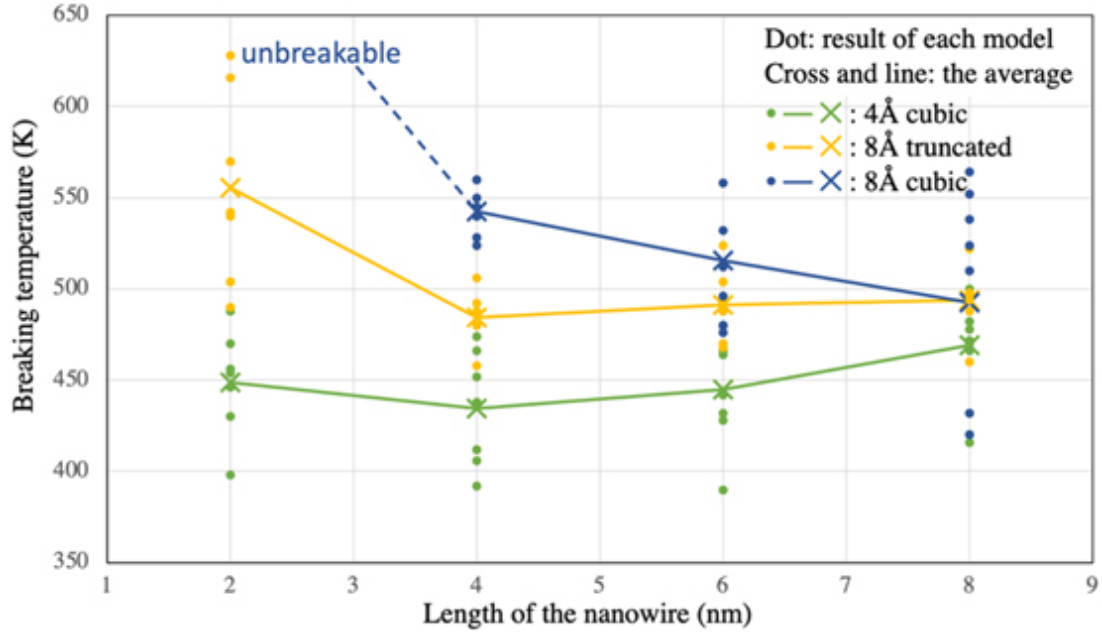
Figure 4-5 The breaking temperatures of all the individual systems (dots) and the average values of the breaking temperature for the specific length and width of the NW (crosses and lines).

length and structure of the NW.

Table 4-1 The average breaking temperatures of the different systems in this chapter

NW width and structure \ NW length	20 Å	40 Å	60 Å	80 Å
4 Å cubic	448 ± 29 K	434 ± 32 K	444 ± 32 K	469 ± 25 K
8 Å truncated cubic	556 ± 52 K	484 ± 15 K	491 ± 19 K	494 ± 18 K
8 Å cubic	Unbreakable	543 ± 13 K	516 ± 30 K	493 ± 64 K

Wider NWs will generally break at higher temperatures, and this becomes more pronounced when the NWs are shorter. The breaking points of 4-Å- and 8-Å-wide, 80-Å-long cubic NWs differ by ~ 25 K. This difference, however, is increased to over 70 K for an NW length of 60 Å and to 100 K for a length of 40 Å. The breaking point's dependence on the length varies according to the NW width and structure.

There is an exponential decrease in the breaking temperature as the length increases for the 8 Å NWs, with this behaviour being more pronounced for the cubic NW. The

81

breaking point of the truncated NW remains the same for lengths ≥ 40 Å (± 10 K). The 4 Å NWs always break at more or less the same temperature (± 25 K) regardless of their length. The slight increase in the breaking temperature of the 4-Å-wide cubic NW when the length is larger is within the expected fluctuations in an MD simulation. Finally, cubic NWs are more robust than the truncated NWs of the same width for lengths ≤ 60 Å, and the difference increases as the length is reduced. However, they appear to break at the same temperature at a length of 80 Å. The cubic NWs exhibit greater robustness than the truncated ones, which can be attributed to the difference in their structures. The truncated NWs are formed by removing atoms from the four long edges of the cubic ones (see Figure 4-1), resulting in a "narrower" geometry compared to the cubic NWs.

The 8-Å-wide, 20-Å-long cubic NW is an interesting case, as it retained its integrity throughout the whole simulationHowever, as the temperature continues to rise, both the cluster and the nanowire begin to melt, transforming into an amorphous state. Eventually, the two clusters merge into one, resulting in the system becoming a single, completely melted amorphous structure at around 850 K.

Experimental and simulation combined studies [45] show a relation between the break-up temperature of NWs and the corresponding bulk melting temperature of the material:

$$\frac{T_{nm}}{T_{mb}} = C_1 - \frac{C_2}{d_{NW}}, \tag{4-1}$$

where T_{mn} is the observed breaking temperature of the NW and T_{mb} is the melting temperature of the corresponding bulk material. C_1 and C_2 are constants related to the material (equal to 0.34 and 0.10 nm, respectively, for instance) and d_{NW} is the initial diameter of the NW. For the pure gold NWs with 4 Å and 8 Å diameters, respectively, the predicted breaking temperatures are 120 K and 290 K, respectively. This is rather different from our simulation result; this difference is due to the fact that the clusters play a large role in stabilising the NW in the middle.

The Rayleigh instability model, which describes the breaking up of liquid cylinders, has been used to describe the fragmentation process of NWs [43]. The linear dependence on NW width arises from the Rayleigh instability criterion, which states that a liquid column with a wavelength greater than the critical wavelength will be unstable and break

up. The critical wavelength is given by: $\lambda_c = 2\pi R$, where R is the radius of the liquid column (or NW width in this case). The applicability of this model is questionable in a fragmenting NW [44]; however, the behaviour observed in our MD simulations agrees qualitatively with the breakage behaviour of a liquid cylinder described using the Rayleigh model.

We can consider a short period around the breaking event as the stable state applicable to the Rayleigh model; for example, according to our description of the breaking process in Figure 4-2 (f)–(h), this state is 0.2 ns after the breaking of the NW. We measure the distance λ between the two parts of the broken NW, the diameter of the rest of the NW after the breaking event d_{sp} and its initial radius R_0, which is calculated using the average distance between the centre axis and the outer atoms; then, we calculate the λ/R_0 and d_{sp}/R_0 ratios for the more cylindrical 8-Å-wide truncated cubic NW, which are 8.2 and 2.5, respectively. Nichols and Mullins predicted λ/R_0 equals to 8.89 and d_{sp}/R_0, assuming constant volume, equals to 3.76 as the criteria for the surface diffusion-dominated breakup of a cylindrical wire as a result of harmonic surface perturbations [62].

Thus, our results are in good agreement with the Rayleigh model, suggesting that surface diffusion dominates the process. Deviations from the theoretical predictions are to be expected since our simulated system still does not have the ideal shape (an infinitely long cylindrical liquid) and isotropy that are assumed in the Rayleigh model, with atoms of the NW diffusing towards the clusters on the sides.

4.4   Conclusions

In this chapter, a series of model systems and MD simulations of the breaking process were created by heating the system to imitate the Joule heating mechanism in a cluster-based percolation system. The evolution of these systems was analysed in an effort to gain insight into the breaking process of nanofilaments connecting clusters.

Atoms in the NW will gradually aggregate towards the clusters on the sides, and the NW will eventually break at a certain temperature before the melting of the whole system. The a-CNA structural analysis result showed that a large part of the NW will remain crystalline, but the middle part of the NW will be molten during the breaking.

The breaking temperature's dependency on the geometric characteristics of the NWs was extracted. We find a strong dependence on the width and structure of the NW, while the length is found to be an important parameter in some but not all cases.

The NW breaking temperatures determined from the MD simulations presented in this study are much higher than the expected breaking temperatures for isolated NWs of the same diameter. We attribute this observation to the clusters on the ends that stabilise the NW in the middle. The Rayleigh model can be applied to analyse the molten part of the NW, and indicates that the breaking mechanism of the NW in the simulated systems is a consequence of diffusion processes.

This chapter showed that nanofilaments between clusters can be broken by Joule heating. Since structures similar to our model systems are applied in cluster-based neuromorphic systems, our work indicates that the Joule heating mechanism is likely to be an important factor in the breaking process of the percolation connections of these systems. We remark that a theoretical model needs to be established to account for filament breaking. Additionaly, more research is needed to understand the mechanism of filament formation, as well. We hope that this work will contribute towards that goal. Further research on the mechanism of filament formation can be found in the next chapter.

References

[1] A. M. Turing, "Intelligent machinery, a heretical theory," *Philosophia Mathematica*, vol. 4, no. 3, pp. 256–260, 1996.

[2] C. Mead, "Neuromorphic electronic systems," *Proceedings of the IEEE*, vol. 78, no. 10, pp. 1629–1636, 1990.

[3] H. C. Anderson, "Neural network machines," *IEEE Potentials*, vol. 8, pp. 13–16, Feb 1989.

[4] G. Rozenberg, T. Back, and J. N. Kok, *Handbook of Natural Computing*, vol. 1–4. Springer Berlin Heidelberg, 2012.

[5] K. He, X. Zhang, S. Ren, and J. Sun, "Deep residual learning for image recognition," in *Proceedings of the IEEE Computer Society Conference on Computer Vision and Pattern Recognition*, pp. 770–778, 2016.

[6] D. Silver, A. Huang, C. J. Maddison, A. Guez, L. Sifre, G. Van Den Driessche, J. Schrittwieser, I. Antonoglou, V. Panneershelvam, M. Lanctot, S. Dieleman, D. Grewe, J. Nham, N. Kalchbrenner, I. Sutskever, T. Lillicrap, M. Leach, K. Kavukcuoglu, T. Graepel, and D. Hassabis, "Mastering the game of Go with deep neural networks and tree search," *Nature*, vol. 529, no. 7587, pp. 484–489, 2016.

[7] O. Vinyals, I. Babuschkin, W. M. Czarnecki, M. Mathieu, A. Dudzik, J. Chung, D. H. Choi, R. Powell, T. Ewalds, P. Georgiev, J. Oh, D. Horgan, M. Kroiss, I. Danihelka, A. Huang, L. Sifre, T. Cai, J. P. Agapiou, M. Jaderberg, A. S. Vezhnevets, R. Leblond, T. Pohlen, V. Dalibard, D. Budden, Y. Sulsky, J. Molloy, T. L. Paine, C. Gulcehre, Z. Wang, T. Pfaff, Y. Wu, R. Ring, D. Yogatama, D. Wünsch, K. McKinney, O. Smith, T. Schaul, T. Lillicrap, K. Kavukcuoglu, D. Hassabis, C. Apps, and D. Silver, "Grandmaster level in StarCraft II using multi-agent reinforcement learning," *Nature*, vol. 575, no. 7782, pp. 350–354, 2019.

[8] M. Hilbert and P. López, "The world's technological capacity to store, communicate, and compute information," *Science*, vol. 332, no. 6025, pp. 60–65, 2011.

[9] Z. Cheng, C. Ríos, W. H. Pernice, C. David Wright, and H. Bhaskaran, "On-chip photonic synapse," *Science Advances*, vol. 3, p. e1700160, Sept 2017.

[10] A. Andrae and T. Edler, "On global electricity usage of communication technology: Trends to 2030," *Challenges*, vol. 6, pp. 117–157, Apr 2015.

[11] UN, "A new circular vision for electronics time for a global reboot." World Economic Forum, 2019, URL: https://www.weforum.org/reports/a-new-circular-vision-for-electronics-time-for-a-global-reboot.

[12] M. M. Waldrop, "The chips are down for Moore's law," *Nature*, vol. 530, pp. 144–147, Feb 2016.

[13] H. Jaeger, "Towards a generalized theory comprising digital, neuromorphic and unconventional computing," *Neuromorphic Computing and Engineering*, vol. 1, no. 1, p. 012002, 2021.

[14] M. Wuttig and N. Yamada, "Phase-change materials for rewriteable data storage," *Nature Materials*, vol. 6, no. 11, pp. 824–832, 2007.

[15] D. Kuzum, R. G. Jeyasingh, B. Lee, and H. S. Wong, "Nanoelectronic programmable synapses based on phase change materials for brain-inspired computing," *Nano Letters*, vol. 12, no. 5, pp. 2179–2186, 2012.

[16] L. O. Chua, "Memristor—The missing circuit element," *IEEE Transactions on Circuit Theory*, vol. 18, no. 5, pp. 507–519, 1971.

[17] T. Prodromakis, C. Toumazou, and L. Chua, "Two centuries of memristors," *Nature Materials*, vol. 11, pp. 478–481, jun 2012.

[18] R. Midya, Z. Wang, J. Zhang, S. E. Savel'ev, C. Li, M. Rao, M. H. Jang, S. Joshi, H. Jiang, P. Lin, K. Norris, N. Ge, Q. Wu, M. Barnell, Z. Li, H. L. Xin, R. S. Williams, Q. Xia, and J. J. Yang, "Anatomy of Ag/Hafnia-based selectors with 10^{10} nonlinearity," *Advanced Materials*, vol. 29, p. 1604457, Mar 2017.

[19] Z. Wang, M. Rao, R. Midya, S. Joshi, H. Jiang, P. Lin, W. Song, S. Asapu, Y. Zhuo, C. Li, H. Wu, Q. Xia, and J. J. Yang, "Threshold switching of Ag or Cu in dielectrics: Materials, mechanism, and applications," *Advanced Functional Materials*, vol. 28, no. 6, p. 1870036, 2018.

[20] D. Ielmini, "Resistive switching memories based on metal oxides: Mechanisms, reliability and scaling," *Semiconductor Science and Technology*, vol. 31, no. 6, p. 063002, 2016.

[21] J. J. Yang, D. B. Strukov, and D. R. Stewart, "Memristive devices for computing," *Nature Nanotechnology*, vol. 8, no. 1, pp. 13–24, 2013.

[22] W. Wang, M. Wang, E. Ambrosi, A. Bricalli, M. Laudato, Z. Sun, X. Chen, and D. Ielmini, "Surface diffusion-limited lifetime of silver and copper nanofilaments in resistive switching devices," *Nature Communications*, vol. 10, p. 81, 2019.

[23] J. Joshua Yang, F. Miao, M. D. Pickett, D. A. Ohlberg, D. R. Stewart, C. N. Lau, and R. S. Williams, "The mechanism of electroforming of metal oxide memristive switches," *Nanotechnology*, vol. 20, no. 21, p. 215201, 2009.

[24] C. Du, F. Cai, M. A. Zidan, W. Ma, S. H. Lee, and W. D. Lu, "Reservoir computing using dynamic memristors for temporal information processing," *Nature Communications*, vol. 8, p. 2204, 2017.

[25] S. K. Bose, S. Shirai, J. B. Mallinson, and S. A. Brown, "Synaptic dynamics in complex self-assembled nanoparticle networks," *Faraday Discussions*, vol. 213, pp. 471–485, 2019.

[26] C. Minnai, A. Bellacicca, S. A. Brown, and P. Milani, "Facile fabrication of complex networks of memristive devices," *Scientific Reports*, vol. 7, no. 1, p. 7955, 2017.

[27] A. Z. Stieg, A. V. Avizienis, H. O. Sillin, C. Martin-Olmos, M. Aono, and J. K. Gimzewski, "Emergent criticality in complex Turing B-type atomic switch networks," *Advanced Materials*, vol. 24, no. 2, pp. 286–293, 2012.

[28] M. Mirigliano, D. Decastri, A. Pullia, D. Dellasega, A. Casu, A. Falqui, and P. Milani, "Complex electrical spiking activity in resistive switching nanostructured Au two-terminal devices," *Nanotechnology*, vol. 31, no. 23, p. 234001, 2020.

[29] A. Sattar, S. Fostner, and S. A. Brown, "Quantized conductance and switching in percolating nanoparticle films," *Physical Review Letters*, vol. 111, no. 13, p. 136808, 2013.

[30] M. Mirigliano, F. Borghi, A. Podestà, A. Antidormi, L. Colombo, and P. Milani, "Non-ohmic behavior and resistive switching of Au cluster-assembled films beyond the percolation threshold," *Nanoscale Advances*, vol. 1, no. 8, pp. 3119–3130, 2019.

[31] S. K. Bose, J. B. Mallinson, R. M. Gazoni, and S. A. Brown, "Stable self-assembled atomic-switch networks for neuromorphic applications," *IEEE Transactions on Electron Devices*, vol. 64, no. 12, pp. 5194–5201, 2017.

[32] J. B. Mallinson, S. Shirai, S. K. Acharya, S. K. Bose, E. Galli, and S. A. Brown, "Avalanches and criticality in self-organized nanoscale networks," *Science Advances*, vol. 5, no. 11, p. eaaw8483, 2019.

[33] C. Minnai, M. Mirigliano, S. A. Brown, and P. Milani, "The nanocoherer: An electrically and mechanically resettable resistive switching device based on gold clusters assembled on paper," *Nano Futures*, vol. 2, no. 1, p. 1002, 2018.

[34] M. D. Pike, S. K. Bose, J. B. Mallinson, S. K. Acharya, S. Shirai, E. Galli, S. J. Weddell, P. J. Bones, M. D. Arnold, and S. A. Brown, "Atomic scale dynamics drive brain-like avalanches in percolating nanostructured networks," *Nano Letters*, vol. 20, no. 5, pp. 3935–3942, 2020.

[35] Y. Yang, B. Chen, and W. D. Lu, "Memristive physically evolving networks enabling the emulation of heterosynaptic plasticity," *Advanced Materials*, vol. 27, pp. 7720–7727, Dec 2015.

[36] T. H. Kim, X. G. Zhang, D. M. Nicholson, B. M. Evans, N. S. Kulkarni, B. Radhakrishnan, E. A. Kenik, and A. P. Li, "Large discrete resistance jump at grain boundary in copper nanowire," *Nano Letters*, vol. 10, no. 8, pp. 3096–3100, 2010.

[37] S. L. Johnson, A. Sundararajan, D. P. Hunley, and D. R. Strachan, "Memristive switching of single-component metallic nanowires," *Nanotechnology*, vol. 21, no. 12, p. 125204, 2010.

[38] T. B. Song, Y. Chen, C. H. Chung, Y. Yang, B. Bob, H. S. Duan, G. Li, K. N. Tu, and Y. Huang, "Nanoscale Joule heating and electromigration enhanced ripening of silver nanowire contacts," *ACS Nano*, vol. 8, no. 3, pp. 2804–2811, 2014.

[39] R. Hoffmann-Vogel, "Electromigration and the structure of metallic nanocontacts," *Applied Physics Reviews*, vol. 4, no. 3, p. 031302, 2017.

[40] A. Halbritter, S. Csonka, O. Y. Kolesnychenko, G. Mihály, O. I. Shklyarevskii, O. I. Shklyarevskii, and H. van Kempen, "Connective neck evolution and conductance steps in hot point contacts," *Physical Review B*, vol. 65, pp. 454131–454138, Jan 2002.

[41] Y. H. Wen, Y. Zhang, J. C. Zheng, Z. Z. Zhu, and S. G. Sun, "Orientation-dependent structural transition and melting of Au nanowires," *Journal of Physical Chemistry C*, vol. 113, no. 48, pp. 20611–20617, 2009.

[42] Y. H. Wen, Z. Z. Zhu, R. Zhu, and G. F. Shao, "Size effects on the melting of nickel nanowires: A molecular dynamics study," *Physica E: Low-Dimensional Systems and Nanostructures*, vol. 25, no. 1, pp. 47–54, 2004.

[43] A. Volk, D. Knez, P. Thaler, A. W. Hauser, W. Grogger, F. Hofer, and W. E. Ernst, "Thermal instabilities and Rayleigh breakup of ultrathin silver nanowires grown in helium nanodroplets," *Physical Chemistry Chemical Physics*, vol. 17, no. 38, pp. 24570–24575, 2015.

[44] P. Moskovkin, M. Panshenskov, S. Lucas, and A. V. Solov'yov, "Simulation of nanowire fragmentation by means of kinetic Monte Carlo approach: 2D case," *Physica Status Solidi (B) Basic Research*, vol. 251, no. 7, pp. 1456–1462, 2014.

[45] M. Schnedlitz, M. Lasserus, D. Knez, A. W. Hauser, F. Hofer, and W. E. Ernst, "Thermally induced breakup of metallic nanowires: Experiment and theory," *Physical Chemistry Chemical Physics*, vol. 19, no. 14, pp. 9402–9408, 2017.

[46] S. Koo, J. Park, S. Koo, and K. Kim, "Local heat dissipation of Ag nanowire networks examined with scanning thermal microscopy," *Journal of Physical Chemistry C*, vol. 125, no. 11, pp. 6306–6312, 2021.

[47] C. L. Kim, J. Y. Lee, D. G. Shin, J. S. Yeo, and D. E. Kim, "Mechanism of heat-induced fusion of silver nanowires," *Scientific Reports*, vol. 10, p. 9271, 2020.

[48] I. A. Solov'yov, A. V. Yakubovich, P. V. Nikolaev, I. Volkovets, and A. V. Solov'yov, "MesoBioNano explorer-A universal program for multiscale computer simulations of

complex molecular structure and dynamics," *Journal of Computational Chemistry*, vol. 33, no. 30, pp. 2412–2439, 2012.

[49] G. B. Sushko, I. A. Solov'yov, and A. V. Solov'yov, "Modeling MesoBioNano systems with MBN Studio made easy," *Journal of Molecular Graphics and Modelling*, vol. 88, pp. 247–260, 2019.

[50] P. N. Plessow, "The transformation of cuboctahedral to icosahedral nanoparticles: Atomic structure and dynamics," *Physical Chemistry Chemical Physics*, vol. 22, no. 23, pp. 12939–12945, 2020.

[51] D. M. Wells, G. Rossi, R. Ferrando, and R. E. Palmer, "Metastability of the atomic structures of size-selected gold nanoparticles," *Nanoscale*, vol. 7, no. 15, pp. 6498–6503, 2015.

[52] Y. Kondo and K. Takayanagi, "Gold nanobridge stabilized by surface structure," *Physical Review Letters*, vol. 79, no. 18, pp. 3455–3458, 1997.

[53] M. J. Lagos, F. Sato, P. A. Autreto, D. S. Galvao, V. Rodrigues, and D. Ugarte, "Temperature effects on the atomic arrangement and conductance of atomic-size gold nanowires generated by mechanical stretching," *Nanotechnology*, vol. 21, no. 48, p. 485702, 2010.

[54] A. Halder and N. Ravishankar, "Ultrafine single-crystalline gold nanowire arrays by oriented attachment," *Advanced Materials*, vol. 19, no. 14, pp. 1854–1858, 2007.

[55] R. P. Gupta, "Lattice relaxation at a metal surface," *Physical Review B*, vol. 23, no. 12, pp. 6265–6270, 1981.

[56] F. Cleri and V. Rosato, "Tight-binding potentials for transition metals and alloys," *Physical Review B*, vol. 48, pp. 22–33, Jul 1993.

[57] L. Landau and E. Lifshitz, *Statistical Physics*. Oxford: Pergamon Press, 1980.

[58] I. A. Solov'yov, A. V. Korol, and A. V. Solov'yov, *Multiscale Modeling of Complex Molecular Structure and Dynamics with MBN Explorer*. Cham: Springer International Publishing, 2017.

[59] A. Stukowski, "Structure identification methods for atomistic simulations of crystalline materials," *Modelling and Simulation in Materials Science and Engineering*, vol. 20, no. 4, p. 045021, 2012.

[60] A. Stukowski, "Visualization and analysis of atomistic simulation data with OVITO-the Open Visualization Tool," *Modelling and Simulation in Materials Science and Engineering*, vol. 18, no. 1, p. 015012, 2010.

[61] P. E. Marszalek, W. J. Greenleaf, H. Li, A. F. Oberhauser, and J. M. Fernandez, "Atomic force microscopy captures quantized plastic deformation in gold nanowires," *Proceedings of the National Academy of Sciences of the United States of America*, vol. 97, no. 12, pp. 6282–6286, 2000.

[62] F. A. Nichols and W. W. Mullins, "Morphological changes of a surface of revolution due to capillarity-induced surface diffusion," *Journal of Applied Physics*, vol. 36, no. 6, pp. 1826–1835, 1965.

Chapter 5 Nanofilament Formation Between Au Clusters on Graphite

The previous chapter considered the fission of an individual filament between two clusters, i.e. synapse rupture. This chapter considers the complementary process, the formation of such a connection. The supporting surface is introduced to explore the mechanism in this simulation of two gold clusters

In this chapter, I was involved in designing the simulations, building the model, carrying out simulations and performing the data analysis.

5.1 Introduction

As traditional von Neumann computing approaches its fundamental limits and requires increasing energy resources, neuromorphic computing has emerged as a promising interdisciplinary research area [1–4]. Inspired by the human brain's energy-efficiency and capabilities, neuromorphic computing aims to mimic brain function using artificial neurons [5]. One proposed architecture involves interconnected, synapse-like switching devices such as memristors, whose resistance changes based on the history of applied bias voltage [6–10]. Formation and breakage of nanoscale conductive filaments play a crucial role in switching behavior [11].

Random assembly of nanoscale building blocks, such as atomic clusters and small nanoparticles, is a promising approach for forming neuromorphic networks [12]. Metal cluster films fabricated using gas-phase deposition techniques exhibit non-ohmic switching behavior [13–18] and can be deposited on various insulating materials [12, 15–18]. Cluster deposition technologies offer a simpler and potentially cheaper alternative to lithography methods for creating robust intra- and inter-device connections [19–24].

The mechanisms of the formation and breakage of the conductive connections between clusters have been widely discussed in the literature. According to experimental observations like conductance measurements [14, 25], the electric field-induced surface diffusion and evaporation and the van der Waals interaction between metal atoms are con-

sidered the main mechanisms of the formation of atomic-scale connections between the clusters [26–28]. Experimental observations obtained using scanning transmission electron microscopy and simulation results obtained using the kinetic Monte Carlo method showed that the width of the connection increases with time as a power-law function [29,30]. The value of the power can be explained by the combined contributions from surface diffusion and viscosity flow [31,32]. On the other hand, the breakage of the connections is explained by electromigration caused by the electric current running through the connections. Numerous studies have emphasised the contribution of electromigration to the breakage or resistive switching of metal nanowires (NWs) [33–36]. An alternative mechanism for the breakage is the Joule heating induced by the current running through the connections [13]. High temperatures of up to thousands of kelvins could be induced by small voltage drops on the order of $\sim$100 mV when the size of a point contact in a complex nanoscale junction is smaller than the mean free path of electrons [37]. The thermally induced breaking of NWs has been frequently reported [38–40], and relevant computer simulations have been carried out [41–43]. Strong local heating can be observed in an NW network when the current exists [44]. The breaking process of the NW caused by heat generation can be observed in situ using transmission electron microscopy [45].

Although there are plenty of experimental studies and computer simulations of cluster dynamics on various substrates [46–48], the role of the substrate in the formation and breakage of conductive filaments remains unclear. Multiple quantum conductance models and related experiments and simulations have been employed to evaluate the current running through a filament and its conductance [49–53]. However, to date, there have been no studies considering the whole process of nanofilament formation and breakage, from applying the bias voltage to the breakage of a nanofilament due to generated heat.

In this chapter, the formation and breaking of a nanoscale conductive filament between nanometre-sized gold clusters placed on a carbon substrate are studied using molecular dynamics (MD) simulations. The characteristic times for bridge formation are evaluated at elevated temperatures ($T = 500$–800 K) for different cluster orientations and distances between the neighbouring clusters, and they are used to estimate the bridge formation time at experimentally relevant conditions. The heat generated by the electric current
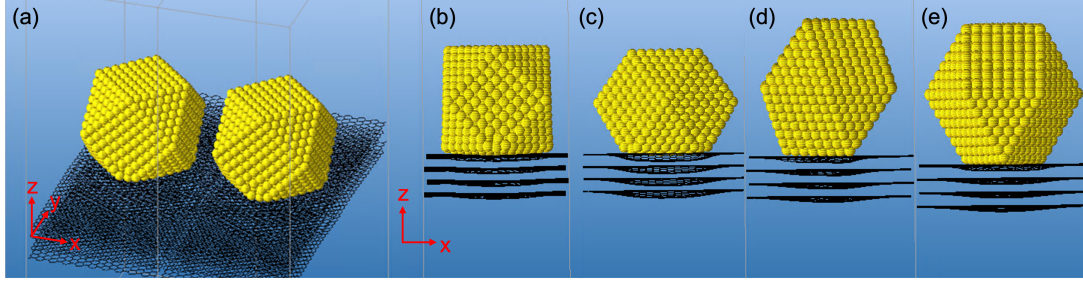
Figure 5-1 The geometry of the simulated system. A cuboctahedral Au_{1415} cluster is placed on top of a four-layer thick graphite substrate and periodic boundary conditions are employed. (a) Snapshot of the system and its periodic image. (b) a (100) facet of the gold cluster is set perpendicular to x direction ('Au(100)'). (c) based on Au(100), rotate the cluster for 45° along z axis ('Au(100)rot'). (d) a (111) facet of the cluster is set perpendicular to z direction and one edge of the (111) facet triangle is parallel to the y axis ('Au(111)'). (e) based on Au(111), rotate the cluster for 60°along z axis. the (111) facet of the cluster is set perpendicular to z direction and one edge of the (111) facet triangle is parallel to the x axis (Au(111)rot). the substrate is bent as a result of the energy minimization during the initial geometry optimization.

for different bias voltage values is estimated using a model approach for determining the conductance of nanoscopic systems, and the nanofilament breaking process under these thermal conditions has been simulated. The presented results provide an atomistic-level understanding of the fundamental processes involving the conductive connections between deposited metal clusters. Our results highlight the important role of the substrate in the bridge formation and breakage processes, and they offer new insights into the fundamental processes in cluster-based neuromorphic computing systems.

5.2 Methodology

The MD simulations were performed with the MBN Explorer software package [54]. The creation of the systems and the analysis of the results were performed with its accompanying multitask toolkit, MBN Studio [55].

The studied system comprises a cuboctahedral Au_{1415} cluster placed on top of a four-layer-thick graphite substrate. In neuromorphic devices fabricated by deposition techniques, clusters exhibit diverse sizes and structures. [13–18] The selection of cuboctahedral Au_{1415} with various orientations exemplifies the inherent complexity of such systems while preserving a relatively simple arrangement. Although insulating materials are typically used as substrates in neuromorphic devices, graphite is commonly employed as a substrate in STEM observations. We opted for a graphite substrate to maintain system simplicity and facilitate comparisons with in situ STEM observations [30], ensuring a more direct connection to experimental results. The system is simulated using periodic boundary conditions so that the connecting bridges are formed between the cluster and its neighbouring periodic images. Four different Au_{1415} geometry arrangements have been simulated: (i) a (100) facet of the gold cluster was perpendicular to x direction (labeled as 'Au(100)'); (ii) rotate the cluster for 45° along z axis based on (i) ('Au(100)rot'); (iii) a (111) facet of the cluster was perpendicular to z direction, while one edge of the (111) facet triangle was parallel to the y axis ('Au(111)'); and (iv) rotate the cluster for 60°along z axis based on (iii), so that the (111) facet of the cluster was perpendicular to z direction, while one edge of the (111) facet triangle was parallel to the x-axis ('Au(111)rot'). These geometrical arrangements are shown in Figure 5-1. The distance between the cluster and its periodic image is determined by the minimum distance of all the distances between any atom from the cluster and any atom from its periodic image, which describe the width of the 'gap' between the clusters. The distance has been varied by adjusting the size of the simulation box. The bottom-most layer of the substrate has been fixed to avoid the translational motion of the whole system.

The many-body Gupta potential [56, 57] was used to model the interaction between gold atoms. The bond-order Brenner potential [58] was used to describe the interaction between covalently bonded carbon atoms within each graphite layer, whereas the Lennard-Jones potential was employed to account for the van der Waals interaction between the graphite layers and Au-C interactions. The parameters for these interatomic potentials are listed in a previous study [47], as they have been demonstrated to provide reliable and accurate results for systems with a similar nature to our research, making them suitable

for the current work. An introduction of these potentials can be found in Chapter 3.

In the bridge formation simulation, the Langevin thermostat is used to control the temperature and represent the ambient environment as described in Chapter 3. 1 ps damping time was used to control the temperature, providing the system with enough time to equilibrate while maintaining a balance between computational efficiency and adequate sampling. The timestep for the MD was set to 2 fs. After the energy minimisation process, MD simulations were carried out at a constant temperature for 10 ns. This time scale is chosen to balance between ensuring sufficient time for the system to exhibit meaningful structural and dynamic changes, and maintaining computational feasibility. For each geometry and distance between the cluster and its images, different thermostat temperatures within the range from 500 to 800 K were considered. The reason for choosing this temperature range, rather than room temperature, is to accelerate the structural changes in our system. By raising the temperature, we are able to observe significant behaviors and dynamics in a limited timescale, rendering the simulation more efficient and offering valuable insights under various conditions. It is important to note that room temperature is typically the temperature at which the neuromorphic devices worked. Therefore, by analyzing the high-temperature results, we can subsequently infer the room temperature behavior, facilitating an understanding of the system's performance under more realistic conditions.

In neuromorphic devices based on clusters with an applied bias, the generated Joule heat from the current flow through the bridge can result in the breaking of the bridge, as demonstrated in the previous chapter. The Joule heat generated from the current after the formation of the bridge can be evaluated, which enables the simulation of the bridge breakage process. In the bridge breakage simulation, the system's initial geometry was taken from the outcome of the bridge formation simulation. The simulations were carried out for 100 ps at 300 K, and the Langevin thermostat was used to equilibrate the system. The gold atoms that appeared in the gap between the neighbouring clusters in the initial Au(100) geometry (Figure 5-1 (a)) have been assigned to the bridge region. Of the various models used to estimate the conductance of the bridge and the current passing through the system at a given bias voltage, we use Wexler's model [50], which is the most relevant

to our simulation conditions and has been experimentally validated [53]. The details of the evaluation of the current and Joule heat can be found in the following result section. The heating rate for the system due to the Joule heating mechanism was evaluated according to the estimated current and conductance. Then, the velocities of gold atoms in the bridge region were rescaled according to the evaluated heating rate. The system then evolved over 2 ps without a thermostat, and the last frame of the simulation was used to re-evaluate the conductance and current for the chosen bias voltage. Multiple subsequent simulations were performed in this way for a total simulation time of 100 ps. The simulations were carried out for bias voltages from 10–100 mV that were applied between the cluster and its neighbouring image, which corresponds to the typical cluster sizes and distances between the electrodes in experiments [14, 29]. Although the realistic arrangement of clusters in a randomly assembled cluster film is more complex than the presented model, the chosen cluster geometries, as well as the temperature and bias voltage ranges, are representative for experiments in this research field. This permits us to explore at the atomistic scale the mechanisms that drive the functioning of such a device.

5.3   Results and discussions

5.3.1   Bridge formation process

The process of bridge formation between two gold Au_{1415} clusters deposited on a carbon substrate is illustrated in Figure 5-2. The process starts with the diffusion of surface gold atoms along the substrate, leading to the narrowing of the gap between the clusters. Then, a thin bridge with the width of one or two atoms is formed so that the clusters become connected. Figure 5-2 (a) shows a schematic illustration of this process, and Figure 5-2 (d) shows the corresponding MD simulation snapshot. The bridge then expands in width to about half of the cluster's diameter within the first 100–200 ps. The thickness of such a bridge corresponds to one monolayer of gold atoms. The corresponding schematic image and simulation snapshot are shown in Figure 5-2 (b) and Figure 5-2 (e), respectively. The increase in the width then becomes slower, and the second layer of atoms appears on the bridge. The steady-state structure of the system is shown in Figure 5-2 (c) and
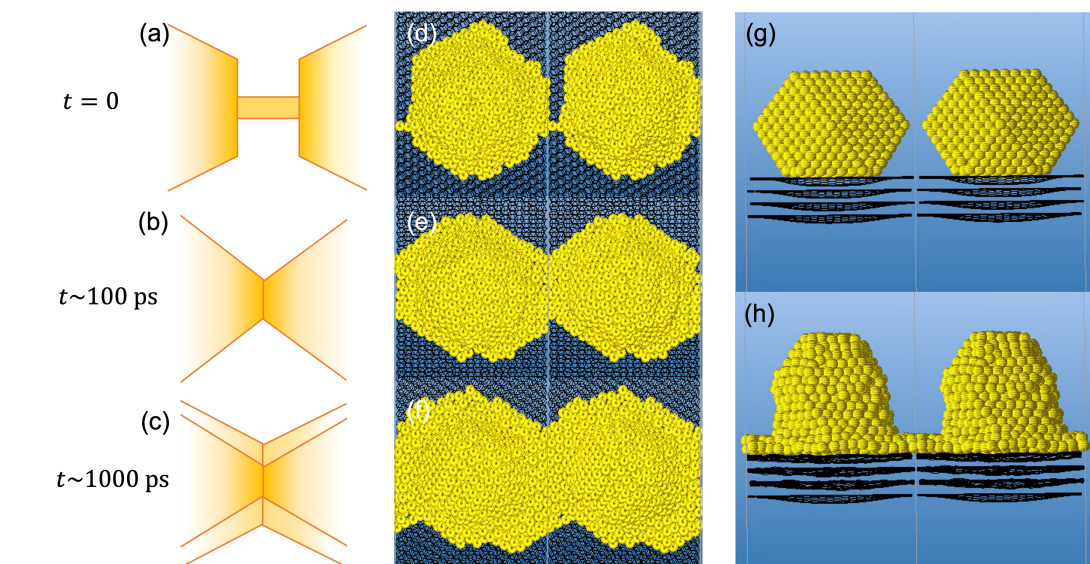
Figure 5-2 A typical bridge formation process. (a, b, c) Sketch of the bridge formation process. (a) A bridge with a width of one or two atoms is formed between two neighbouring Au_{1415} clusters. (b) The bridge then increases in width over the $\sim$100 ps of the simulation time. (c) The expansion becomes slower and the second layer of atoms is formed. (d, e, f) Corresponding bird's-eye view of the simulated MD trajectories. (g, h) The side view of a simulation result for the Au(100)rot geometry arrangement: (g) the initial configuration and (h) a steady state after the bridge has been formed. Bridge formation always takes place along the substrate and not at the initial narrowest distance between the clusters.

Figure 5-2 (f). It is noticeable that in the simulations carried out in this study, the bridge is always formed along the substrate for any initial distance between the clusters above 5 Å and for any cluster orientation. Figure 5-2 (g) shows the initial Au(100)rot geometry arrangement, where the smallest distance between atoms of two neighbouring clusters is set to 7 Å, a value smaller than the chosen cutoff distance for Au-Au interactions. Despite this closer distance, the atoms still diffuse along the substrate and form a bridge over the substrate, as shown in Figure 5-2 (h).

Due to the limited computational resources, the time scale of the bridge formation is too large to be observed in MD simulations at room temperature. Higher temperatures
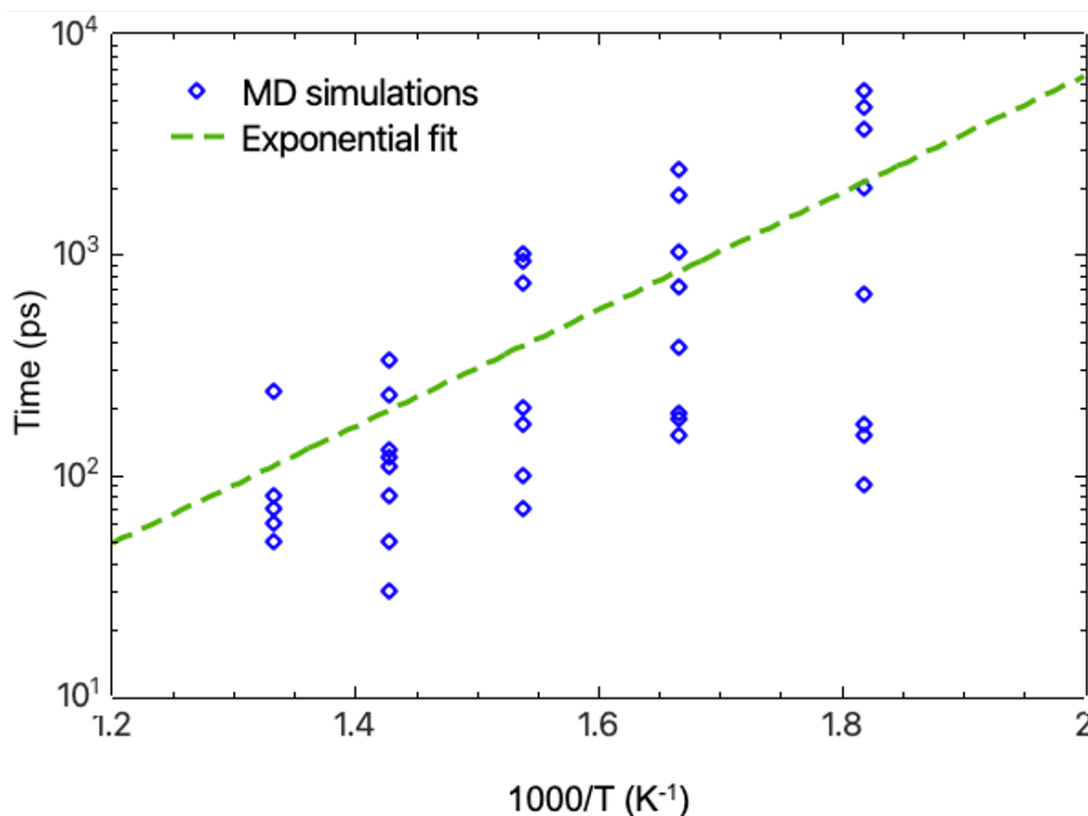
Figure 5-3 Bridge formation time as a function of thermostat temperature for the (100) orientation and 8 Å shortest distance between the neighbouring clusters. The diamond symbols are the individual simulations, and the green dashed line is the exponential fit.

in the range from 500–800 K have been considered, and a relation between the bridge formation time (from the beginning of the simulation to the appearance of the bridge shown in Figure 5-2 (a)) and thermostat temperature has been established. Figure 5-3 shows the dependence of the bridge formation time on the inverse temperature ($1/T$). The figure shows the simulation results for temperatures above 550 K at which the bridge has been formed in every simulation run. Dots indicate the results of each run, and crosses illustrate the average bridge formation time for a specific temperature. The formation time is shown on a logarithmic scale. The averaged formation time has been fitted with an exponential function of $1/T$ ($R^2 = 0.99$). According to this relation and data variation, the estimated formation time at $T = 300$ K is $10^7 \sim 10^8$ ps.

According to surface diffusion theory, the single particle on the surface will diffuse with the following rate:

$$\Gamma = \frac{1}{\Delta t} = \nu \exp\left(-\frac{E_a}{k_B T}\right),$$ (5-1)

where E_a is the activation energy, ν is the attempt escape rate, T is the temperature of the system, k_B is the Boltzmann constant and Δt is the simulation time step, which defines the characteristic time for particle diffusion on the surface [59–61]. It can be seen that Δt has an exponential relationship with $1/T$. Since the bridge formation process can be seen as the accumulated diffusive steps of each atom and similar geometry states are reached in simulations at different temperatures when the bridge is formed, it is reasonable to consider the bridge formation time to have an exponential relationship with $1/T$, as shown in Figure 5-3, and to consider the surface diffusion to be the dominant mechanism of the bridge-forming process in our model.

Different distances between neighbouring clusters have also been considered, and the bridge formation time for each inter-cluster distance at $T = 750$ K is shown in Figure 5-3 (b). Both the formation time and distance are on a logarithmic scale. A power-law relation is fitted between the formation time and the distance ($R^2 = 0.98$). The distance (d) and time (t) have the following relationship: $t \sim d^{5.9}$ which will be discussed in the following paragraph.

In the bridge-forming process shown in Figures 5-2 (a) and (d), the bridge can only form after the clusters have diffused along the substrate and the gap width has been reduced to a certain level. The formation time-distance relationship is almost equivalent to the relationship between the average atomic diffused displacement and the time. The mean-square displacement of a single diffusive atom on the surface has the following relationship with time: $\langle \Delta x^2 \rangle = 2\Gamma l^2 t$ [61], where l is the mean displacement in a single time step, Δx is the displacement distance, and Γ is the diffusion constant. However, this quadratic function relation does not fit well (R^2 lower than 0.8) with the simulation results in Figure 5-4. This mismatch is reasonable because atomic diffusion from part of the cluster on the substrate will not be equivalent to a free atom on the surface due to viscosity and geometry factors. The liquid drop model has been frequently used to study
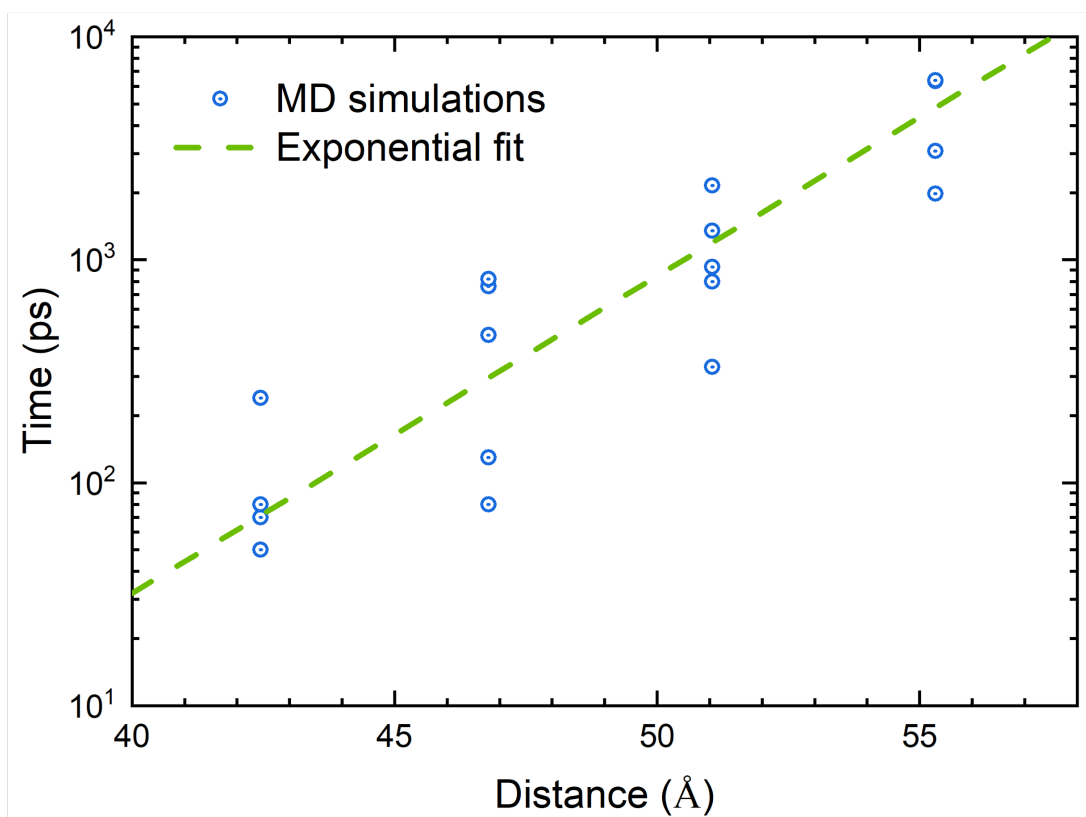
Figure 5-4 Bridge formation time as a function of distance between the neighbouring clusters at $T = 750$ K. The center-dotted circles are the individual simulations, and the green dashed line is the exponential fit.

the behaviour of the cluster, especially in the high-temperature conditions studied by many researchers [62,63]. Experimental and theoretical studies of the diffusive spreading of a liquid drop on the surface have been reported [64,65]. The droplet radius on the surface has a multiple-stage and complex relationship with time. Although it is hard to express the relationship explicitly, part of the spreading process (for example, Figure 5 in [64]) fits well with the power law. In certain stages of the droplet spreading in [64], the relation between the radius and time ranges from $t \sim R^7$ to $t \sim R^{10}$. Our result fits the power law well, and the power is close to that of the liquid drop power law ($t \sim d^{5.9}$). The deviation exists because the cluster has a different viscosity and is not exactly the same as the liquid. Further research is needed to look into the exact mechanism and relationship.

The 'formation time-inverse temperature' relation has also been explored for different geometry orientations, as shown in Figure 5-5, and the exponential function has been used to fit the MD simulation results for each orientation. The distance between neighbouring clusters has been set to 7 Å for all configurations. The predicted formation time at 300 K is ~ 10 μs for Au(100), ~ 10 s for Au(100)rot and over one year for Au(111) and Au(111)rot. The formation process is significantly faster for the Au(100) orientation because this orientation has the smallest distance to diffuse along the substrate due to the geometry feature shown in Figure 5-1. The timescale of Au(111) and Au(111)rot are too large to be observed because the (111) surface of gold can match the graphite structure very well, which stabilises the cluster compared to (100) and (100)rot, which mismatch with the substrate. The predicted formation time at 300 K has a large variation from ~ 10 μs to multiple years, which reflects the experimental complexity of the switching behaviour in randomly assembled cluster films [14,18].

After bridge formation, the neck width of the bridge will continue growing. The 'neck width-time' relation for the Au(100) orientation at different temperatures is shown in Figure 5-6. Multiple simulations have been carried out at each temperature, and each dot shows the average time at which the bridge reaches a certain width. The data fit well with the power law $D \sim t^{\alpha}$, where D is the neck width of the bridge, t is time and α is the power number [29,30]. The relation between the power α and the temperature is shown in the inset. It can be seen that $\alpha \sim 0.33$, and it is independent of the temperature.

102
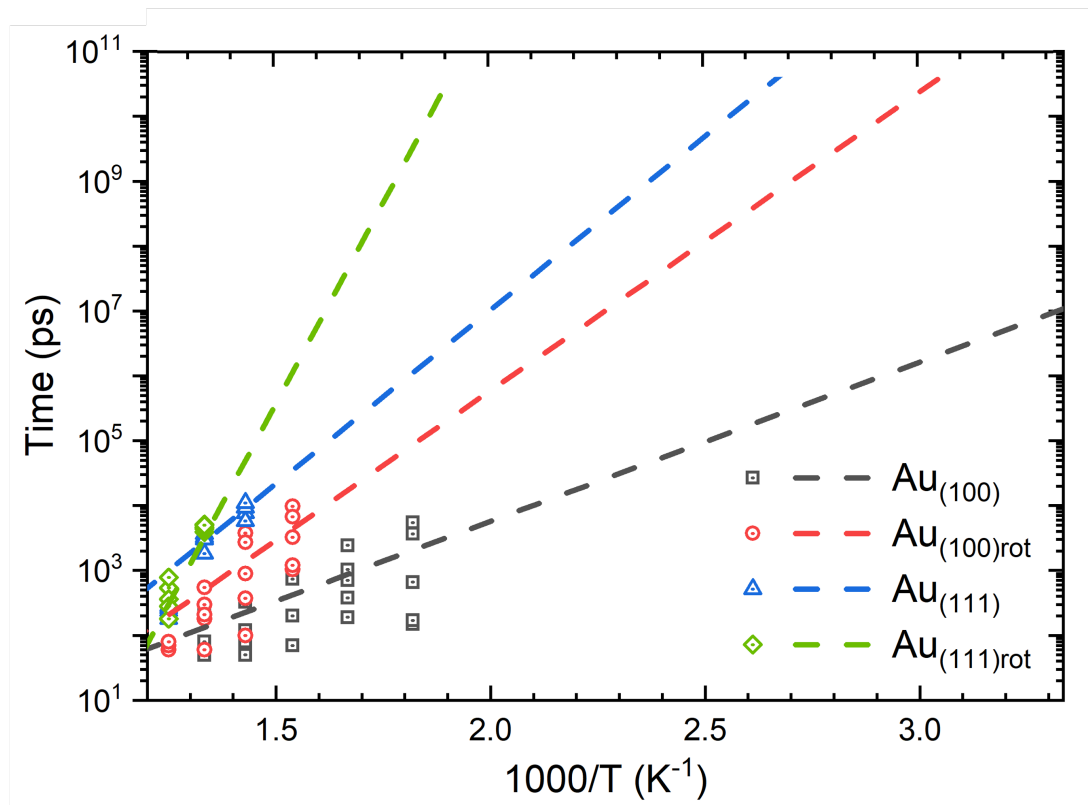
Figure 5-5 The 'formation time-inverse temperature' dependence for different geometry orientations. Symbols show the results of individual MD runs; and dashed lines illustrate the exponential fit.
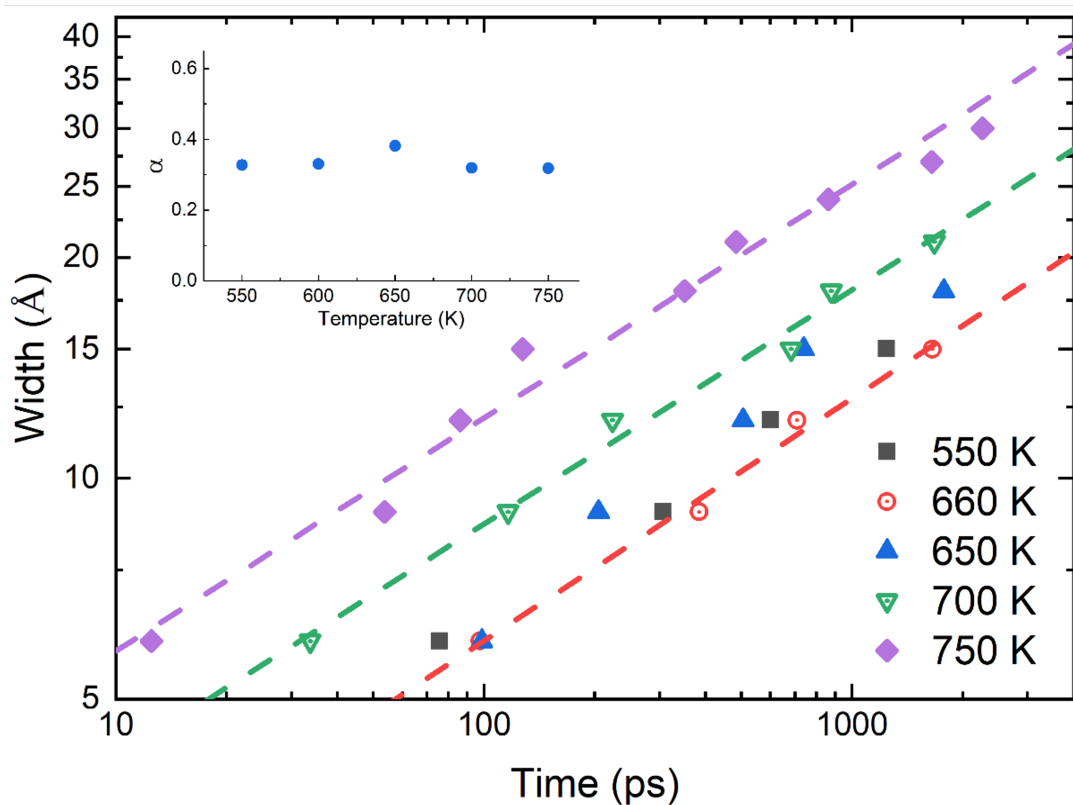
Figure 5-6 Width-time relation of the bridge for different temperatures. Each symbol shows the average time at which the bridge reaches a certain width. The power law $D \sim t^{\alpha}$ is fitted by the dashed line, where α is the power number. The inset shows the relation between α and the temperature.
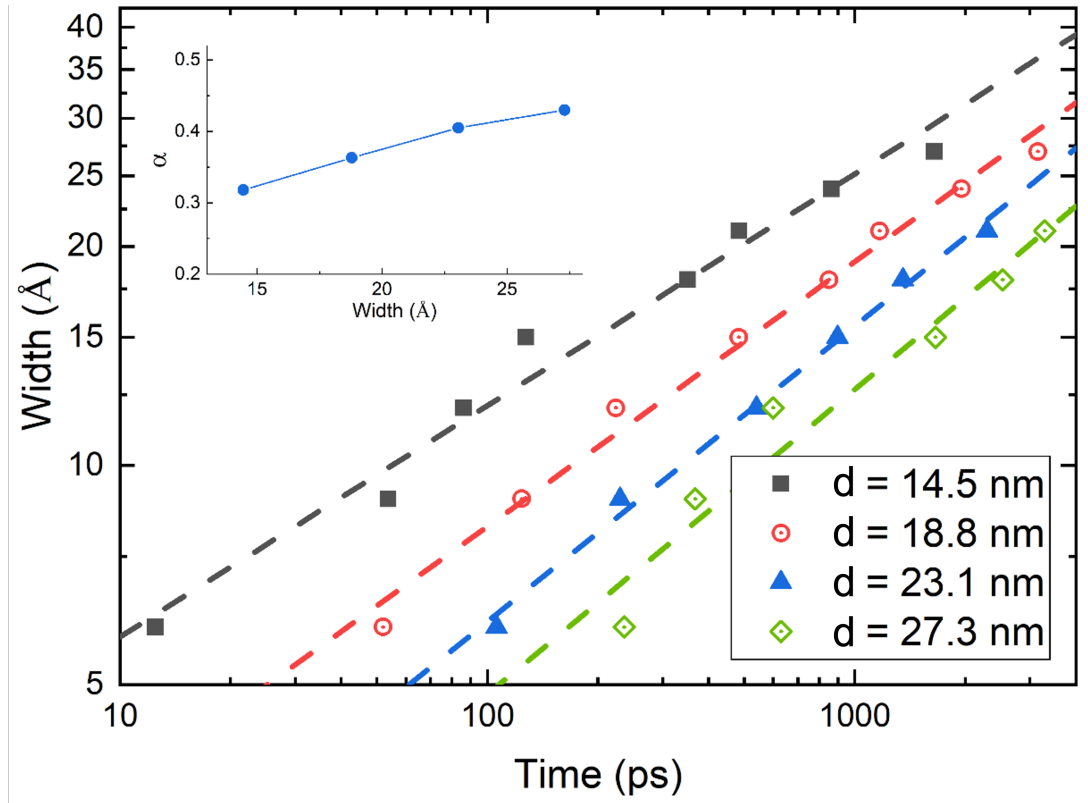
Figure 5-7 Width-time relation of the bridge for different distances d. Each symbol shows the average time at which the bridge reaches a certain width. The power law $D \sim t^\alpha$ is fitted by the dashed line, where α is the power number. The inset shows the relation between α and the distance.

A similar analysis has also been done for different distances between the neighbouring clusters. Figure 5-7 shows the neck width-time relation for different neighbouring distances at 750 K. The power law $D \sim t^\alpha$ relation is also used to fit the data, and the relationship between the power α and the distance is shown in the inset. A constant increase in α can be seen, along with an increase in the distance. The range of the power α lies between 0.31 and 0.45.

The neck-width growing process has been experimentally observed and Monte Carlo simulations have been performed to study the mechanism [29, 30]. It was shown that the neck radius r between two coalescing microscale solid particles follows a power law $r \propto t^\alpha$, where α is specific to the physical coalescence process and lies between 1/6 (surface diffusion) [31] and 1/2 (viscous flow) [32]. Our result, shown in Figure 5-6, fits well with

the power law and the power $\alpha \sim 0.31$, which is in the range of the theoretical prediction and highly similar to the in situ observation result in [30]. Our simulation at different temperatures shows that the power number α is independent of the temperature, which is also compatible with the theoretical prediction. The clusters have spherical shapes in most previous Monte Carlo simulations, and no substrates are considered [29, 66], so the cross section of the neck is circular. In our result, however, the neck has a bow-tie shape with a thickness of one or two layers of atoms (shown in Figure 5-2 (e), (f), (h)). It can be seen that despite the geometry difference caused by the surface interaction between the gold and the substrate, the neck growth mechanism remains unchanged. On the other hand, our result in Figure 5-7 shows that the power number α can be affected by the initial distance between the clusters, but the value of α is still within the range of $1/6 \sim 1/2$. A longer initial distance will make the diffused cluster deviate more from the circular shape when the bridge is formed. The α value approaches $1/2$ with a longer initial distance, which shows that the viscosity flow mechanism dominates when the geometry of the system deviates from the ideal circular shape.

5.3.2 Bridge-breaking process

The bridge-breaking process has been studied under different values of the bias voltage, varied from 10 to 100 mV, at $T = 300$ K. The geometry of the bridge with a width of one or two atoms was chosen to be the initial state because the current flow will pass through the bridge immediately when the bridge is formed, as described in previous experimental works [13–18]. The conductance of the bridge is evaluated using the Wexler's theory model [50]:

$$G_{Wexler} = \frac{k_F{}^2}{4\pi} S G_0 \left[1 + \frac{3\pi}{8} \Gamma\left(K\right) \frac{r}{l} \right]^{-1} \tag{5-2}$$

where k_F is the Fermi wavevector (in our case, gold, $k_F = 1.204$ Å^{-1} [67]), $G_0 = 2e^2/h$ is the quantum conductance unit, r is radius of the cross section of the bridge (in our case for one atom bridge, is the radius of gold atom 1.44Å), l is the electron mean free path, S is the area of the cross section of the bridge (in our case $S = \pi r^2$), $\Gamma(K)$ is a slowly varying function of order ~ 1 which can be seen as constant in our case, and $K = l/r$

Table 5-1 Characteristic parameters of the bridge.

conductance/G_0	bias/mV	current/μA	power/nW
0.72	46	2.6	120
	30	1.7	50

is the so-called Knudsen number (the ratio of mean free path and the representative physical length scale, in our case, radius of the cross section of the bridge). Experimental results show a "conductance – surface area" relation between the gold link formed by mechanical stretch [53]. The data was fitted well with the Wexler's expression. The fitted values $\Gamma(K) = 0.70$ and $l = 38$ Å. The conductance of the bridge was calculated with the information above and then the current and power under different bias can be evaluated as well.

For a larger bias like 46 mV, gold atoms in the bridge region will experience intense thermally induced atomic motion and eventually break the bridge at 25 ps. Local heat is generated due to different heat transfer properties between the cluster and the substrate. The temperature of the cluster reaches $\sim$ 700 K when the breakage happens. For a smaller bias like 30 mV, the atomic movement in the bridge part is not intense enough to break the bridge. The temperature of the cluster will keep increasing, and the width of the bridge will expand, as in the bridge-forming process. Figure 5-8 shows the different results for the different biases. The other biases between 30 and 46 mV cannot show a constant breaking or expanding result. The estimated conductance, current and power are shown in Table 5-1. The conductance is given in quantum conductance units ($G_0 = 2e^2/h$).

The geometry of the bridge with a width of one or two atoms is chosen to be the initial state because the current flow will pass through the bridge immediately when the bridge is formed in experimental conditions [13–18]. In our results, the bridge can be constantly broken or continue growing only when the bias is over 46 mV or under 30 mV, respectively. Biases between these two values will result in random growth or breakage behaviour. Our results indicate that a certain bias level is needed to break the bridge, but the threshold is obscure. Several experimental results mentioned the existence of this
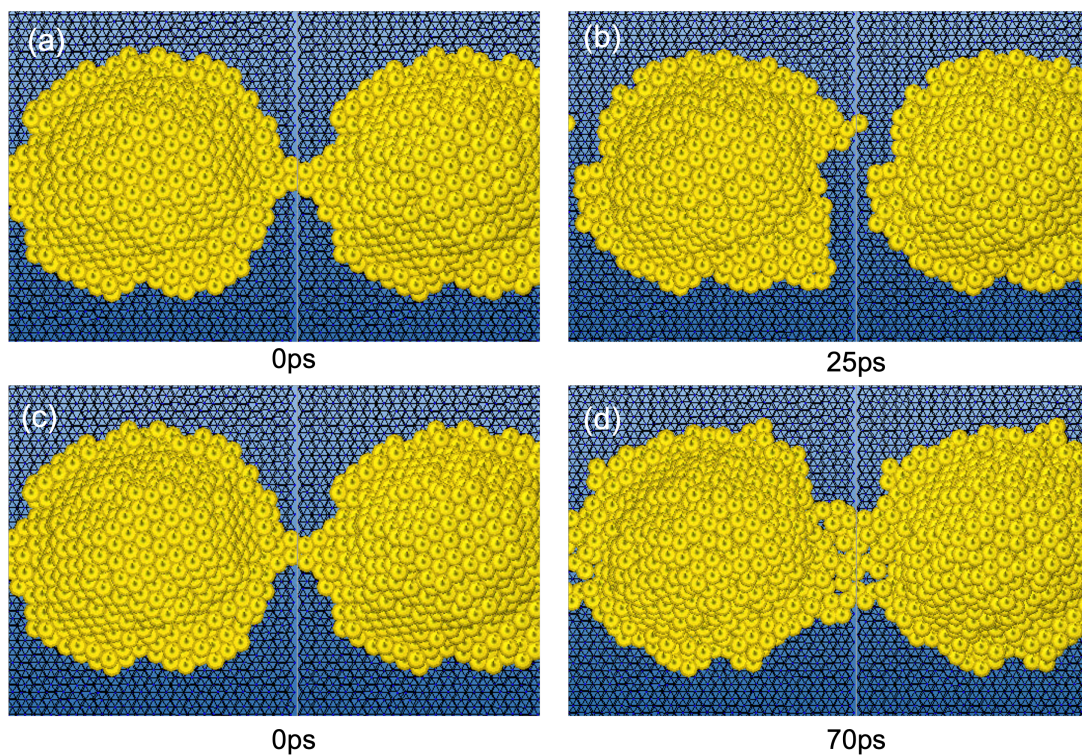
Figure 5-8 Breaking process results for different applied biases. (a), (b) The initial and breaking frames of a simulation with a 46 mV applied bias. (c), (d) The initial and in-between frames of a simulation with a 30 mV applied bias. The times of the corresponding frames are marked below the panels.

threshold [13, 14], and the complexity of the switching behaviour near this threshold is reported by conductance measurements [14–16]. Our simulation results can reflect these features properly and act as a good reference for future studies.

5.4 Conclusions

In summary, with the aim of providing an understanding of the formation and breakage of the conductive filamentary bridges between neighbouring clusters in neuromorphic devices, we built a series of model systems and performed MD simulations of the formation and breakage processes of the bridges by setting clusters on a graphite substrate.

In the bridge-forming simulations, high temperature was used to accelerate the whole process and make results visible within the limited MD simulation time. The time scale at room temperature was estimated from the relation found using the results for a series of higher temperatures. The diffusion on the graphite substrate contributes most of the formation mechanism in our simulations. The liquid droplet model can describe the spreading process of the cluster on graphite, and the neck width of the bridge after its formation can be described by the combined contributions of diffusion and viscosity flow.

In the bridge-breaking simulations, the conductance of the bridge was estimated using the quantum conductance model, and the Joule heat under particular biases was calculated. The temperature variation was applied by re-scaling the speed of the atoms on the bridge, and the breaking process was revealed by the simulation. Our result indicates that the Joule heating mechanism is an important part of the breaking process of the bridge. It also shows the existence of the bias threshold that must be reached to activate switching behaviour and demonstrates the complexity of the switching process in experiments.

In this chapter, atomistic simulations were performed to provide insight into the mechanisms of cluster-based neuromorphic systems. The substrate is considered, making our model more realistic. New mechanisms like diffusion and the formation and breakage processes on substrates are revealed by our model. The settings and parameters are chosen according to the experimental conditions, making our result representative and a good reference for further studies. However, more complicated and asymmetric situations can be found in a real cluster network, and more research is needed to present a full picture

of the mechanisms involved in the forming and breaking behaviour. This chapter's work can provide valuable insights and contribute to a better understanding of cluster-based neuromorphic devices.

References

[1] M. M. Waldrop, "The chips are down for Moore's law," *Nature*, vol. 530, pp. 144–147, Feb 2016.

[2] UN, "A new circular vision for electronics time for a global reboot." World Economic Forum, 2019, URL: https://www.weforum.org/reports/a-new-circular-vision-for-electronics-time-for-a-global-reboot.

[3] R. A. Nawrocki, R. M. Voyles, and S. E. Shaheen, "A mini review of neuromorphic architectures and implementations," *IEEE Transactions on Electron Devices*, vol. 63, pp. 3819–3829, Oct 2016.

[4] H. Jaeger, "Towards a generalized theory comprising digital, neuromorphic and unconventional computing," *Neuromorphic Computing and Engineering*, vol. 1, no. 1, p. 012002, 2021.

[5] C. Mead, "Neuromorphic electronic systems," *Proceedings of the IEEE*, vol. 78, no. 10, pp. 1629–1636, 1990.

[6] A. V. Avizienis, H. O. Sillin, C. Martin-Olmos, H. H. Shieh, M. Aono, A. Z. Stieg, and J. K. Gimzewski, "Neuromorphic atomic switch networks," *PLoS ONE*, vol. 7, no. 8, p. e42772, 2012.

[7] T. Ohno, T. Hasegawa, T. Tsuruoka, K. Terabe, J. K. Gimzewski, and M. Aono, "Short-term plasticity and long-term potentiation mimicked in single inorganic synapses," *Nature Materials*, vol. 10, pp. 591–595, Aug 2011.

[8] A. Z. Stieg, A. V. Avizienis, H. O. Sillin, C. Martin-Olmos, M. Aono, and J. K. Gimzewski, "Emergent criticality in complex Turing B-type atomic switch networks," *Advanced Materials*, vol. 24, no. 2, pp. 286–293, 2012.

[9] M. Wuttig and N. Yamada, "Phase-change materials for rewriteable data storage," *Nature Materials*, vol. 6, no. 11, pp. 824–832, 2007.

[10] L. O. Chua, "Memristor—The missing circuit element," *IEEE Transactions on Circuit Theory*, vol. 18, no. 5, pp. 507–519, 1971.

[11] T. Prodromakis, C. Toumazou, and L. Chua, "Two centuries of memristors," *Nature Materials*, vol. 11, pp. 478–481, jun 2012.

[12] C. Minnai, A. Bellacicca, S. A. Brown, and P. Milani, "Facile fabrication of complex networks of memristive devices," *Scientific Reports*, vol. 7, no. 1, p. 7955, 2017.

[13] M. Mirigliano, D. Decastri, A. Pullia, D. Dellasega, A. Casu, A. Falqui, and P. Milani, "Complex electrical spiking activity in resistive switching nanostructured Au two-terminal devices," *Nanotechnology*, vol. 31, no. 23, p. 234001, 2020.

[14] A. Sattar, S. Fostner, and S. A. Brown, "Quantized conductance and switching in percolating nanoparticle films," *Physical Review Letters*, vol. 111, no. 13, p. 136808, 2013.

[15] M. Mirigliano, F. Borghi, A. Podestà, A. Antidormi, L. Colombo, and P. Milani, "Non-ohmic behavior and resistive switching of Au cluster-assembled films beyond the percolation threshold," *Nanoscale Advances*, vol. 1, no. 8, pp. 3119–3130, 2019.

[16] S. K. Bose, J. B. Mallinson, R. M. Gazoni, and S. A. Brown, "Stable self-assembled atomic-switch networks for neuromorphic applications," *IEEE Transactions on Electron Devices*, vol. 64, no. 12, pp. 5194–5201, 2017.

[17] J. B. Mallinson, S. Shirai, S. K. Acharya, S. K. Bose, E. Galli, and S. A. Brown, "Avalanches and criticality in self-organized nanoscale networks," *Science Advances*, vol. 5, no. 11, p. eaaw8483, 2019.

111

[18] C. Minnai, M. Mirigliano, S. A. Brown, and P. Milani, "The nanocoherer: An electrically and mechanically resettable resistive switching device based on gold clusters assembled on paper," *Nano Futures*, vol. 2, no. 1, p. 1002, 2018.

[19] K. Wegner, P. Piseri, H. V. Tafreshi, and P. Milani, "Cluster beam deposition: A tool for nanoscale science and technology," *Journal of Physics D: Applied Physics*, vol. 39, no. 22, pp. 439–460, 2006.

[20] C. Zhang, H. Tsunoyama, H. Akatsuka, H. Sekiya, T. Nagase, and A. Nakajima, "Advanced nanocluster ion source based on high-power impulse magnetron sputtering and time-resolved measurements of nanocluster formation," *Journal of Physical Chemistry A*, vol. 117, no. 40, pp. 10211–10217, 2013.

[21] R. E. Palmer, L. Cao, and F. Yin, "Note: Proof of principle of a new type of cluster beam source with potential for scale-up," *Review of Scientific Instruments*, vol. 87, no. 4, pp. 10–13, 2016.

[22] J. Joshua Yang, F. Miao, M. D. Pickett, D. A. Ohlberg, D. R. Stewart, C. N. Lau, and R. S. Williams, "The mechanism of electroforming of metal oxide memristive switches," *Nanotechnology*, vol. 20, no. 21, p. 215201, 2009.

[23] C. Du, F. Cai, M. A. Zidan, W. Ma, S. H. Lee, and W. D. Lu, "Reservoir computing using dynamic memristors for temporal information processing," *Nature Communications*, vol. 8, p. 2204, 2017.

[24] S. K. Bose, S. Shirai, J. B. Mallinson, and S. A. Brown, "Synaptic dynamics in complex self-assembled nanoparticle networks," *Faraday Discussions*, vol. 213, pp. 471–485, 2019.

[25] M. D. Pike, S. K. Bose, J. B. Mallinson, S. K. Acharya, S. Shirai, E. Galli, S. J. Weddell, P. J. Bones, M. D. Arnold, and S. A. Brown, "Atomic scale dynamics drive brain-like avalanches in percolating nanostructured networks," *Nano Letters*, vol. 20, no. 5, pp. 3935–3942, 2020.

[26] M. Olsen, M. Hummelgård, and H. Olin, "Surface modifications by field induced diffusion," *PLoS ONE*, vol. 7, no. 1, p. 30106, 2012.

[27] T. T. Tsong, "Effects of an electric field in atomic manipulations," *Physical Review B*, vol. 44, pp. 13703–13710, Dec 1991.

[28] T. M. Mayer, J. E. Houston, G. E. Franklin, A. A. Erchak, and T. A. Michalske, "Electric field induced surface modification of Au," *Journal of Applied Physics*, vol. 85, pp. 8170–8177, Jun 1999.

[29] P. Y. Convers, D. N. McCarthy, A. Sattar, F. Natali, S. C. Hendy, and S. A. Brown, "Electrical signature of nanoscale coalescence in a percolating Bi nanocluster film," *Physical Review B*, vol. 82, no. 11, pp. 1–5, 2010.

[30] T. H. Lim, D. McCarthy, S. C. Hendy, K. J. Stevens, S. A. Brown, and R. D. Tilley, "Real-time TEM and kinetic Monte Carlo studies of the coalescence of decahedral gold nanoparticles," *ACS Nano*, vol. 3, no. 11, pp. 3809–3813, 2009.

[31] G. C. Kuczynski, "Study of the sintering of glass," *Journal of Applied Physics*, vol. 20, pp. 1160–1163, Dec 1949.

[32] F. A. Nichols and W. W. Mullins, "Morphological changes of a surface of revolution due to capillarity-induced surface diffusion," *Journal of Applied Physics*, vol. 36, no. 6, pp. 1826–1835, 1965.

[33] T. H. Kim, X. G. Zhang, D. M. Nicholson, B. M. Evans, N. S. Kulkarni, B. Radhakrishnan, E. A. Kenik, and A. P. Li, "Large discrete resistance jump at grain boundary in copper nanowire," *Nano Letters*, vol. 10, no. 8, pp. 3096–3100, 2010.

[34] S. L. Johnson, A. Sundararajan, D. P. Hunley, and D. R. Strachan, "Memristive switching of single-component metallic nanowires," *Nanotechnology*, vol. 21, no. 12, p. 125204, 2010.

[35] T. B. Song, Y. Chen, C. H. Chung, Y. Yang, B. Bob, H. S. Duan, G. Li, K. N. Tu, and Y. Huang, "Nanoscale Joule heating and electromigration enhanced ripening of silver nanowire contacts," *ACS Nano*, vol. 8, no. 3, pp. 2804–2811, 2014.

[36] R. Hoffmann-Vogel, "Electromigration and the structure of metallic nanocontacts," *Applied Physics Reviews*, vol. 4, no. 3, p. 031302, 2017.

[37] A. Halbritter, S. Csonka, O. Y. Kolesnychenko, G. Mihály, O. I. Shklyarevskii, O. I. Shklyarevskii, and H. van Kempen, "Connective neck evolution and conductance steps in hot point contacts," *Physical Review B*, vol. 65, pp. 454131–454138, Jan 2002.

[38] Y. H. Wen, Y. Zhang, J. C. Zheng, Z. Z. Zhu, and S. G. Sun, "Orientation-dependent structural transition and melting of Au nanowires," *Journal of Physical Chemistry C*, vol. 113, no. 48, pp. 20611–20617, 2009.

[39] A. Volk, D. Knez, P. Thaler, A. W. Hauser, W. Grogger, F. Hofer, and W. E. Ernst, "Thermal instabilities and Rayleigh breakup of ultrathin silver nanowires grown in helium nanodroplets," *Physical Chemistry Chemical Physics*, vol. 17, no. 38, pp. 24570–24575, 2015.

[40] M. Schnedlitz, M. Lasserus, D. Knez, A. W. Hauser, F. Hofer, and W. E. Ernst, "Thermally induced breakup of metallic nanowires: Experiment and theory," *Physical Chemistry Chemical Physics*, vol. 19, no. 14, pp. 9402–9408, 2017.

[41] Y. H. Wen, Z. Z. Zhu, R. Zhu, and G. F. Shao, "Size effects on the melting of nickel nanowires: A molecular dynamics study," *Physica E: Low-Dimensional Systems and Nanostructures*, vol. 25, no. 1, pp. 47–54, 2004.

[42] P. Moskovkin, M. Panshenskov, S. Lucas, and A. V. Solov'yov, "Simulation of nanowire fragmentation by means of kinetic Monte Carlo approach: 2D case," *Physica Status Solidi (B) Basic Research*, vol. 251, no. 7, pp. 1456–1462, 2014.

[43] W. Wu, T. Pavloudis, A. V. Verkhovtsev, A. V. Solov'yov, and R. E. Palmer, "Molecular dynamics simulation of nanofilament breakage in neuromorphic nanoparticle networks," *Nanotechnology*, vol. 33, p. 275602, Jul 2022.

[44] S. Koo, J. Park, S. Koo, and K. Kim, "Local heat dissipation of Ag nanowire networks examined with scanning thermal microscopy," *Journal of Physical Chemistry C*, vol. 125, no. 11, pp. 6306–6312, 2021.

[45] C. L. Kim, J. Y. Lee, D. G. Shin, J. S. Yeo, and D. E. Kim, "Mechanism of heat-induced fusion of silver nanowires," *Scientific Reports*, vol. 10, p. 9271, 2020.

[46] J. Y. Ruzicka, F. Abu Bakar, C. Hoeck, R. Adnan, C. Mcnicoll, T. Kemmitt, B. C. Cowie, G. F. Metha, G. G. Andersson, and V. B. Golovko, "Toward control of gold cluster aggregation on TiO2 via surface treatments," *Journal of Physical Chemistry C*, vol. 119, pp. 24465–24474, Oct 2015.

[47] A. V. Verkhovtsev, Y. Erofeev, and A. V. Solov'yov, "Soft landing of metal clusters on graphite: A molecular dynamics study," *The European Physical Journal D*, vol. 74, p. 205, Oct 2020.

[48] L. Bardotti, P. Jensen, A. Hoareau, M. Treilleux, B. Cabaud, A. Perez, and F. C. S. Aires, "Diffusion and aggregation of large antimony and gold clusters deposited on graphite," *Surface Science*, vol. 367, pp. 276–292, Dec 1996.

[49] Y. V. Sharvin, "A possible method for studying Fermi surfaces," *Sov. Phys. JETP*, vol. 21, p. 655, 1965.

[50] G. Wexler, "The size effect and the non-local Boltzmann transport equation in orifice and disk geometry," *Proceedings of the Physical Society*, vol. 89, no. 4, pp. 927–941, 1966.

[51] J. A. Torres, J. I. Pascual, and J. J. Sáenz, "Theory of conduction through narrow constrictions in a three-dimensional electron gas," *Physical Review B*, vol. 49, pp. 16581–16584, Jun 1994.

[52] M. López-Suárez, C. Melis, L. Colombo, and W. Tarantino, "Modeling charge transport in gold nanogranular films," *Physical Review Materials*, vol. 5, p. 126001, Dec 2021.

[53] D. Erts, H. Olin, L. Ryen, and A. Thölén, "Maxwell and Sharvin conductance in gold point contacts investigated using TEM-STM," *Physical Review B*, vol. 61, no. 19, pp. 12725–12727, 2000.

[54] I. A. Solov'yov, A. V. Yakubovich, P. V. Nikolaev, I. Volkovets, and A. V. Solov'yov, "MesoBioNano explorer-A universal program for multiscale computer simulations of complex molecular structure and dynamics," *Journal of Computational Chemistry*, vol. 33, no. 30, pp. 2412–2439, 2012.

[55] G. B. Sushko, I. A. Solov'yov, and A. V. Solov'yov, "Modeling MesoBioNano systems with MBN Studio made easy," *Journal of Molecular Graphics and Modelling*, vol. 88, pp. 247–260, 2019.

[56] R. P. Gupta, "Lattice relaxation at a metal surface," *Physical Review B*, vol. 23, no. 12, pp. 6265–6270, 1981.

[57] F. Cleri and V. Rosato, "Tight-binding potentials for transition metals and alloys," *Physical Review B*, vol. 48, pp. 22–33, Jul 1993.

[58] D. W. Brenner, "Empirical potential for hydrocarbons for use in simulating the chemical vapor deposition of diamond films," *Physical Review B*, vol. 42, pp. 9458–9471, Nov 1990.

[59] V. V. Dick, I. A. Solov'Yov, and A. V. Solov'Yov, "Fragmentation pathways of nanofractal structures on surfaces," *Physical Review B*, vol. 84, p. 115408, 2011.

[60] A. Einstein, *Investigations on the Theory of the Brownian Movement*. Dover Books on Physics Series, Dover Publications, 1956.

[61] G. Antczak and G. Ehrlich, *Surface Diffusion: Metals, Metal Atoms, and Clusters*. Cambridge University Press, 2010.

[62] K. K. Nanda, S. N. Sahu, and S. N. Behera, "Liquid-drop model for the size-dependent melting of low-dimensional systems," *Physical Review A - Atomic, Molecular, and Optical Physics*, vol. 66, no. 1, p. 132081, 2002.

[63] W. Hu, S. Xiao, J. Yang, and Z. Zhang, "Melting evolution and diffusion behavior of vanadium nanoparticles," *European Physical Journal B*, vol. 45, pp. 547–554, Jun 2005.

[64] M. J. De Ruijter, J. De Coninck, and G. Oshanin, "Droplet spreading: Partial wetting regime revisited," *Langmuir*, vol. 15, no. 6, pp. 2209–2216, 1999.

[65] Š. Šikalo and E. N. Ganić, "Phenomena of droplet-surface interactions," *Experimental Thermal and Fluid Science*, vol. 31, no. 2, pp. 97–110, 2006.

[66] S. Arcidiacono, N. Bieri, D. Poulikakos, and C. Grigoropoulos, "On the coalescence of gold nanoparticles," *International Journal of Multiphase Flow*, vol. 30, pp. 979–994, Jul 2004.

[67] H. Ibach and H. Lüth, *Solid-State Physics*. Berlin, Heidelberg: Springer Berlin Heidelberg, 2009.

Chapter 6 The Melting Behaviour of Pb-Al Core-shell Nanoclusters

The previous two chapters have considered the formation and breakage of links between Au clusters. Au clusters are robust against oxidation, and have been shown a promising material in neuromorphic computing devices. However, Au is a rare and expensive metal. One approach to reduce the usage of precious metals in nanoclusters is to create core-shell clusters, where the surface comprises a precious metal and the core a more abundant and less expensive metal. The idea behind this architecture is to retain the conductivity properties of the precious metal by fixing it on the outer surface, while the bulk of the nanoclusters is made of a cheaper material. Meanwhile, the core-shell clusters may present novel and unique characteristics compared to elemental clusters, which may bring about new possibilities in cluster-based neuromorphic devices. If such clusters are to be employed in electronic devices, an understanding of their intrinsic thermal stability is crucial. This chapter carries out a simulation research into this topic by investigating the behaviour of Pb-Al core-shell clusters under elevated temperatures. Here, aluminum (Al) is used in place of gold (Au) in the shell of the cluster. This choice allows for a more effective future experimental comparison and provides a solution to a common imaging issue in STEM. Usually, core-shell clusters with Au shells do not yield a good contrast in Scanning Transmission Electron Microscopy (STEM) due to the high atomic number of gold. However, the use of a low-atomic number material for the shell, such as Al, results in a significant Z contrast that allows the high-atomic number Pb core to be clearly imaged in dark-field STEM, as discussed by Yamashita in 2018 [1]. This approach not only enables more effective imaging but also explores the potential of using more cost-effective materials in the fabrication of core-shell clusters for neuromorphic devices.

6.1 Introduction

Metal clusters have fantastic properties and numerous potential applications in the catalysis, sensor, optoelectronics and biomedical fields [2–6]. In the context of neuro-

morphic computing, metal clusters created by deposition technologies can be made into synapse devices which function as a single neuron in a neuromorphic computing system and shows non-ohmic switching behaviour [7–12]. Several previous studies have identified various elemental metal clusters that can be used to create such devices, like Au [13] and Sn [14]. However, the number of elemental metals that are robust and functional against the oxidation at the nanoscale is very limited [15]. In recent years, bimetallic alloy clusters have garnered significant attention due to their distinctive physical and chemical properties that may differ from those of elemental metal clusters. [16–20]. These alloy clusters offer the possibilities for new materials to be used in the creation of cluster-based neuromorphic switching devices.

Critical factors that determine the properties of the clusters are their composition, size, structure and, in alloy nanoclusters, the distribution of the different atoms in the cluster. By tuning these factors, clusters with customised properties can be fabricated [21–23]. In order to realise such an approach, an extensive understanding of the properties of the clusters is essential. One of the most critical properties is the melting behaviour, which has a crucial effect on the fabrication process of these clusters [24].

Metal clusters have a much lower melting point than the corresponding bulk metals due to a significant surface-to-volume ratio. The depression of the melting point with decreasing size has been reported experimentally and theoretically for various metal clusters [24–26]. However, several exceptions have been found, including Sn [27, 28] and Ga [29]; for these metals, the melting point is much higher than that of the bulk materials when the size is less than 40 atoms. Meanwhile, it has also been shown that the melting point does not necessarily vary monotonically with the size in some particular systems [30–32]. In modern experiments, the melting of massive clusters is usually measured by electron or X-ray diffraction and nanocalorimetry [33–36]. However, these techniques are not applicable to researching the behaviour of the clusters individually in vacuum, because it is difficult to collect the signal at such a small scale [37]. STEM has been widely used to observe the behaviour of the clusters individually [38,39]. Due to its strong chemical sensitivity [40], clusters with multiple components and a complex structure can be observed in situ by STEM [41–43]. The recently developed temperature-control sample

119

holder [44] has made STEM a very strong tool for observing the melting behaviours of metal clusters [45].

The melting behaviour of the core-shell clusters can be significantly different from that of the corresponding monometallic particles. Molecular dynamics simulations have been performed on various kinds of systems, including Au-Pt [46, 47], Pt-Pd [48], Au-Cu [49] and Ag-Cu [50]. A two-stage melting behaviour has been observed in these systems, and the melting points of the cores and shells are correlated with the core-shell ratio and the structure. Furthermore, a segregation behaviour of the constituent elements in bimetallic nanoparticles has been reported both experimentally and theoretically due to the different surface energies and diffusivities between each of the constituent metals [51–53]. The melting properties shown by the systems mentioned above are not necessarily easy to observe in situ using STEM, due to the low contrast between their constituent elements. Meanwhile, previous atomistic-level works concerning the melting behaviour of bimetallic core-shell nanoparticles lack a thorough study of the effect of the shell thickness on the melting behaviour.

In this chapter, an atomistic study of the melting process of Pb-Al core-shell clusters during continuous heating was performed. The choice of these elements is based on the high contrast of the elements in STEM, which makes comparison with further in situ observations easier in the future. A series of molecular dynamics simulations of core-shell clusters with a fixed Pb_{147} core and a varying Al shell thickness have been employed to provide insights into the melting behaviour. A structural analysis has been performed and a special behaviour has been observed in which the core atoms break the 'prison' of the shell and are segregated with the shell atoms after the system melts.

6.2 Methodology

6.2.1 Initial configuration

In this work, closed-shell magic-number cuboctahedral clusters were used as an example to demonstrate the melting process of the Pb-Al core-shell cluster. This structure conforms to the preferred lattice of Pb and Al (fcc) and simplifies the construction of
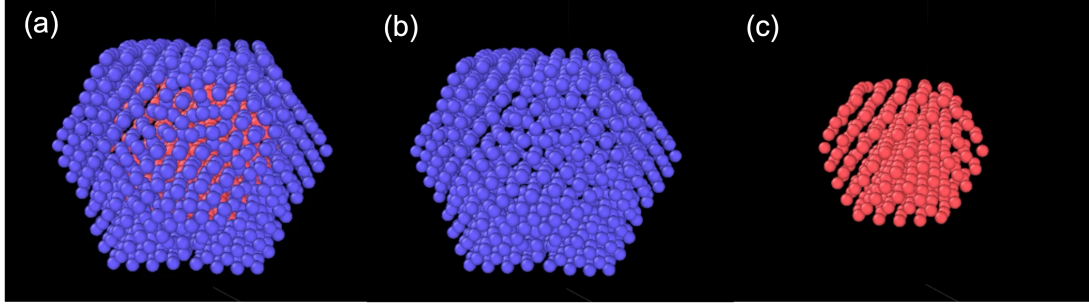
Figure 6-1 The structure of the $Pb_{147}Al_{776}$ core-shell cluster after the initial relaxation. (a) The whole core-shell structure; Pb is marked in red and Al is marked in blue. (b) The shell part of the cluster. (c) The Pb_{147} core of the cluster.

models and representations. The following series of cuboctahedral Pb clusters was used: Pb_{561}, Pb_{923}, Pb_{1415}, Pb_{2058}, Pb_{2869}. The core-shell structure was achieved by replacing the outer-shell Pb atoms with Al while keeping a Pb_{147} cluster in the centre unchanged. Thus, the resulting initial configurations of the core-shell clusters were $Pb_{147}Al_{414}$, $Pb_{147}Al_{776}$, $Pb_{147}Al_{1268}$, $Pb_{147}Al_{1911}$ and $Pb_{147}Al_{2722}$ (2 to 6 layers of Al atoms surrounding the Pb_{147} core). A free Pb_{147} cluster was also simulated for comparison purposes. Figure 6-1 shows the structure of the $Pb_{147}Al_{776}$ cluster after the initial relaxation in (a), the Al shell of this cluster in (b) and the Pb_{147} core in (c). Mismatches and defects of the shell can be seen after the energy minimisation in Figure 6-1 (a) due to the difference between the lattice constants of the core and shell atoms.

6.2.2   Simulation details

All the simulations were carried out with LAMMPS code [54], and the observation and analyses of the structural results were performed with OVITO [55]. The difference between the package with previous chapters is project-based. An empirical many-body embedded atom model (EAM) potential from Landa [56] was employed to describe the interaction between atoms. The potential was selected for its ability to accurately represent the properties of Pb-Al alloys, as demonstrated by its well-fitted phase diagram [56]. The MD simulations were carried out in the canonical ensemble (NVT), and the Nose-Hoover

thermostat was used to maintain the constant-temperature condition. No periodic boundary conditions were applied to ensure the simulation of isolated nanoparticles. Before the MD simulations, the initial clusters were fully relaxed. The integral calculation was done with the Verlet algorithm with a time step of 2 fs to reach a balance between the accuracy and computational resources. The temperature was set to increase from 0 K to 1400 K to fully show the melting process, with an increasing rate of 14 K/ns. The rate of the increase in the temperature was low enough to consider the system to be in an equilibrium state during the simulation process, which is proven by comparing with the simulations in constant temperatures. Each initial configuration was simulated five times to reduce the randomness in the results.

6.3 Results and discussion

6.3.1 The melting behaviour

The melting behaviour of a $Pb_{147}Al_{1268}$ core-shell cluster is shown in Figure 6-2 (a)–(d). Figure 6-2 (e)–(h) shows the corresponding core structure. The initial configuration after the relaxation is shown in Figure 6-2 (a). The melting process can generally be divided into three phases. During the core melting phase, as the temperature increases, the intense core atom vibration can be observed which indicate the melting of the core part. Defects are randomly formed on the shell part due to the perturbation of the atoms, as shown in Figure 6-2 (b). During the 'prison-break' phase, the core atoms eventually find a defect to break through because of the surface energy and reach the cluster's surface, as shown in Figure 6-2 (c). During the segregation phase, the core atoms gradually come out of the shell, as shown in Figure 6-2 (d), and form a segregated nanocluster, otherwise known as a Janus nanocluster (a reference to the two-faced god of ancient Rome). The shell part melts during the 'prison-break' phase in most cases, but for the smallest $Pb_{147}Al_{414}$ cluster, it will melt before the melting of the core.

At a certain level of shell thickness (specifically, for $Pb_{147}Al_{1268}$ and $Pb_{147}Al_{1911}$; the later ones are shown in Figure 6-3), the surface segregation will happen in more than one step. A part of the core is sometimes separated and squeezed out of the Al shell,

122
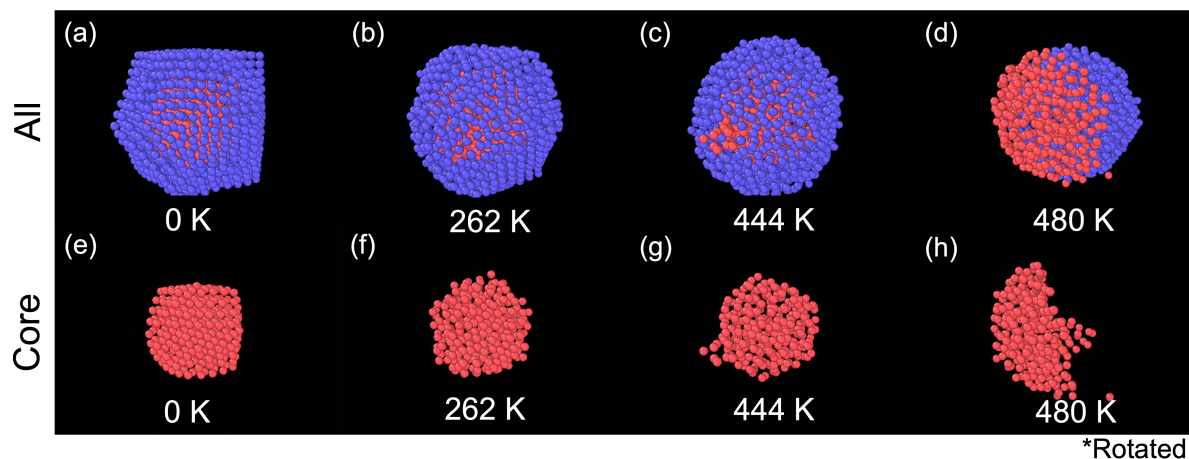
Figure 6-2 The melting behaviour of a $Pb_{147}Al_{1268}$ core-shell cluster. (a) The initial structure. (b) The core of the cluster is melted. (c) Core atoms begin to break out of the surface. (d) The core atoms completely break out. Panels (e)–(h) show the corresponding Pb core structures of panels (a)–(d). Panel (h) is rotated to show the structure during the coming-out process of the core atoms.

while the rest of the core remains inside the cluster (Figure 6-3 (a)). The remaining part in the centre can break out later at a higher temperature (Figure 6-3 (b)). The appearance of this multi-step segregation process was observed in all five simulations of the same structures, but no rule could be extracted concerning the number of atoms in the temporary remaining part.

Previous theoretical studies on segregation in nanoclusters focused on either neighbouring elements in the same period of the periodic table or elements in the same group of the periodic table [52], and they cannot be applied in our case. However, density functional theory (DFT) and MD studies on the segregation of Pb and Al in nano-crystalline and bulk materials showed that the segregation is governed by a combination of electronic effects and the mismatch effect due to the different lattice constants and defects [57–59]. Clear grain boundaries between the Al and Pb phases were observed in these works, similar to our results for the Pb-Al clusters.
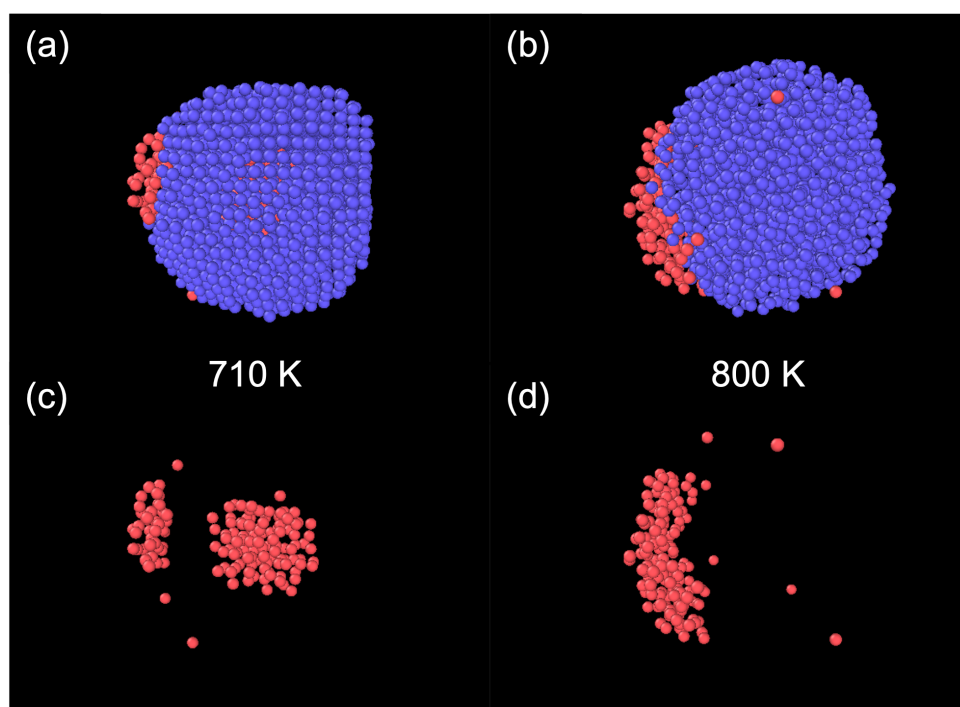
Figure 6-3 (a) The two-step break-out in a $Pb_{147}Al_{1911}$ nanocluster. The core atoms undergo scission and are partially separated out, while the rest of the core remains inside the shell. (b) The core atoms will eventually break out at a higher temperature. Panels (c) and (d) show the core atoms corresponding to (a) and (b).

6.3.2 Structure analysis

The "breaking out" and surface segregation behaviour is crucially affected by the melting of the cluster. A pair distribution function (PDF) analysis was performed on the clusters to shed light onto their melting process. Previous research has shown the relationship between the averaged PDF and the melting behaviour of the clusters [60]. An averaged PDF of 50 recorded frames within a temperature range of 5 K and a time range of 357 ps, has been applied to the core and shell atoms of the Pb-Al core-shell clusters, respectively. The averaged PDF within the 5 K range is calculated to represent the PDF at the middle temperature of the 5K range. This average can efficiently reduce the perturbation in PDF data and provide a proper estimation the melting temperature. The averaged PDF of the core atoms of $Pb_{147}Al_{2722}$ at different temperatures is shown in Figure 6-4 (a). The nearest neighbour distance ($\sigma \approx 2.5$ Å) is given by the occurrence of the first peak. As the temperature increases, the $\sqrt{2}\sigma$ peak (second peak) of the function begins to decrease and vanishes at the melting point. In Figure 6-4 (a), the melting point of the Pb core is located from 600 K $\sim$ 700 K. The accuracy of the melting point can be increased by repeatedly performing the averaged PDF analysis in this temperature range every 10 K. In this case, the extracted melting point of the core was 670 ± 10 K. The initial and melted structures of the core are shown in Figure 6-4 (b) and (c). The "break-out" has not yet happened, as shown in Figure 6-4 (c). It is important to note that the surface break-out event always occurs after the melting of the core in all our simulations.

The adaptive common neighbor analysis (a-CNA) [61] has also been used to study the structural changes that occur during the melting process of core-shell clusters. Figure 6-5 shows the melting process of a $Pb_{147}Al_{776}$ cluster. In the initial state shown in Figure 6-5 (a),(f), the atoms after the outer layer are all recognised by the algorithm as crystalline (face-centered cubic, hexagonal close-packed, body-centered cubic or icosahedral). The outer layer atoms, despite being in a clearly crystalline formation, are not recognised by the algorithm as such since they lack the required amount of neighbours. After a period of perturbation, shown in Figure 6-5 (b),(g), the core of the cluster melts first (Figure 6-5 (c),(h)). The break-out event then occurs almost immediately after the core melts.
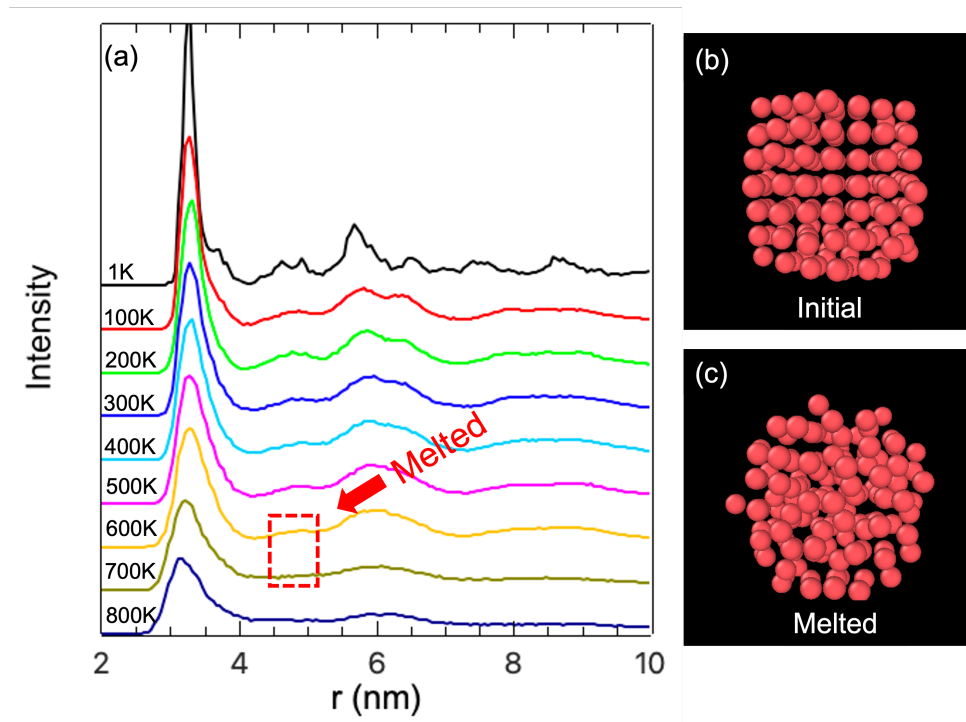
Figure 6-4 (a) Averaged pair distribution function (PDF) of the core atoms of the $Pb_{147}Al_{2722}$ core-shell cluster in different temperature ranges. (b) The initial core structure of the $Pb_{147}Al_{2722}$ cluster. (c) The structure of the core when the melting happens. It can be seen that the break-out event has not yet occurred when the core is melting.
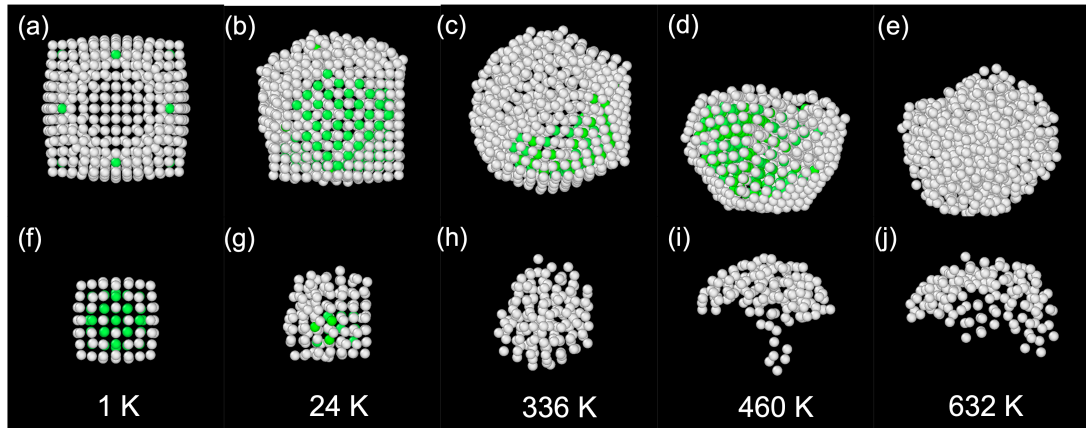
Figure 6-5 The adaptive common neighbor analysis (a-CNA) algorithm is used to study the melting process of a $Pb_{147}Al_{776}$ cluster. The melting processes of the core (f)–(j) and shell (a)–(e) are shown separately. Crystalline atoms identified by a-CNA are marked in green. In the initial setting (a),(f), the cluster is in a crystalline state. After a period of perturbation (b),(g), the core melts (c),(h) and breaks out of the shell (d),(i). The shell maintains its crystalline structure during the break-out process. As the temperature increases (e),(j), the shell eventually melts as well.

As shown in Figure 6-5 (d),(i), the shell remains crystalline during the entire break-out event. As the temperature increases (Figure 6-5 (e),(j)), the shell eventually melts as well. However, clusters with thicker shells ($Pb_{147}Al_{1268\sim2722}$) behave differently, and their behaviour will be discussed in the next section and in Figure 6-7.

The proportions of crystalline atoms identified by a-CNA in core-shell clusters with different shell thicknesses during the entire simulation process are shown in Figure 6-6. The data for $Pb_{147}Al_{414}$ is not shown because the number of atoms in the cluster that are marked as crystalline are too small after the simulation starts. This may be due to a combination of factors, including the lower melting point due to the smaller size, a higher proportion of surface atoms, and a more unstable structure due to defects introduced by shell atoms. The data for $Pb_{147}Al_{776\sim2122}$ are shown separately in (a)–(d). According to the definition of melting, the number of crystalline atoms show a sudden decrease when melting occurs. This is more obvious in the shell atoms due to the larger

127
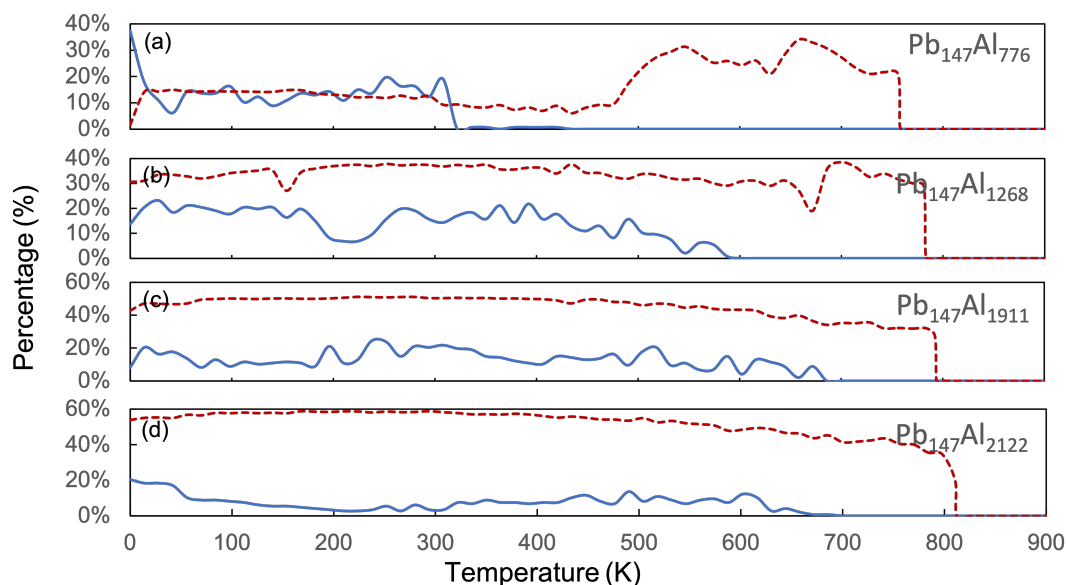
Figure 6-6 The proportions of crystalline atoms marked by a-CNA during the simulation, i.e. the crystalline Pb/the total Pb and the crystalline Al/the total Al. The blue solid lines represent the Pb core and the red dashed lines represent the Al shell. The data of $Pb_{147}Al_{776\sim2122}$ are shown in (a)–(d), separately. The data of $Pb_{147}Al_{414}$ is not shown because no atom will be marked crystalline (fcc) after the simulation starts.

number of atoms. Although there are large perturbations in the data for the core, the melting temperature can still be accurately determined: after a certain point the atoms of interest are all recognised as amorphous. All the melting temperatures agree well with those from the PDF analysis. It can be observed that as the shell thickness of the core-shell clusters increases, the melting point of both the core and shell increases, with the increase in the core being more pronounced due to the stronger constraints of a thicker shell. Additionally, a sharp increase in the crystalline proportion of the shell can be observed at around 500 K in the $Pb_{147}Al_{776}$ cluster. This is because after the break-out event, the cluster becomes a Janus nanoparticle, and the shell atoms reorganize into a structure with more bulk atoms that can be recognized by a-CNA.

6.3.3 Melting temperature and timing of the break-out event

The relationship between the melting point and the break-out event for different shell thicknesses (2–6 atom layers, $Pb_{147}Al_{414\sim2722}$) is shown in Figure 6-7. The melting points of an elemental Pb_{147} cluster and bulk Pb were simulated using the same parameters that were used in our previous runs for comparison purposes. The melting point of the Pb_{147} core has a monotonic positive correlation with the thickness of the shell. The core of the $Pb_{147}Al_{414}$ cluster (2 shell layers) has a lower melting point than the pure Pb_{147} cluster, although it is covered by the shell. In the $Pb_{147}Al_{1911}$ and $Pb_{147}Al_{2722}$ clusters (5 and 6 shell layers, respectively), the melting point of the core is even higher than the melting point of bulk Pb. The shell melts at a higher temperature compared to the core, except in the case of $Pb_{147}Al_{414}$ (2 shell layers). The melting point of the shell has a monotonic positive correlation with the thickness as well.

The beginning of the break-out occurs just after the core melts. $Pb_{147}Al_{414}$ is an exception: the break-out event happens at a higher temperature after the melting of the shell and core because of its relatively low total kinetic energy when the core is melted which could not provide enough perturbation for the break-out process. Another exception is the largest $Pb_{147}Al_{2722}$ cluster (6 shell layers). The core atoms stay inside the cluster due to the stability of the very big shell until the shell is totally melted. The break-out process happens in two steps in clusters with 4 or 5 shell layers ($Pb_{147}Al_{1268}$ and $Pb_{147}Al_{1911}$). The first break-out happens just at the beginning of melting, when the whole structure is relatively stable, while the remaining Pb atoms in the core escape when the shell is completely melted.

The melting point of the $Pb_{147}Al_{414}$ cluster is lower than that of the elemental Pb_{147} cluster; this has not been observed in previous studies on the melting behaviour of core-shell clusters. The difference between the lattice constants of Al and Pb results in a mismatch and causes defects during the initial relaxation of the core-shell structures. This is universal for all the core-shell clusters, and the mismatch part can be easily observed in the structure, as in Figure 6-1 (c). Previous research shows that the melting point of the nanoparticle can be depressed by the insoluble impurities due to the perturbation of the
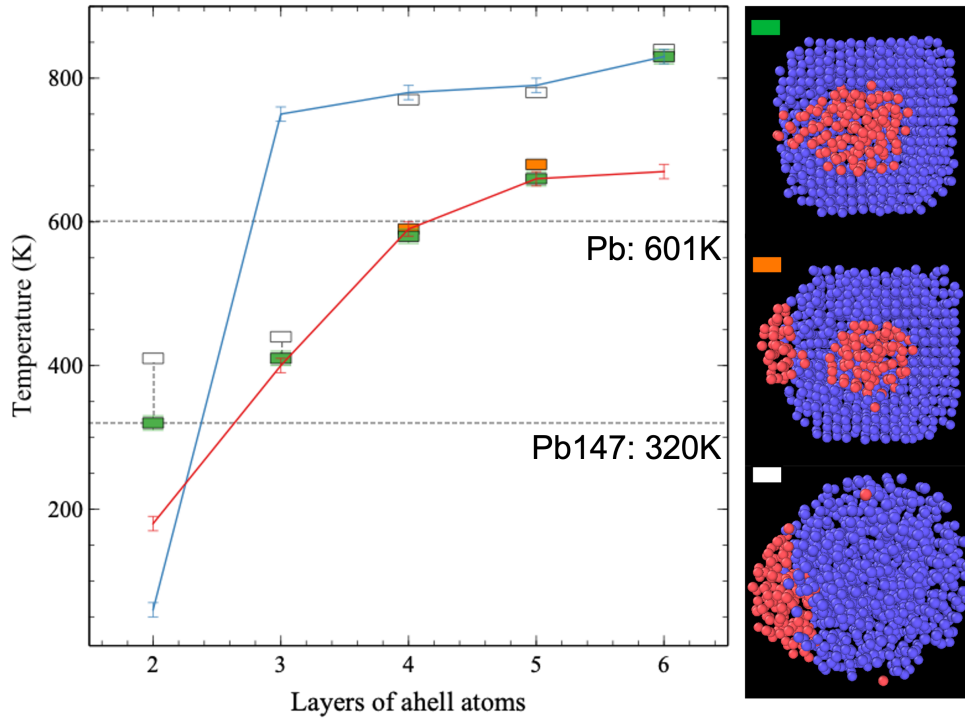
Figure 6-7 Melting and break-out event temperature of the $Pb_{147}Al_{414\sim2722}$ core-shell clusters (2$\sim$6 layers of shell atoms). Orange line: core melting temperature. Blue line: shell melting temperature. Vertical line: duration of the break-out, which is quantified from the moment the first core atom reaches the surface to the moment when the interface between the two metals smooths out.. Boxes: Green: the beginning of the break-out. Orange: part of the core remains inside. White: all of the core atoms are out. The melting points of an elemental Pb_{147} nanocluster and bulk Pb for our simulation settings are marked with horizontal lines.

130

lattice in the host clusters [62]. In the $Pb_{147}Al_{414}$ cluster, the mass ratio is Al:Pb = 0.36:1. Al and Pb are insoluble, and defects can be seen on all the core structures (Figure 6-1 (c), Figure 6-4 (b), etc.). Aluminium can be seen as an impurity in the Pb core in our case to explain this melting point depression. In the $Pb_{147}Al_{1911}$ and $Pb_{147}Al_{2722}$ clusters (5 and 6 shell layers), the melting point of the core is even higher than that of bulk Pb. This result may be due to the pressure effect introduced by the increasing thickness of the Al shell, which has been previously mentioned in works on Al nanoparticles [63].

The trigger for the break-out shifts from the melting of the core to the melting of the shell as the shell gets thicker. This is probably due to the fact that the thin shell has a lower melting point and is not robust enough to prevent the liquid state of the Pb atoms from getting out. The two-step break-out, which appears when 4 or 5 shell layers are present, is the intermediate scenario between these two conditions.

6.4   Conclusions

In summary, the melting process of Pb-Al core-shell clusters with different Al-shell thicknesses has been studied using molecular dynamic simulations. The Pb core atoms will break out of the Al shell and the nanocluster will end up in a segregated state after the melting of the clusters. The process may happen in two steps, in which case part of the core remains inside the cluster while the other part breaks out. The melting point of the Pb core can either be depressed or elevated by the presence of the Al shell, depending on the shell thickness. The thinner shell can be seen as insoluble impurities that introduce defects and mismatches to depress the melting point of the core, while the thicker shell elevates the melting point due to the introduction of the pressure effect. The timing of the break-out shifts from the melting of the core to the melting point of the shell as the shell gets thicker.

Our research has provided new insight into the melting behaviour of the core-shell clusters. This result indicates that the stability and melting properties of the core-shell clusters can be tuned by adjusting the thickness of the shell. It also provides a prediction and a reference for future experimental studies, especially STEM observation results.

References

[1] S. Yamashita, J. Kikkawa, K. Yanagisawa, T. Nagai, K. Ishizuka, and K. Kimoto, "Atomic number dependence of Z contrast in scanning transmission electron microscopy," *Scientific Reports*, vol. 8, p. 12325, aug 2018.

[2] W. E. Kaden, T. Wu, W. A. Kunkel, and S. L. Anderson, "Electronic structure controls reactivity of size-selected PD clusters adsorbed on TiO2 surfaces," *Science*, vol. 326, pp. 826–829, Nov 2009.

[3] N. Cheng, S. Stambula, D. Wang, M. N. Banis, J. Liu, A. Riese, B. Xiao, R. Li, T. K. Sham, L. M. Liu, G. A. Botton, and X. Sun, "Platinum single-atom and cluster catalysis of the hydrogen evolution reaction," *Nature Communications*, vol. 7, p. 13638, 2016.

[4] B. Xie, B. Ding, P. Mao, Y. Wang, Y. Liu, M. Chen, C. Zhou, H. Wen, S. Xia, M. Han, R. E. Palmer, G. Wang, and J. Hu, "Metal nanocluster—metal organic framework—polymer hybrid nanomaterials for improved hydrogen detection," *Small*, p. 2200634, Apr 2022.

[5] J. A. Scholl, A. L. Koh, and J. A. Dionne, "Quantum plasmon resonances of individual metallic nanoparticles," *Nature*, vol. 483, no. 7390, pp. 421–427, 2012.

[6] P. Cao, X. Wu, W. Zhang, L. Zhao, W. Sun, and Z. Tang, "Killing oral bacteria using metal-organic frameworks," *Industrial and Engineering Chemistry Research*, vol. 59, pp. 1559–1567, Jan 2020.

[7] M. Mirigliano, D. Decastri, A. Pullia, D. Dellasega, A. Casu, A. Falqui, and P. Milani, "Complex electrical spiking activity in resistive switching nanostructured Au two-terminal devices," *Nanotechnology*, vol. 31, no. 23, p. 234001, 2020.

[8] A. Sattar, S. Fostner, and S. A. Brown, "Quantized conductance and switching in percolating nanoparticle films," *Physical Review Letters*, vol. 111, no. 13, p. 136808, 2013.

[9] M. Mirigliano, F. Borghi, A. Podestà, A. Antidormi, L. Colombo, and P. Milani, "Non-ohmic behavior and resistive switching of Au cluster-assembled films beyond the percolation threshold," *Nanoscale Advances*, vol. 1, no. 8, pp. 3119–3130, 2019.

[10] S. K. Bose, J. B. Mallinson, R. M. Gazoni, and S. A. Brown, "Stable self-assembled atomic-switch networks for neuromorphic applications," *IEEE Transactions on Electron Devices*, vol. 64, no. 12, pp. 5194–5201, 2017.

[11] J. B. Mallinson, S. Shirai, S. K. Acharya, S. K. Bose, E. Galli, and S. A. Brown, "Avalanches and criticality in self-organized nanoscale networks," *Science Advances*, vol. 5, no. 11, p. eaaw8483, 2019.

[12] C. Minnai, M. Mirigliano, S. A. Brown, and P. Milani, "The nanocoherer: An electrically and mechanically resettable resistive switching device based on gold clusters assembled on paper," *Nano Futures*, vol. 2, no. 1, p. 1002, 2018.

[13] C. Minnai, A. Bellacicca, S. A. Brown, and P. Milani, "Facile fabrication of complex networks of memristive devices," *Scientific Reports*, vol. 7, no. 1, p. 7955, 2017.

[14] M. D. Pike, S. K. Bose, J. B. Mallinson, S. K. Acharya, S. Shirai, E. Galli, S. J. Weddell, P. J. Bones, M. D. Arnold, and S. A. Brown, "Atomic scale dynamics drive brain-like avalanches in percolating nanostructured networks," *Nano Letters*, vol. 20, no. 5, pp. 3935–3942, 2020.

[15] M. T. Reetz, S. A. Quaiser, M. Winter, J. A. Becker, R. Schäfer, U. Stimming, A. Marmann, R. Vogel, and T. Konno, "Nanostructured Metal Oxide Clusters by Oxidation of Stabilized Metal Clusters with Air," *Angewandte Chemie International Edition in English*, vol. 35, pp. 2092–2094, oct 1996.

[16] B. B. Xiao, Y. F. Zhu, X. Y. Lang, Z. Wen, and Q. Jiang, "$Al_{13}@Pt_{42}$ core-shell cluster for oxygen reduction reaction," *Scientific Reports*, vol. 4, p. 5205, Dec 2014.

[17] D. Sun, Y. Tian, Y. Zhang, Z. Xu, M. Y. Sfeir, M. Cotlet, and O. Gang, "Light-harvesting nanoparticle core-shell clusters with controllable optical output," *ACS Nano*, vol. 9, pp. 5657–5665, Jun 2015.

[18] F. Tao, M. E. Grass, Y. Zhang, D. R. Butcher, J. R. Renzas, Z. Liu, J. Y. Chung, B. S. Mun, M. Salmeron, and G. A. Somorjai, "Reaction-driven restructuring of Rh-Pd and Pt-Pd core-shell nanoparticles," *Science*, vol. 322, pp. 932–934, Nov 2008.

[19] B. N. Wanjala, J. Luo, R. Loukrakpam, B. Fang, D. Mott, P. N. Njoki, M. Engelhard, H. R. Naslund, J. K. Wu, L. Wang, O. Malis, and C. J. Zhong, "Nanoscale alloying, phase-segregation, and core-shell evolution of gold-platinum nanoparticles and their electrocatalytic effect on oxygen reduction reaction," *Chemistry of Materials*, vol. 22, pp. 4282–4294, Jul 2010.

[20] C. J. Serpell, J. Cookson, D. Ozkaya, and P. D. Beer, "Core@shell bimetallic nanoparticle synthesis via anion coordination," *Nature Chemistry*, vol. 3, pp. 478–483, Jun 2011.

[21] E. C. Tyo and S. Vajda, "Catalysis by clusters with precise numbers of atoms," *Nature Nanotechnology*, vol. 10, pp. 577–588, Jul 2015.

[22] D. M. Wells, G. Rossi, R. Ferrando, and R. E. Palmer, "Metastability of the atomic structures of size-selected gold nanoparticles," *Nanoscale*, vol. 7, no. 15, pp. 6498–6503, 2015.

[23] F. Yin, Z. W. Wang, and R. E. Palmer, "Controlled formation of mass-selected Cu-Au core-shell cluster beams," *Journal of the American Chemical Society*, vol. 133, pp. 10325–10327, Jul 2011.

[24] R. L. Johnston, *Atomic and Molecular Clusters*. CRC Press, 2002.

[25] M. Schmidt, R. Kusche, W. Kronmüller, B. Von Issendorff, and H. Haberland, "Experimental determination of the melting point and heat capacity for a free cluster of 139 sodium atoms," *Physical Review Letters*, vol. 79, pp. 99–102, Jul 1997.

[26] S. L. Lai, J. Y. Guo, V. Petrova, G. Ramanath, and L. H. Allen, "Size-dependent melting properties of small tin particles: Nanocalorimetric measurements," *Phys. Rev. Lett.*, vol. 77, pp. 99–102, Jul 1996.

[27] A. A. Shvartsburg and M. F. Jarrold, "Solid clusters above the bulk melting point," *Physical Review Letters*, vol. 85, pp. 2530–2532, Sept 2000.

[28] K. Joshi, D. G. Kanhere, and S. A. Blundell, "Abnormally high melting temperature of the Sn_{10} cluster," *Physical Review B*, vol. 66, p. 155329, Oct 2002.

[29] G. A. Breaux, R. C. Benirschke, T. Sugai, B. S. Kinnear, and M. F. Jarrold, "Hot and solid gallium clusters: Too small to melt," *Phys. Rev. Lett.*, vol. 91, p. 215508, Nov 2003.

[30] M. Schmidt, R. Kusche, B. Von Issendorff, and H. Haberland, "Irregular variations in the melting point of size-selected atomic clusters," *Nature*, vol. 393, pp. 238–240, May 1998.

[31] H. Haberland, T. Hippler, J. Donges, O. Kostko, M. Schmidt, and B. von Issendorff, "Melting of sodium clusters: Where do the magic numbers come from?," *Phys. Rev. Lett.*, vol. 94, p. 035701, Jan 2005.

[32] F. Calvo and F. Spiegelmann, "Mechanisms of phase transitions in sodium clusters: From molecular to bulk behavior," *Journal of Chemical Physics*, vol. 112, pp. 2888–2908, Feb 2000.

[33] W. Wu, T. Pavloudis, A. V. Verkhovtsev, A. V. Solov'yov, and R. E. Palmer, "Molecular dynamics simulation of nanofilament breakage in neuromorphic nanoparticle networks," *Nanotechnology*, vol. 33, p. 275602, Jul 2022.

[34] J. Kern, J. Biesiadka, B. Loll, W. Saenger, and A. Zouni, "Structure of the Mn4-Ca cluster as derived from X-ray diffraction," *Photosynthesis Research*, vol. 92, pp. 389–405, Aug 2007.

[35] D. Bahena, N. Bhattarai, U. Santiago, A. Tlahuice, A. Ponce, S. B. Bach, B. Yoon, R. L. Whetten, U. Landman, and M. Jose-Yacaman, "STEM electron diffraction and high-resolution images used in the determination of the crystal structure of the Au144(SR)60 cluster," *Journal of Physical Chemistry Letters*, vol. 4, pp. 975–981, Mar 2013.

[36] B. Zhao, L. Li, F. Lu, Q. Zhai, B. Yang, C. Schick, and Y. Gao, "Phase transitions and nucleation mechanisms in metals studied by nanocalorimetry: A review," *Thermochimica Acta*, vol. 603, pp. 2–23, Mar 2015.

[37] F. Baletto and R. Ferrando, "Structural properties of nanoclusters: Energetic, thermodynamic, and kinetic effects," *Rev. Mod. Phys.*, vol. 77, pp. 371–423, May 2005.

[38] Z. Y. Li, N. P. Young, M. Di Vece, S. Palomba, R. E. Palmer, A. L. Bleloch, B. C. Curley, R. L. Johnston, J. Jiang, and J. Yuan, "Three-dimensional atomic-scale structure of size-selected gold nanoclusters," *Nature*, vol. 451, no. 7174, pp. 46–48, 2008.

[39] D. Nelli, G. Rossi, Z. Wang, R. E. Palmer, and R. Ferrando, "Structure and orientation effects in the coalescence of Au clusters," *Nanoscale*, vol. 12, no. 14, pp. 7688–7699, 2020.

[40] S. J. Pennycook, "Z-contrast STEM for materials science," *Ultramicroscopy*, vol. 30, pp. 58–69, Jun 1989.

[41] T. W. Liao, A. Yadav, K. J. Hu, J. Van Der Tol, S. Cosentino, F. D'Acapito, R. E. Palmer, C. Lenardi, R. Ferrando, D. Grandjean, and P. Lievens, "Unravelling the nucleation mechanism of bimetallic nanoparticles with composition-tunable core-shell arrangement," *Nanoscale*, vol. 10, no. 14, pp. 6684–6694, 2018.

[42] H. Nakamichi, K. Yamada, and K. Sato, "Sub-nanometre elemental analysis of Cu cluster in Fe-Cu-Ni alloy using aberration corrected STEM-EDS," *Journal of Microscopy*, vol. 242, pp. 55–61, Apr 2011.

[43] M. Schnedlitz, R. Fernandez-Perea, D. Knez, M. Lasserus, A. Schiffmann, F. Hofer, A. W. Hauser, M. P. De Lara-Castells, and W. E. Ernst, "Effects of the core location on the structural stability of Ni-Au core-shell nanoparticles," *Journal of Physical Chemistry C*, vol. 123, pp. 20037–20043, Aug 2019.

[44] A. R. Harutyunyan, G. Chen, T. M. Paronyan, E. M. Pigos, O. A. Kuznetsov, K. Hewaparakrama, S. M. Kim, D. Zakharov, E. A. Stach, and G. U. Sumanasekera,

"Preferential growth of single-walled carbon nanotubes with metallic conductivity," *Science*, vol. 326, pp. 116–120, Oct 2009.

[45] D. M. Foster, T. Pavloudis, J. Kioseoglou, and R. E. Palmer, "Atomic-resolution imaging of surface and core melting in individual size-selected Au nanoclusters on carbon," *Nature Communications*, vol. 10, no. 1, pp. 1–8, 2019.

[46] Z. Yang, X. Yang, and Z. Xu, "Molecular dynamics simulation of the melting behavior of Pt-Au nanoparticles with core-shell structure," *Journal of Physical Chemistry C*, vol. 112, no. 13, pp. 4937–4947, 2008.

[47] R. Huang, Y. H. Wen, G. F. Shao, and S. G. Sun, "Insight into the melting behavior of Au-Pt core-shell nanoparticles from atomistic simulations," *Journal of Physical Chemistry C*, vol. 117, no. 8, pp. 4278–4286, 2013.

[48] R. Huang, Y. H. Wen, Z. Z. Zhu, and S. G. Sun, "Two-stage melting in core-shell nanoparticles: An atomic-scale perspective," *Journal of Physical Chemistry C*, vol. 116, pp. 11837–11841, May 2012.

[49] M. J. López, P. A. Marcos, and J. A. Alonso, "Structural and dynamical properties of Cu-Au bimetallic clusters," *Journal of Chemical Physics*, vol. 104, no. 3, pp. 1056–1066, 1996.

[50] P. Grammatikopoulos, J. Kioseoglou, A. Galea, J. Vernieres, M. Benelmekki, R. E. Diaz, and M. Sowwan, "Kinetic trapping through coalescence and the formation of patterned Ag-Cu nanoparticles," *Nanoscale*, vol. 8, no. 18, pp. 9780–9790, 2016.

[51] B. N. Wanjala, J. Luo, B. Fang, D. Mott, and C. J. Zhong, "Gold-platinum nanoparticles: Alloying and phase segregation," *Journal of Materials Chemistry*, vol. 21, no. 12, pp. 4012–4020, 2011.

[52] J. A. Reyes-Nava, J. L. Rodríguez-López, and U. Pal, "Generalizing segregation and chemical ordering in bimetallic nanoclusters through atomistic view points," *Physical Review B*, vol. 80, p. 161412, Oct 2009.

[53] L. Deng, W. Hu, H. Deng, and S. Xiao, "Surface segregation and structural features of bimetallic Au-Pt nanoparticles," *Journal of Physical Chemistry C*, vol. 114, pp. 11026–11032, Jul 2010.

[54] A. P. Thompson, H. M. Aktulga, R. Berger, D. S. Bolintineanu, W. M. Brown, P. S. Crozier, P. J. in 't Veld, A. Kohlmeyer, S. G. Moore, T. D. Nguyen, R. Shan, M. J. Stevens, J. Tranchida, C. Trott, and S. J. Plimpton, "LAMMPS - A flexible simulation tool for particle-based materials modeling at the atomic, meso, and continuum scales," *Computer Physics Communications*, vol. 271, p. 108171, 2022.

[55] A. Stukowski, "Visualization and analysis of atomistic simulation data with OVITO-the Open Visualization Tool," *Modelling and Simulation in Materials Science and Engineering*, vol. 18, no. 1, p. 015012, 2010.

[56] A. Landa, P. Wynblatt, D. J. Siegel, J. B. Adams, O. N. Mryasov, and X. Y. Liu, "Development of glue-type potentials for the Al-Pb system: Phase diagram calculation," *Acta Materialia*, vol. 48, pp. 1753–1761, May 2000.

[57] S. Jang, Y. Purohit, D. L. Irving, C. Padgett, D. Brenner, and R. O. Scattergood, "Influence of Pb segregation on the deformation of nanocrystalline Al: Insights from molecular simulations," *Acta Materialia*, vol. 56, pp. 4750–4761, Oct 2008.

[58] Y. Purohit, S. Jang, D. L. Irving, C. W. Padgett, R. O. Scattergood, and D. W. Brenner, "Atomistic modeling of the segregation of lead impurities to a grain boundary in an aluminum bicrystalline solid," *Materials Science and Engineering A*, vol. 493, pp. 97–100, Oct 2008.

[59] X. Zhang, J. Liu, J. Tang, L. Li, M. Chen, S. Liu, and B. Zhu, "Element segregation on the surfaces of pure aluminum foils," *Applied Surface Science*, vol. 256, pp. 7300–7304, Sept 2010.

[60] L. Delgado-Callico, K. Rossi, R. Pinto-Miles, P. Salzbrenner, and F. Baletto, "A universal signature in the melting of metallic nanoparticles," *Nanoscale*, vol. 13, no. 2, pp. 1172–1180, 2021.

[61] A. Stukowski, "Structure identification methods for atomistic simulations of crystalline materials," *Modelling and Simulation in Materials Science and Engineering*, vol. 20, no. 4, p. 045021, 2012.

[62] C. Hock, S. Straßburg, H. Haberland, B. V. Issendorff, A. Aguado, and M. Schmidt, "Melting-point depression by insoluble impurities: A finite size effect," *Physical Review Letters*, vol. 101, p. 023401, Jul 2008.

[63] Q. S. Mei, S. C. Wang, H. T. Cong, Z. H. Jin, and K. Lu, "Determination of pressure effect on the melting point elevation of Al nanoparticles encapsulated in Al2O3 without epitaxial interface," *Physical Review B*, vol. 70, p. 125421, Sept 2004.

Chapter 7   Conclusions and Outlooks

7.1   Conclusions

The formation and breakage of conductive connections is fundamental to the functioning of cluster-based neuromorphic systems. The main contributions of this Thesis are to offer some new insight into the mechanisms of the formation and breakage, as well as to explore the properties of new possible cluster materials, with the molecular dynamics simulation method.

The thermal breakage of a gold nanofilament located between two gold nanoparticles was simulated via molecular dynamics simulations to study one of the underpinning mechanisms of cluster-based neuromorphic devices. Simulations of Au nanowires of different lengths (20–80 Å), widths (4–8 Å) and shapes, connecting two Au_{1415} nanoparticles (NPs), were performed as temperature was applied to mimic Joule heating, modelling the behaviour of a single synapse in a neuromorphic nanocluster network. The evolution of the system was monitored via a detailed structure identification analysis. It was found that atoms of the nanofilament gradually aggregate towards the clusters upon heating, causing the middle of the wire to gradually thin and then break. Most of the system remains crystalline during this process, but the centre is molten. The terminal NPs serve to increase the melting point of the nanowire by fixing it and they act as recrystallisation regions. A strong dependence of the behaviour on the widths of the NWs and also on their lengths and structures was found. These results may serve as guidelines for design and fabrication of one component in the realisation of cluster-based neuromorphic computing systems.

This Thesis also presents the results of molecular dynamics simulations of the reverse bridge formation between two 2.8-nanometre-sized Au_{1415} clusters deposited on a carbon (graphene) substrate. The bridge formation process is driven by the diffusion of gold atoms along the substrate, even when the clusters themselves are very close. The characteristic times of bridge formation were evaluated at elevated temperatures ($T = 500$–800 K) for different cluster orientations and distances between the neighbouring clusters, and they

are used to estimate the bridge formation time at room temperature. The bridge width has a power-law dependence on the simulation time, and the mechanism is a combination of diffusion and viscous flow. To consider the subsequent breakage of such a junction, the Joule heat generated by the electric current for different bias voltage values was estimated with a model used to determine the conductance of nanoscopic systems. The simulations of this process reveal the existence of a threshold voltage to activate thermally-induced bridge-breaking, and they provide atomistic insights into the dynamics of this process. The crucial role of the substrate in the bridge formation and breakage processes was revealed.

Taken together, the results of the simulations provide an atomistic-level understanding of some of the fundamental processes involving the conductive connections between individual clusters in cluster-based nanofilms, which is relevant to the practical realisation of cluster-based neuromorphic computing systems.

As we have seen, melting is a critical property that affects the fabrication and deployment of clusters in cluster-based neuromorphic devices. Core-shell clusters are candidate materials for cluster-based neuromorphic devices, e.g., to reduce materials costs. In this Thesis, molecular dynamics simulations have been employed to investigate the melting behaviour of prototypical Pb-Al core-shell clusters featuring a fixed Pb_{147} core and varying Al shell thickness. The results show that the core and shell melt independently. However, dramatically, the core atoms always break out of the shell and the nanoclusters prefer to settle into a segregated state when heated. Interestingly, the melting point of the core can be either depressed or elevated, depending on the thickness of the shell, due to competing mechanisms. As the shell becomes thinner the onset of the break-out event changes from the melting of the core to the melting of the shell, due to the lower melting temperature and robustness of the thinner shell. These results can serve as a reference for the future fabrication and experimental applications of these core-shell clusters.

The simulation studies in this Thesis thus provide insight into the mechanisms of switching in cluster-based (gold) neuromorphic systems due to heating, e.g. Joule heating, as well as to the fundamental thermal behaviour of prototypical candidate core-shell clusters.

7.2   Outlooks

There are many potential future studies that could be envisaged, based on the results and conclusions of this Thesis.

First, although we have identified several mechanisms that contribute to the formation and fission of connections between clusters in cluster arrays, the relative contributions of each mechanism and the relationship between these mechanisms are still unknown. Previous experiments have observed the combined effects of several mechanisms in the formation and breakage process of connections [1, 2], but it is challenging to integrate the different mechanisms while representing the atomistic structure of the system. For the formation process, the role of the van der Waals force and electric field induced surface diffusion/evaporation (EFISD/EFIE) have been studied previously [3–5], but a more comprehensive study on how these mechanisms work together to form a connection is still needed. For the fission process, electromigration is often considered the main mechanism [6–9], but this thesis and other studies [10, 11] have shown that the effect of Joule heating is also significant and can cause the fission of connections. The challenge for the future is to increase the scale of the simulations to incorporate all of the principal mechanisms of the dynamics of atoms in cluster arrays. In this context, the fundamentals of the electromigration process may need revisiting, since although there are many experimental observations of electromigration processes [12], simulation work on electromigration is typically limited to fixed current density or electric field [9]. There is a lack of research that considers the feedback effect on the current due to structural changes, to represent a realistic fission process under given bias.

So far as the supporting substrate of the clusters is concerned, this Thesis has only considered the effect of a model graphite substrate, but in actual devices, insulating substrates such as glass [13], silicon nitride [14, 15], or even paper [16] have to be used. Different substrates may have different effects on the mechanisms of both the formation and fission process, which are yet to be explored. The similarities and differences between the effects caused by different substrates are a crucial topic for future modelling. In addition to the various substrate options, there are also different types of clusters and nanoparticles that

could potentially be explored as building blocks for cluster-based neuromorphic devices. In this Thesis, we have only considered cuboctahedral gold clusters with various orientations, but there are many other materials, structures, sizes, and orientations to explore systematically.

This thesis has also studied the melting properties of core-shell clusters as a reference for future applications of these new material systems. However, a great deal more research is needed into how these materials would actually function in neuromorphic (or other) devices. Additionally, there are also many other forms of binary clusters, including nano-alloys with various structures and different electrical properties [17] that may affect the overall performance when used in devices, and possibly provide for tuning the device behaviour.

A range of possible future studies can then be summarized as follows:

- **The formation process**

  Carry out comprehensive atomistic studies of the formation process of connections between clusters, considering all known mechanisms (van der Waals force, EFIS-D/EFIE and surface diffusion along the substrate). Explore how these mechanisms contribute to the formation process and how the system behaviour relates to these mechanisms.

- **The fission process**

  Carry out atomistic studies of the fission process of connections at a given bias, including both the effects of electromigration and Joule heating. The current distribution should be recalculated in each frame, based on the structural changes occurring under constant bias.

- **The realistic substrate**

  Consider a model with a more realistic substrate such as silicon dioxide. Compare the behaviour of cluster arrays with and without the substrate to establish the effect of the substrate. Use the graphite substrates as a reference. Consider the effects of uneven and complex surface structure, including the appearance of point defects.

Silicon dioxide substrates with different surface structures can be compared to see if pinning sites of substrate affect the formation and fission mechanisms.

- **The structure of clusters**

  Explore different cluster isomers, such as decahedral and icosahedral clusters, with different orientations. Establish how the atomic structure affects the formation and fission processes in a systematic fashion.

- **Core-shell clusters in devices**

  Repeat neuromorphic simulations with core-shell clusters to investigate the possible use of alloy clusters in neuromorphic devices. Include alloy clusters with different compositions, atomic structures and orientations. Thus systematically explore the potential application of alloy clusters in neuromorphic devices.

References

[1] M. D. Pike, S. K. Bose, J. B. Mallinson, S. K. Acharya, S. Shirai, E. Galli, S. J. Weddell, P. J. Bones, M. D. Arnold, and S. A. Brown, "Atomic scale dynamics drive brain-like avalanches in percolating nanostructured networks," *Nano Letters*, vol. 20, no. 5, pp. 3935–3942, 2020.

[2] A. Sattar, S. Fostner, and S. A. Brown, "Quantized conductance and switching in percolating nanoparticle films," *Physical Review Letters*, vol. 111, no. 13, p. 136808, 2013.

[3] M. Olsen, M. Hummelgård, and H. Olin, "Surface modifications by field induced diffusion," *PLoS ONE*, vol. 7, no. 1, p. 30106, 2012.

[4] T. T. Tsong, "Effects of an electric field in atomic manipulations," *Physical Review B*, vol. 44, pp. 13703–13710, Dec 1991.

[5] T. M. Mayer, J. E. Houston, G. E. Franklin, A. A. Erchak, and T. A. Michalske, "Electric field induced surface modification of Au," *Journal of Applied Physics*, vol. 85, pp. 8170–8177, Jun 1999.

[6] T. H. Kim, X. G. Zhang, D. M. Nicholson, B. M. Evans, N. S. Kulkarni, B. Radhakrishnan, E. A. Kenik, and A. P. Li, "Large discrete resistance jump at grain boundary in copper nanowire," *Nano Letters*, vol. 10, no. 8, pp. 3096–3100, 2010.

[7] S. L. Johnson, A. Sundararajan, D. P. Hunley, and D. R. Strachan, "Memristive switching of single-component metallic nanowires," *Nanotechnology*, vol. 21, no. 12, p. 125204, 2010.

[8] T. B. Song, Y. Chen, C. H. Chung, Y. Yang, B. Bob, H. S. Duan, G. Li, K. N. Tu, and Y. Huang, "Nanoscale Joule heating and electromigration enhanced ripening of silver nanowire contacts," *ACS Nano*, vol. 8, no. 3, pp. 2804–2811, 2014.

[9] R. Hoffmann-Vogel, "Electromigration and the structure of metallic nanocontacts," *Applied Physics Reviews*, vol. 4, no. 3, p. 031302, 2017.

[10] S. Koo, J. Park, S. Koo, and K. Kim, "Local heat dissipation of Ag nanowire networks examined with scanning thermal microscopy," *Journal of Physical Chemistry C*, vol. 125, no. 11, pp. 6306–6312, 2021.

[11] C. L. Kim, J. Y. Lee, D. G. Shin, J. S. Yeo, and D. E. Kim, "Mechanism of heat-induced fusion of silver nanowires," *Scientific Reports*, vol. 10, p. 9271, 2020.

[12] W. Jeong, K. Kim, Y. Kim, W. Lee, and P. Reddy, "Characterization of nanoscale temperature fields during electromigration of nanowires," *Scientific Reports*, vol. 4, p. 4975, dec 2014.

[13] C. Minnai, A. Bellacicca, S. A. Brown, and P. Milani, "Facile fabrication of complex networks of memristive devices," *Scientific Reports*, vol. 7, no. 1, p. 7955, 2017.

[14] S. K. Bose, J. B. Mallinson, R. M. Gazoni, and S. A. Brown, "Stable self-assembled atomic-switch networks for neuromorphic applications," *IEEE Transactions on Electron Devices*, vol. 64, no. 12, pp. 5194–5201, 2017.

[15] J. B. Mallinson, S. Shirai, S. K. Acharya, S. K. Bose, E. Galli, and S. A. Brown, "Avalanches and criticality in self-organized nanoscale networks," *Science Advances*, vol. 5, no. 11, p. eaaw8483, 2019.

[16] C. Minnai, M. Mirigliano, S. A. Brown, and P. Milani, "The nanocoherer: An electrically and mechanically resettable resistive switching device based on gold clusters assembled on paper," *Nano Futures*, vol. 2, no. 1, p. 1002, 2018.

[17] R. Peköz, H. Oymak, and ş. Erkoç, "Binary Alloy Clusters: Structures and Electronic Properties," *Reviews in Theoretical Science*, vol. 2, pp. 301–319, dec 2014.

Publications list

[1] W. Wu, T. Pavloudis, A. V. Verkhovtsev, A. V. Solov'yov, and R. E. Palmer, "Molecular dynamics simulation of nanofilament breakage in neuromorphic nanoparticle networks," *Nanotechnology*, vol. 33, p. 275602, Jul 2022.

[2] W. Wu, A. V. Verkhovtsev, T. Pavloudis, A. V. Solov'yov and R. E. Palmer, "Neuromorphic nanocluster networks: Critical role of the substrate in nano-link formation," *Nano Research*, accepted, Apr 2023.

[3] W. Wu, T. Pavloudis and R. E. Palmer, "Core atoms escape from the shell: reverse segregation of Pb-Al core-shell nanoclusters via nanoscale melting," *submitted*.

Appendices

A. Scripts for the molecular dynamics simulations

A.1 MBN Explorer scripts

Energy minimization:

```
1  ; INPUT FILES
2  Input_File                = OPproject.in
3  Potential_File            = OPproject.pot
4
5  ; METHOD PARAMETERS
6  Interactions_Mode         = basic_interactions
7
8  ; OPTIMIZATION PARAMETERS
9  Disp_Tolerance            = 1.e-6
10 Force_Tolerance           = 1.e-6
11 Max_Particle_Displacement = 1.e-5
12 Optimization_Method       = conjugate_gradient
13 Optimization_Steps        = 10000000
14 Torque_Tolerance          = 1.e-6
15 Velocity_Quenching_Time_Step = 1
16
17 ; OUTPUT FILES
18 Log_File                  = OPproject.log
19 Log_Parameter             = p_energy step total_energy
20 Output_File               = OPproject.out
21 Trajectory_File           = OPproject.xyz
22 Trajectory_Format         = xyz
23
24 ; SIMULATION BOX PARAMETERS
25 Box_Size_X                = 50
26 Box_Size_Y                = 120
27 Box_Size_Z                = 50
```

```
28
29  ; SIMULATION PARAMETERS
30  Log_Steps                   = 100
31  Openmp                      = on
32  Task_Type                   = opt;optimization
33  Trajectory_Steps            = 5000
34
35  ; SYSTEM OF UNITS
36  Distance_Unit               = angstroem
37  Energy_Unit                 = ev
38  Temperature_Unit            = k
39  Time_Unit                   = fsec
40
41  Random                      = randomize
```

Molecular dynamics simulaiton:

```
1  ; DYNAMICS PARAMETERS
2  Antirotator                 = on
3  Initial_Temperature         = 300
4  Thermostat                  = langevin
5  Thermostat_Damping_Time     = 1
6  Thermostat_Temperature      = 300
7  thermostat_temperature_increase_rate = 0.02
8
9  ; INPUT FILES
10 Input_File                  = MDproject.in
11 Potential_File              = MDproject.pot
12
13 ; METHOD PARAMETERS
14 Interactions_Mode           = basic_interactions
15
16 ; OUTPUT FILES
17 Log_File                    = MDproject.log
```

149

```
18  Log_Parameter                = k_energy p_energy step temperature time
         total_energy
19  Output_File                  = MDproject.out
20  Trajectory_File              = MDproject.xyz
21  Trajectory_Format            = xyz
22
23  ; SIMULATION BOX PARAMETERS
24  Box_Size_X                   = 80
25  Box_Size_Y                   = 200
26  Box_Size_Z                   = 80
27
28  ; SIMULATION PARAMETERS
29  Integrator                   = verlet
30  Log_Steps                    = 1000
31  Openmp                       = on
32  Simulation_Time              = 10000
33  Task_Type                    = md;molecular_dynamics
34  Time_Step                    = 0.001
35  Trajectory_Steps             = 100000
36
37  ; SYSTEM OF UNITS
38  Distance_Unit                = angstroem
39  Energy_Unit                  = ev
40  Temperature_Unit             = k
41  Time_Unit                    = psec
42
43  Random                       = randomize
```

A.2   LAMMPS scripts

Energy minimization:

```
1  # Initialization
2
3  units    metal
```

```
 4  dimension        3
 5  boundary   f f f
 6  atom_style   atomic
 7
 8
 9  # Atom Definition
10
11  read_data atom_definition.txt
12
13
14  # Settings
15
16  pair_style eam/alloy
17  pair_coeff * * alpb-setfl.eam.alloy Pb Al
18
19  dump myDump all custom 1000 relaxed_structure.txt id type x y z
20  dump_modify myDump sort id
21
22  thermo_style custom step temp pe ke etotal enthalpy epair emol press
23  thermo 10
24
25
26  # Run a simulation
27
28  minimize 0 0 1000 1000
29
30  print "All done!"
```

Molecular dynamics simulaiton:

```
 1  # Initialization
 2
 3  units    metal
 4  dimension        3
 5  boundary   f f f
```

```
 6  atom_style   atomic
 7
 8
 9  # Atom Definition
10
11  read_data atom_definition.txt
12
13
14  # Settings
15
16  pair_style eam/alloy
17  pair_coeff * * alpb-setfl.eam.alloy Pb Al
18
19
20  velocity        all create 1 555 mom yes rot yes dist gaussian
21  fix             2 all nvt temp 1 1401 $(100.0*dt) drag 0.0 tchain 1
22  timestep        0.002
23
24  fix             3 all recenter INIT INIT INIT
25
26  dump myDumpBIG all custom 50000 MD_structure.txt id type x y z
27  dump_modify myDumpBIG sort id
28
29  thermo_style custom step temp pe ke etotal enthalpy epair emol press
30  thermo 50000
31
32  # Run a simulation
33
34  run             50000000
35
36  print "All done!"
```